

ABSTRACT

MCCONNELL, WYATT PARKS. The role of surface chemistry in defining the energetics and kinetics of single electron tunneling through individual gold nanoparticles. (Under the direction of Dr. Daniel L. Feldheim.)

The properties of nanoscale materials are often dominated by their surface chemistry due to their increased surface-to-volume ratio. Metal nanoparticles with diameters smaller than $\sim 12\text{nm}$ show a technologically relevant non-linear current-voltage response known as single electron tunneling. Gold nanoparticles offer an excellent platform for understanding how the surface chemistry of the metal island in a single electron-tunneling device can affect the current response of the structure. This is because the surfaces of these particles can be custom tailored using thiol-based self-assembled monolayer protocols that have been extensively developed for planar gold substrates.

This dissertation describes STM measurements of single electron tunneling through individual gold nanoparticles of various sizes and surface chemistries in both air and solvent at room temperature and pressure. The voltage step-width of the resulting coulomb staircase was shown to be dependent on particle size. Solution experiments show that the energetics of single electron tunneling of particles with certain surface chemistries is dependent on the composition of the solution, while other surface chemistries can produce particles that give a stable single electron tunneling response in a wide variety of local chemical environments. Using acid and base terminated surface chemistries, particles were made that showed a defined response to a specific change in the local solution pH. The kinetics of single electron tunneling was also shown to be highly dependent on the chemical bond formed between the capping ligand and the metal particle.

**THE ROLE OF SURFACE CHEMISTRY IN DEFINING THE
ENERGETICS AND KINETICS OF SINGLE ELECTRON TUNNELING
THROUGH INDIVIDUAL GOLD NANOPARTICLES**

By
WYATT PARKS MCCONNELL

A dissertation submitted to the Graduate Faculty of
North Carolina State University
In partial fulfillment of the
Requirements for the Degree of
Doctor of Philosophy

CHEMISTRY

Raleigh

2003

Approved by:

Chair of Advisory Committee

Dedication

To my extended family: Mom and Dad; Eddie, Kristi and Peyton; Mur, Pa and Mimma; Matthew, Jen and Abby; Jamie and Margie and many other friends and family members that are too numerous to list. This dissertation is a testament to what I've learned from you. That with commitment, we can learn and do anything we put our hearts and minds to; that achievement is worthy and honorable for its own sake; that helping others to achieve their goals is often the highest form of achievement we can attain; that we pursue science because it enhances our interactions with people, both through improved technology and a better understanding of our collective history and functioning; and that everything—even something as objective and dissociative as the quantitative study of science—can and should be pursued with an artist's perspective and an eye for creative expression. I thank each and every one of you for the friendship that breathes meaning and life into all of my diverse endeavors.

Biography

Wyatt Parks McConnell was born in Dalton, GA on April 21, 1975. He lived there for a scant three years before moving to southern California. The stay was again for a few short years, but the experience of the laid-back southern California lifestyle continues to inform the McConnell-family approach to living today (not to mention the reason that Wyatt learned to speak without a southern accent). At age eight the family moved back to the southeast. Concord, North Carolina this time where Wyatt would live through high school. Virginia Polytechnic Institute and State University was the next stop for four years of hiking, mountain biking, music making and a bit of chemistry thrown in when time allowed. A summer internship in 1996 working with Ameripol Synpol Corporation in Port Neches, TX, showed Wyatt graduate school was something he should pursue. During his senior year he worked in the lab of Dr. Mark Anderson studying the structure of self-assembled monolayers with surface reflectance infrared spectroscopy and quartz crystal microbalance gravimetry. The Bachelor's of Science Degree in Chemistry was awarded in May of 1997. The enthusiasm of the young faculty in the chemistry department at North Carolina State University attracted Wyatt there for graduate studies where he joined the Feldheim research group in February of 1998. On top of the research described in this dissertation, Wyatt also pursued teaching interests while at NC State. His experiences as a Hewlett Fellow with the Faculty Center for Teaching and Learning during 2000/2001 and in teaching a general chemistry lecture course in the summer of 2002 cemented his desire to pursue teaching as a career.

Acknowledgements

I would first like to thank two people whose work is presented in this dissertation: Lisa B. Lowe collected the DPV data discussed in Chapter 5, and Dr. Louis C. Brousseau III collected the current-voltage curves of galvinol-capped particles discussed in Chapter 6. I also owe a great debt to Dr. Lee Harrell for email discussions that led to Chapter 2 and Appendix A.

I have been lucky to have a very balanced committee, each member of which contributed significantly to this project and to my future success. Dan Feldheim has been an ideal research advisor, finding a balance between providing direction and allowing me to explore my own ideas. Chris Gorman has made significant contributions to my understanding of the challenges, goals and realities associated with studying molecular scale electronic devices. Discussions with Ed Bowden have provided me with a much deeper understanding of electronic instrumentation, electrode processes and electron transfer events. Chuck Boss has helped develop my teaching and presenting style, given me unique teaching opportunities and provided considered council on what to do next and how to develop a challenging and interesting career that maximizes my interests and skills. The sum of these committee members has truly been greater than the parts in this instance, and I am grateful for each of their unique contributions to my development over the last five years.

The Feldheim group has been a great place to work and I must acknowledge all of the members, past and present. This group manages to combine intellectual rigor with social awareness to produces an enjoyable and engaging environment for scientific study.

TABLE OF CONTENTS

List of Figures	vii
List of Tables	ix
1. Background and Scope: Possible applications of metal nanoparticles in future nanoscale electronic devices	1
1.1. Electronic age past and present	2
1.2. The foundation of current electronic devices: the MOSFET	4
1.2.1. MOSFET Architecture	4
1.2.2. MOSFET Operation	6
1.3. Study of nanoscale materials for electronic device applications	9
1.3.1 Motivation	9
1.3.2 Materials for nanoscale electronic applications	10
1.4. Metal nanoparticles	13
1.4.1 Quantized charging energies	13
1.4.2 Single electron-tunneling devices	16
1.5. The effect of surface chemistry on electronic properties at the nanoscale	21
1.6. Scope	23
1.7. Chapter One References	25
2. An analytic solution for the steady-state current response of a double tunnel junction: A computational approach to the semi-classical theory of single electron tunneling	27
2.1. The semi-classical theory	28
2.1.1. Analytic solution for tunneling rates	30
2.1.1.1. Electrostatic energy of the system	32
2.1.1.2. Work done by the voltage source	33
2.1.2. Determining $\rho(n, V)$	35
2.1.2.1. Self-consistent iterative approach	37
2.1.2.2. Calculating <i>relative</i> $\rho(n, V)$ values	37
2.1.2.3. Determining n_o	38
2.1.3. Computational approach	38
2.2. Current-voltage response as a function of input parameters	40
2.2.1. Ideal systems	40
2.2.2. Current-voltage response as a function of R_2	46
2.2.3. Current-voltage response as a function of C_2	48
2.2.4. Effect of temperature on the current-voltage response	50
2.3. Conclusions	52
2.4. Chapter Two References	53

3. Operation of the Digital Instruments Nanoscope IIIa multimode scanning tunneling microscope	54
3.1. STM operation	55
3.2. Digital Instruments Nanoscope IIIa	58
3.3. Conclusions	63
3.4. Chapter Three References	64
4. Current-voltage measurements of individual 5 and 10nm diameter gold nanoparticles	65
4.1. Introduction	66
4.2. Experimental	67
4.3. Results	69
4.4. Conclusions	71
4.5. Chapter Four References	72
5. Single electron-tunneling measurements of gold nanoparticles in solution: the role of capping monolayer in determining the sensitivity of a particle's single electron-tunneling properties to changes in the local chemical environment	73
5.1. Introduction	74
5.2. Experimental	75
5.3. Results	77
5.4. Discussion	80
5.5. Conclusions	82
5.6. Chapter Five References	84
6. A tailored response in the single electron-tunneling properties of individual gold nanoparticles to changes in buffer solution pH	85
6.1. Introduction	86
6.2. Experimental	88
6.3. Results	89
6.4. Discussion	92
6.5. Conclusions	96
6.6. Chapter Six References	98
7. The role of the supporting monolayer in defining the single electron-tunneling current magnitude for particle/monolayer/substrate structures probed with an STM	99
7.1. Introduction	100
7.2. Experimental	103
7.3. Results	104
7.4. Discussion	105
7.5. Conclusions	114
7.6. Chapter Seven References	115
Appendix	116

LIST OF FIGURES

1.1.	MOSFET structure.....	5
1.2.	MOSFET operation.....	7
1.3.	Carbon nanotube conformations.....	11
1.4.	Band diagrams of metal nanoparticles with a coulomb gap	14
1.5.	Single electron charging energies of metal nanoparticles.....	16
1.6.	Single electron tunneling/coulomb staircase	18
1.7.	Gated single electron tunneling	20
2.1.	Equivalent circuit for single electron tunneling.....	29
2.2.	Work done by the voltage source.....	35
2.3.	Calculated current-voltage response with ideal parameters.....	41
2.4.	Tunneling rates with ideal input parameters at positive bias.....	42
2.5.	Tunneling rates with ideal input parameters at negative bias.....	43
2.6.	Calculated current-voltage response as a function of R_1	45
2.7.	Calculated current-voltage response as a function of R_2	47
2.8.	$\rho(n, V)$ as a function of R_2	48
2.9.	Calculated current-voltage response as a function of C_2	49
2.10.	Calculated current-voltage response as a function of temperature	50
2.11.	Calculated current-voltage response with realistic experimental parameters.....	51
3.1.	Tunneling between two electrodes.....	57
3.2.	CITS screen shot.....	59
3.3.	Voltage sweep parameters in CITS mode.....	60
4.1.	Experimental approach with an STM	66
4.2.	Substrate preparation	68
4.3.	Current-voltage response near a particle and over background surface	69
4.4.	Current-voltage response of 5 and 10nm gold particles	70
5.1.	Current-voltage response of citrate-capped particles in different solvents.....	78
5.2.	Current-voltage response of octanethiol-capped particles in different solvents.....	78
5.3.	Differential pulse voltammetry of triphenylphosphine-capped particles in various solvents	79
5.4.	Difference of monolayer packing for triphenylphosphine- and octanethiol-capped particles	81
6.1.	Chemically gated single electron tunneling hypothesis.....	86
6.2.	Charge state of amine, galvinol and alkyl capping ligands as a function of pH.....	87
6.3.	Current-voltage curves of amine-capped particles in solutions of different pH.....	90
6.4.	Current-voltage curves of galvinol-capped particles in solutions of different pH.....	91
6.5.	Current-voltage curves of octanethiol-capped particles in solutions of different pH.....	91
6.6.	Step-width as a function of pH for galvinol- and amine-capped particles	93
6.7.	Equivalent circuit of double-layer capacitance for a monolayer coated electrode ..	94
7.1.	Equivalent circuit for proposed experiment.....	103
7.2.	Representative current-voltage curves for hexanedithiol and mercaptoheptamine supported particles	104

7.3.	Histograms for current step-height as a function of setpoint current and supporting monolayer	106
7.4.	Limitations of CITS in controlling tip-particle spacing.....	108
7.5.	Effect of barrier height on tunneling rate between two electrodes	110
7.6.	Comparison of semi-classical model to experimental data.....	112

LIST OF TABLES

5.1. Capacitance as measured by DPV for triphenylphosphine- and octanethiol-capped particles in various solvent systems	81
5.2. Capacitance as measured by STM for individual citrate- and octanethiol-capped particles in toluene and chloroform	83
6.1. Capacitance as measured by STM for individual amine-, galvinol- and octanethiol-capped particles for solutions of various pH	93
7.1. Current step-height as a function of STM setpoint current and supporting monolayer	106

Chapter 1

Background and Scope: Possible applications of metal nanoparticles in future nanoscale electronic devices.

1.1 The electronic age past and present

Technological and economic growth during the second half of the twentieth century was dominated by the electronic revolution. From communication and information systems, to consumer electronic devices to fuel-efficient automobiles, electronic circuits permeate the technologies we rely upon in our day-to-day lives. The foundation of this revolution is the transistor¹. Based upon unique properties of semiconductor materials, the transistor offers opportunities in electronic circuit design that were previously unthinkable. While transistor-based electronic circuit designs will continue to be a fundamental aspect of technology and our society, the search is on for materials with new and novel properties that will lead to new circuit architectures that can, like the introduction of transistor-based circuits, fundamentally change the way we interact with electronic devices and the technologies created from them².

Prior to the invention of the transistor, electronic circuit designs were based on bulky and fragile vacuum tube technology. The transistor is compact and robust, allowing for the development of the integrated circuit chip (IC). These chips contain many transistors hard-wired together in one package in such a way as to perform a specific task. For engineers, the IC means that rather than designing and building circuits from individual transistors and related components, ICs that perform specific tasks can be assembled in a modular approach to circuit design that allows appliances to be produced very cheaply. This ease of modular design coupled with a rapid decrease in IC production cost and steady increase in IC processing power has resulted in nearly every appliance we use, from personal computers to coffee pots, to be based on an electronic circuit.

Current ICs are produced via photolithography³. This process involves coating a substrate with the materials that will make up the completed circuit and then removing material that is not needed. The power of photolithography lies in the fact that an incredibly complex circuit design containing millions of transistors can be produced with only a few steps. The majority of the research in the microchip industry over the last several decades has been aimed at optimizing the photolithography process in order to pack more and more active components into the same amount of space, providing ICs with much more processing power. While the transistor has seen a consistent decrease in its size over the last six decades, its basic design and operation has changed very little.

While scientists and engineers continue to push the boundaries of what is possible with transistor circuits created from photolithography of bulk semiconductor materials, the last decade has seen significant efforts aimed at developing new materials for electronic device applications and new methods for circuit fabrication. Completely new approaches are being envisioned where instead of starting with a large piece of material and removing bits and pieces until a desired circuit remains, one starts with nanometer scale materials and assembles them into macroscale circuit architectures⁴. This is known as a bottom-up approach to circuit fabrication, whereas photolithographic methods are termed top-down.

The main advantage of the bottom-up approach is that it is very cheap and easy to synthesize large numbers of nanoscale materials like molecules, carbon nanotubes, and metal and semiconductor particles with highly uniform properties. Many of these materials show interesting electronic properties that suggest they are viable candidates for electronic device applications. The two challenges in this approach are understanding the

electronic properties of these nanoscale materials and developing methods for assembling these materials into macroscale circuits. The work presented in this dissertation is aimed at characterizing a class of these new materials. Specifically, it presents experiments that show how surface chemistry can affect the electronic properties of metal nanoparticles.

1.2 The foundation of current electronic devices: the MOSFET

1.2.1 MOSFET Architecture

The metal-oxide silicon field-effect transistor, or MOSFET, is the most commonly used transistor in current IC applications. The operation of the MOSFET is described here in order to provide context for understanding what is required of nanoelectronic materials. The MOSFET only performs two functions in any circuit: it can act as either a switch or an amplifier⁵. As a switch, the MOSFET can control whether or not current is allowed to flow through a specific part of the circuit. The binary computing paradigm that all digital technology is founded on is a result of this on/off nature of the transistor. As will be seen momentarily, a small change in applied voltage to part of the MOSFET can result in a very large change in voltage at another part of the circuit. In this way the MOSFET acts as an amplifier, producing a very large voltage change from a small voltage input.

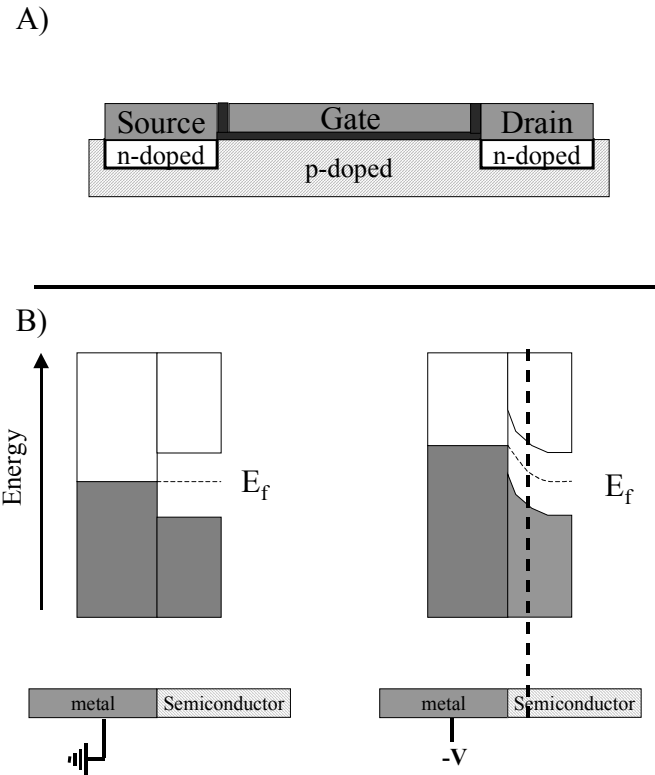


Figure 1.1 a) the cross-section of a typical MOSFET device where metallic source, gate and drain electrodes are placed on top of a semiconductor which forms the conduction channel. b) Band diagram for a metal/semiconductor interface with no bias, and negative bias applied to the metal electrode. The Fermi energy of the semiconductor is only altered in a thin region near the interface denoted by the vertical dashed line, called the depletion region.

The basic MOSFET (Figure 1.1a) consists of four main components: source, drain and gate electrodes coupled to a conduction channel. The conduction channel is made from doped silicon, a semiconductor. This conduction channel consists of alternating n/p/n or p/n/p doped regions lying under metallic source, gate and drain electrodes, respectively. An insulator is used to prevent charge leakage from the gate electrode into the conduction channel while the source and drain electrodes are attached directly to the

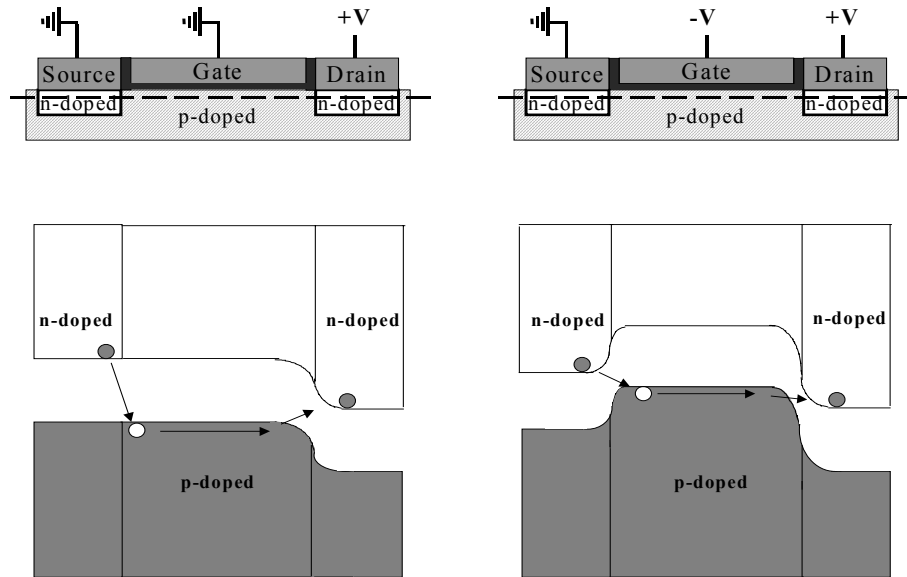
conduction channel to allow current to flow in and out of them. A constant voltage offset between the source and drain electrodes always exists, such that the drain electrode is at a lower electrostatic potential than the source electrode. The gate electrode is used to modulate the electrostatic environment of the middle segment of the conduction channel, transforming it between a conductive and non-conductive pathway to control the flow of current between the source and drain electrodes.

Before a detailed discussion of the operation of the MOSFET is presented, it is important to understand some basic electronic properties of bulk semiconducting materials⁶. Unlike metals, semiconductors can have heterogeneous charge distribution. This means that when a potential is applied to the source, drain or gate electrodes, the Fermi energy of the underlying semiconductor only aligns with the Fermi energy of the metal in a thin surface region of the semiconductor called the depletion layer (marked by the vertical dashed line in Figure 1.1b). This phenomenon is known as band bending. *All band diagrams of the conduction channel shown in the rest of this chapter refer just to the depletion region near the metallic electrode/semiconductor interface.* It is also important to note that n-doped semiconductors transport charge via electrons in their conduction band while hole mobility in the valence band allows for conduction in p-doped semiconductors.

1.2.2 MOSFET Operation

The left side of Figure 1.2a shows the band diagram of an n/p/n type conduction channel of a MOSFET where the drain electrode is biased positive with respect to the source electrode and the gate electrode is set at zero bias with respect to the source

a)



b)

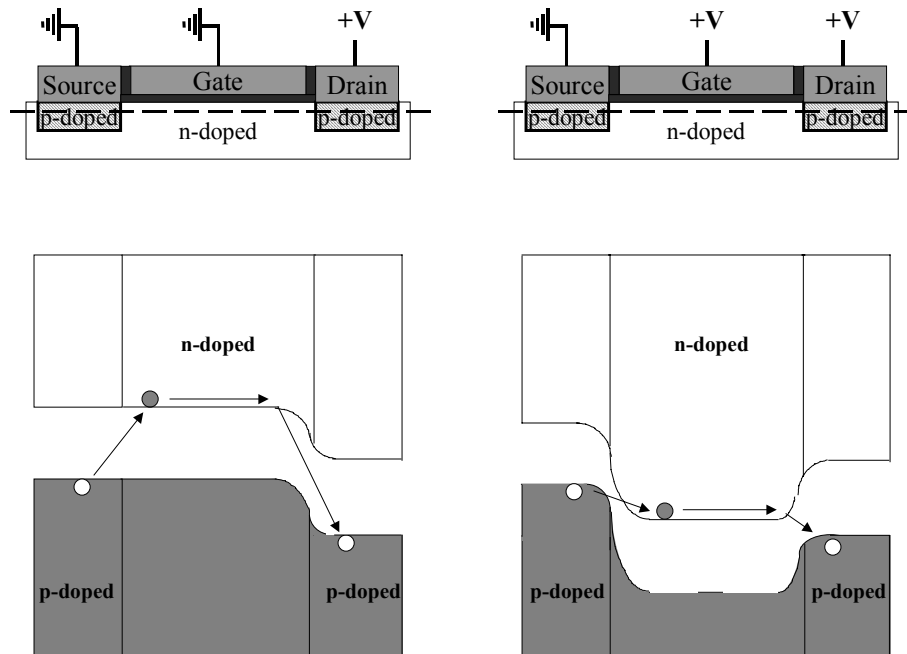


Figure 1.2 a) The band diagrams for an n/p/n doped conduction channel with zero and negative gate bias. Here conduction is only allowed when a negative bias is applied to the gate electrode. b) The band diagrams for a p/n/p doped conduction channel with zero and positive gate bias are shown. Here conduction is only allowed when a positive bias is applied to the gate electrode.

electrode. The Fermi energy of the source region is aligned with that of the gate region because the applied potentials are equal. Alignment of the Fermi energy of the gate section with that of the positively biased drain section leads to the band bending seen on the right side of the structure.

For conduction to occur in this system, an electron must be able to pass from the conduction band of the n-doped section under the source electrode into the valence band of the p-doped section under the gate electrode and finally into the conduction band of the n-doped silicon lying under the drain electrode. For this pathway to be energetically allowable, the valence band of the p-doped section must be raised in energy to an electrostatic potential between that of the valence bands of the two p-type segments. If the gate electrode is biased negative with respect to the source electrode, the electric field produced will raise the electrostatic potential at the surface of the p-doped section underneath the gate electrode (Figure 1.2b). This is where the term “field effect transistor” comes from; a change in the electric field experienced by the middle section of the conduction channel (in this case caused by a voltage applied to the gate electrode) controls the flow of current between the source and drain electrodes.

When the conduction channel is composed of alternating p/n/p-doped regions, the picture becomes slightly different (Figure 1.2b). Now the conduction band of the n-doped gated region must lie between the valence bands of the p-doped source and drain regions to allow current to flow. For this to occur a positive bias must be applied to the gate electrode in order to lower the potential of the depletion region in the p-doped section. Each of these two MOSFET structures requires a bias of specific sign to be applied to the gate electrode in order to align the bands in the depletion region of the

conduction channel in a way that allows current to flow from source to drain.

Importantly, transistors can be designed that turn “on” as a result of either a positive or negative applied gate bias, allowing for versatile logic structures.

The voltage required to switch a transistor from the “off” to the “on” state is usually ± 5 V. This is 50-100 times smaller than the voltage that can be supported between source and drain electrodes in the “off” state without device breakdown. The ability of a small voltage application to the gate electrode to result in a much larger change in voltage at the drain electrode by allowing current to flow through the conduction channel is what allows the transistor to act as an amplifier. The ratio of the voltage that the device can support between source and drain electrodes in the off state to the voltage required at the gate electrode to turn this voltage on is known as the device amplification factor.

1.3 Study of Nanoscale Materials for Electronics Applications

1.3.1 Motivation

The above discussion provides a context in which to study new materials for electronic device applications. At the minimum, new materials will need to accomplish these same tasks with greater efficiency and cost-savings. It may be possible to build devices from nanoscale materials that operate with different conduction mechanisms, such as resonant tunneling, that will allow for faster operation. Devices that operate accurately at much lower current levels may be discovered, allowing significant power savings for battery operated appliances. Simpler schemes for memory storage may be

possible, allowing for an exponential increase in the amount of available memory for computing systems.

More importantly, circuit operations that are currently inconceivable may come to life as more is learned about these materials and the devices that can be created from them. The transistor was not revolutionary because it allowed radios to be made portable and battery operated, but because engineers could now consider new applications for electronic circuits, like computing and random access memory, that were impossible practically with previous circuit architectures. In the same way, the early stages in the development of nanoscale electronic materials will see the replacement of current semiconductor devices in familiar appliances, but if anything that can truly be termed a nanotechnology revolution is to occur, entirely new and currently unpredictable applications for electronic circuits will have to come out of the unique opportunities afforded by these materials. Unique phenomena such as multiple stable conduction states and efficient non-linear optical properties may allow engineers to become truly creative with these materials to create devices and computing paradigms that have no corollary in today's technology.

1.3.2 Materials for nanoscale electronics

Individual molecules represent the ultimate in electronic component miniaturization. The benefits that are hyped by proponents of this molecular electronics revolution are the infinite tuneability of molecular properties, the ability to synthesize very large numbers of molecules with identical properties, and their incredibly small size⁸. Conjugated molecules have been shown to act reasonably well as electron

conductors, and molecules containing redox sites have been shown to be switchable from conductive to insulating depending on their oxidation state. Molecules appear to be limited to two-terminal device applications, and it is unclear as to whether or not molecules will be able to handle the current density required for stable device applications. It is also incredibly difficult to address a small number of molecules, which may negate any size advantage of molecule-based devices.

Conformational Differences in Single-Walled Carbon Nanotubes

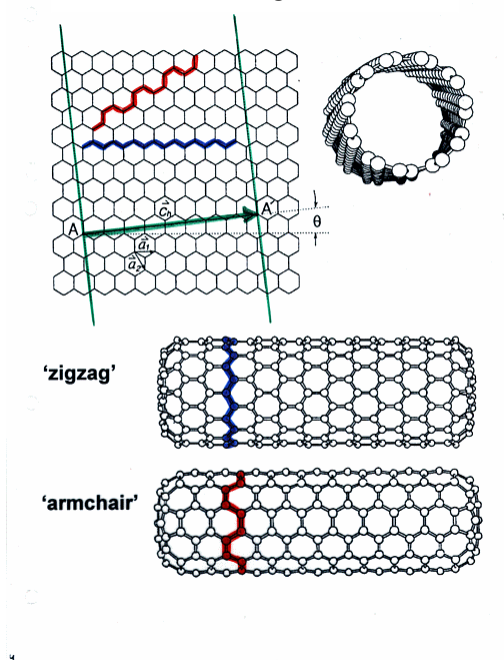


Figure 1.3 The conductivity of single –walled carbon nanotubes is highly dependent on the orientation of the carbon atoms with respect to the long axis of the tube. The armchair conformation leads to conductive tubes while the zigzag confirmation leads to tubes with semi-conducting properties.

Carbon nanotubes are part of the fullerene family of covalently bonded carbon molecules⁹. Carbon nanotubes consist of graphitic sheets of carbon atoms that have wrapped themselves into a tube (Figure 1.4). These tubes can be made from a single graphite sheet of carbon atoms or composed of multiple concentric sheets. Single-walled carbon nanotubes made from single sheets have shown the most promise for electronics

applications. The orientation of the carbon atoms with respect to the long axis of the tube determines whether it behaves like a conductor or a p-type semiconductor. Logic devices have been constructed by building crossed-networks of carbon nanotubes made from both conductor and p-type tubes¹⁰. Certain structures allow for the intersection to act as a gate, where one tube controls the flow of current through the other at the intersection. The micron lengths of carbon nanotubes allow for easy manipulation of tubes into these desired architectures. Other modes of current gating have been demonstrated as well, such as physical compression of the tube along its short axis¹¹. The ease with which carbon nanotube-based devices can be assembled, addressed and imaged makes them excellent candidates for next generation electronic device applications. They are also capable of supporting very high current densities.

The vivid color associated with solutions of metal and semiconductor nanoparticles is the first sign that their electronic and optical properties are quite different from their macroscopic counterparts¹². Shrinking the physical space that free electrons have to roam within the material results in a strong visible plasmon resonance, quantized charging energies, and eventually, if made small enough, to localized electronic states, much like those in a molecule. This dissertation studies how surface chemistry can affect the electronic properties of gold nanoparticles assembled in single electron tunneling devices. A detailed picture of the electronic structure of metal nanoparticles and a brief explanation of single electron tunneling¹³ follow in order to provide sufficient background to understand the motivation and hypothesis of this work.

1.4 Metal Nanoparticles

1.4.1 Quantized Charging Energy

The self-capacitance of a metal sphere¹⁴ is described by:

$$C = 4\pi\epsilon\epsilon_0 r \quad \text{equation 1.1}$$

Where ϵ_0 is the vacuum permittivity, ϵ is the permittivity of the medium surrounding the sphere and r is the radius of the sphere. This capacitance describes the energy required to add an individual electron to the sphere:

$$E_c = \frac{e^2}{C} \quad \text{equation 1.2}$$

For macroscopic metals, this capacitance is very large and it requires little energy to add charge to the particle. As the size of the sphere is decreased, the coulombic interactions of the electrons on the sphere increase as there is less space separating them. This increased coulombic interaction causes an increase in the charging energy (decrease in capacitance). As the size of the sphere drops below 10nm in diameter, this charging energy becomes greater than the thermal energy available in the system (k_bT), and the charge states of the metal sphere become quantized. By quantized, it is meant that the difference in energy between a sphere containing N electrons and a sphere containing $N + 1$ electrons is observable and measurable. Thus, the charging of a nanoscale metallic sphere can be observed one electron at a time^{12, 15}.

Figure 1.4 show the changes that result in the band diagram of a metal particle where $E_c \gg k_bT$ from the addition and removal of an individual electron to and from the

particle. For the neutral particle containing N electrons, there is an energy gap, known as the coulomb gap, between the highest energy electron (N), and the $N + 1$ level. This is a result of the large coulombic repulsion associated with adding an extra electron to the particle.

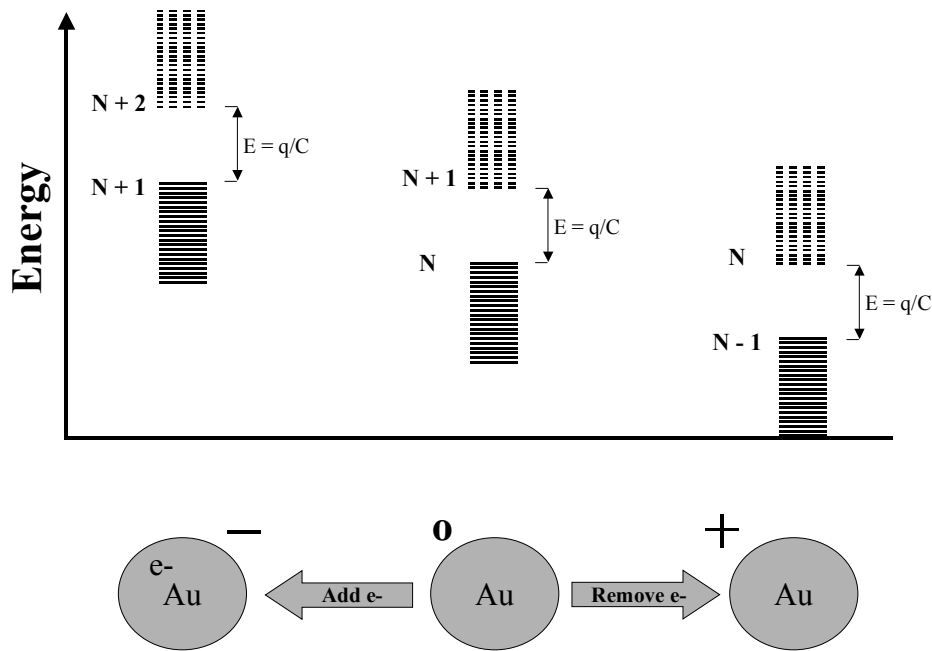


Figure 1.4 The middle structure shows the band diagram of a gold nanoparticle with its coulomb gap of q/C . When an electron is added to the particle (left), the electrostatic energy of the entire system is increased by q/C , resulting in a new coulomb gap of q/C separating the $N + 1$ electron and the lowest energy unfilled state. When an electron is removed from the particle the electrostatic energy of the system decreases by q/C , and the coulomb gap now exists between the $N - 1$ electron and the N state. This measurable change in the Fermi level of the nanoparticle with addition and removal of individual electrons is what gives them their unique electronic properties.

When this energy is overcome and the $N + 1$ electron is added to the particle, the added charge raises the electrostatic potential on the particle and thus raises the energy of all other electrons and unfilled states on the particle by $E = e/C$, thus creating a new coulomb gap between the $N + 1$ electron and the $N + 2$ level. When an electron is removed from

the neutral particle as shown on the right side of Figure 1.4, the opposite occurs. The electrostatic potential of the particle drops and so does the energy of all electrons and unfilled states on the particle.

It is important to note that this discussion has described the nanoparticles using band structures, not quantized molecular states. Metals $> 1\text{ nm}$ in diameter behave as free-electron materials and the quantized energy states are due to classical coulombic interactions, not quantum mechanical electronic states. Figure 1.5 shows the energy of the allowed charging states for a given particle. Again, these are quantized states, but they are classical in nature, resulting from the increased coulombic interactions that exist in a free electron system at the nanoscale, not from localized molecule-like electronic states. The coulombic nature of these quantized charging energies allows the electronic properties of metal particles with diameters greater than 1 nm to be fully described by classical terms.

The quantized coulomb charging of metal nanoparticles has been observed by both measuring the steady-state $I(V)$ response of individual particles¹⁶ and performing electrochemical experiments on bulk solutions of size monodisperse solutions of particles¹⁷. These experiments have shown that the Fermi energies of particles are extremely sensitive to local electric field¹⁸, and that many stable charging states can exist for a single particle. These two properties suggest that metal nanoparticles can form the foundation of new electronic circuits that operate with new gating techniques that use little power and in a multi-state mode providing an exponential increase in computing power over current binary systems¹⁹.

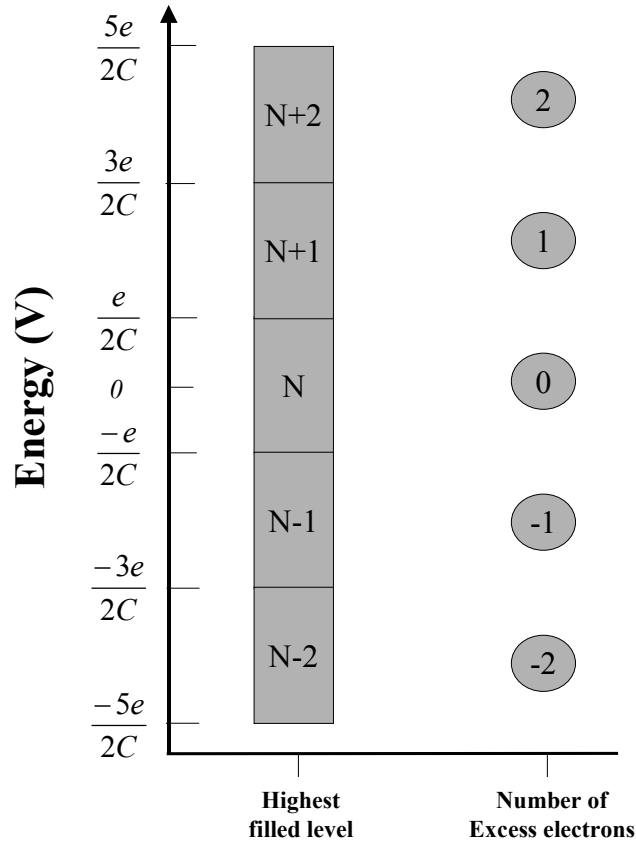


Figure 1.5 The energies at which transitions from $N \rightarrow N \pm 1$ excess electrons on a particle take place are shown. The left side shows the associated highest filled state from Figure 1.4 while the right side shows the number of excess electrons that exist on the particle at various positive and negative voltages. The characteristic coulomb gap of e/C is seen. These quantized states are unique in that they derive from coulombic repulsion forces between delocalized electrons, not from localized electronic states as in quantum dots and molecules.

1.4.2 Single Electron Tunneling Devices

Several methods for exploiting the quantized charging energies of metal nanoparticles have been proposed. Single electron tunneling devices, where a nanoparticle is connected to a source and drain electrode through tunnel junctions and a steady-state current passed through the metal nanoparticle are the most extensively

studied structures. To understand how these structures work, the current response of a basic two-terminal device as a function of increasing source-drain bias should be examined²⁰. The $I(V)$ curve of a particle connected to two electrodes through tunnel junctions results in a coulomb staircase containing sharp, regularly spaced increases in current separated by current plateaus (Figure 1.6). This can be understood by looking at the charging energies of the particle with respect to the source/drain bias. At low bias, the coulomb gap associated with adding an extra electron to the particle has not been overcome by the small source-drain bias and therefore no current is allowed to flow through the particle. This is known as the coulomb-blockade region. When the applied bias becomes larger than this charging energy, current is allowed to flow between the source and drain electrodes by the addition and removal of electrons one at a time to and from the $N + 1$ charging state of the particle. At this point the current plateaus until the applied bias overcomes the charging energy associated with placing an electron in the $N + 2$ state. The current then increases sharply again as current flows by the addition and removal of one electron at a time to and from both the $N + 1$ and $N + 2$ states. This trend continues within the operating window of the structure to produce the characteristic coulomb-staircase $I(V)$ response. This description is oversimplified in that it does not consider the finite rate of electron tunneling or the changes in the Fermi levels of the source and drain electrodes that occur during a tunneling event, but the functioning of the device can be understood from this description. Single electron tunneling will be described more extensively in Chapter 2.

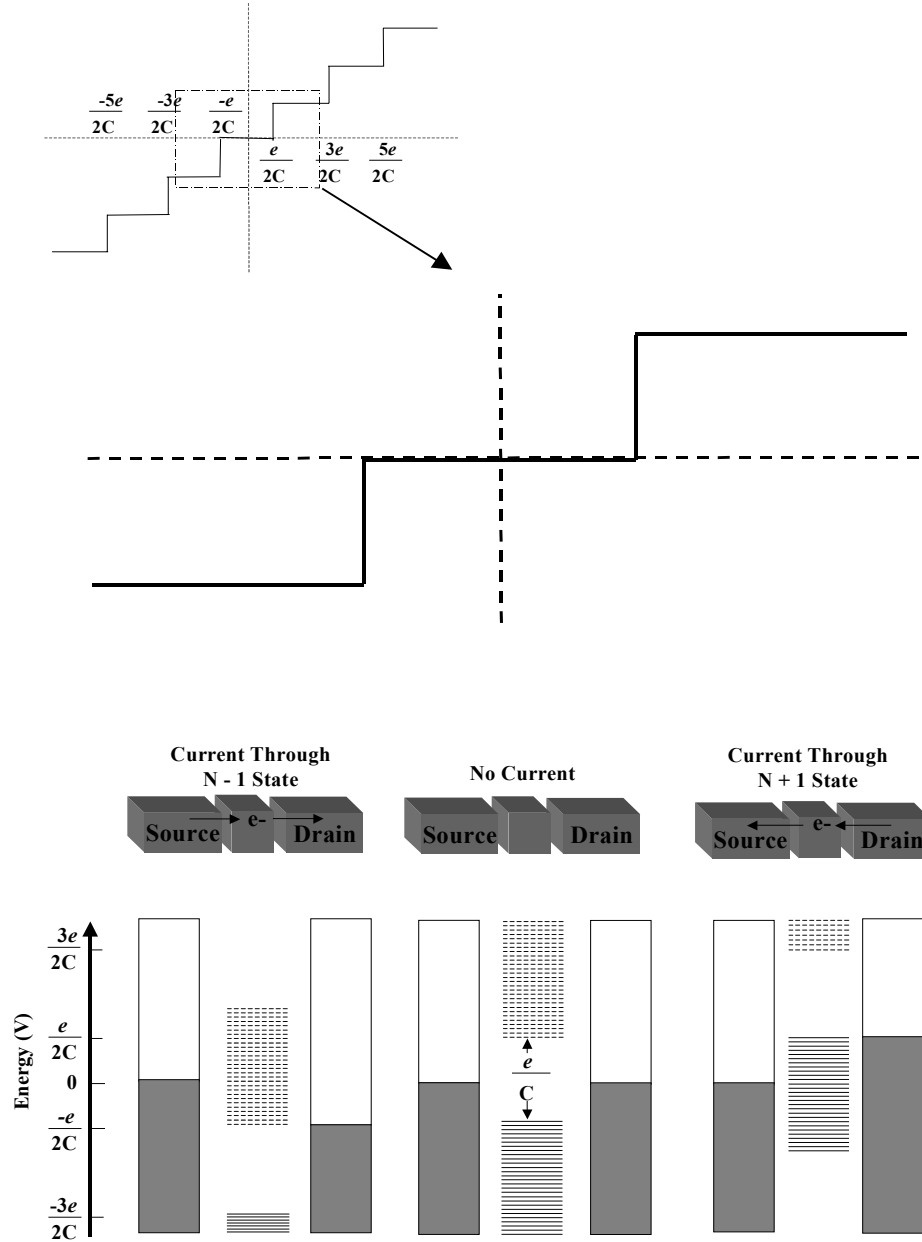


Figure 1.6 A coulomb staircase current-voltage curve resulting from single electron tunneling through a metal island connected to macroscopic electrodes through tunnel junctions is shown. The bottom of the picture shows the band diagram of the particle associated with the $I(V)$ features. At small biases no current flows because the source and drain electrodes are both still in the coulomb gap of the particle. Once the applied bias reaches $\pm e/2C$, current is allowed to flow through the $N+1/N-1$ state. Importantly, when current flows through this new state, the electrostatic energy of the particle shifts as shown in Figure 1.5, resulting in a new coulomb gap. This new coulomb gap means the current plateaus off until the applied bias increases by a further e/C and another step in current occurs. Thus, current steps are seen at voltages of $e(1+2n)/2C$ where n is an integer.

A third gate electrode can also be capacitively coupled to the particle (meaning no current is allowed to flow between the particle and this gate electrode) in order to modulate the current response of single electron tunneling structures and produce a single electron transistor¹⁸. As a potential is applied to the gate electrode with respect to the source electrode, the Fermi energy of the particle is changed (Figure 1.7). This changes the source-drain bias that is required to reach the first current step (V_{onset}), but does not change the spacing of the charging energies of the particle, therefore the voltage separation of current steps in the $I(V)$ curve remains the same. This change in V_{onset} results in a very similar $I(V)$ curve that has simply been shifted within the bias window. A negative gate bias will raise the Fermi energy of the particle and therefore shift the onset of current steps in the negative-bias direction, while a positive gate bias, as shown in Figure 1.7 will shift the coulomb staircase in the positive direction.

Two modes of operation for this single electron transistor can be imagined. The first is very similar to the MOSFET described earlier. The source-drain bias is held constant while the gate voltage is changed to modulate the current response between two different charging states. This holds several advantages over traditional MOSFET designs: an SET is much smaller, can operate at much lower current levels, and requires significantly smaller gate voltages, allowing more densely-packed circuit designs that require less power. An SET device also offers multiple stable current states, which could allow for multi-bit computing paradigms. The difficulties lie in building devices that provide stable operation in ambient conditions.

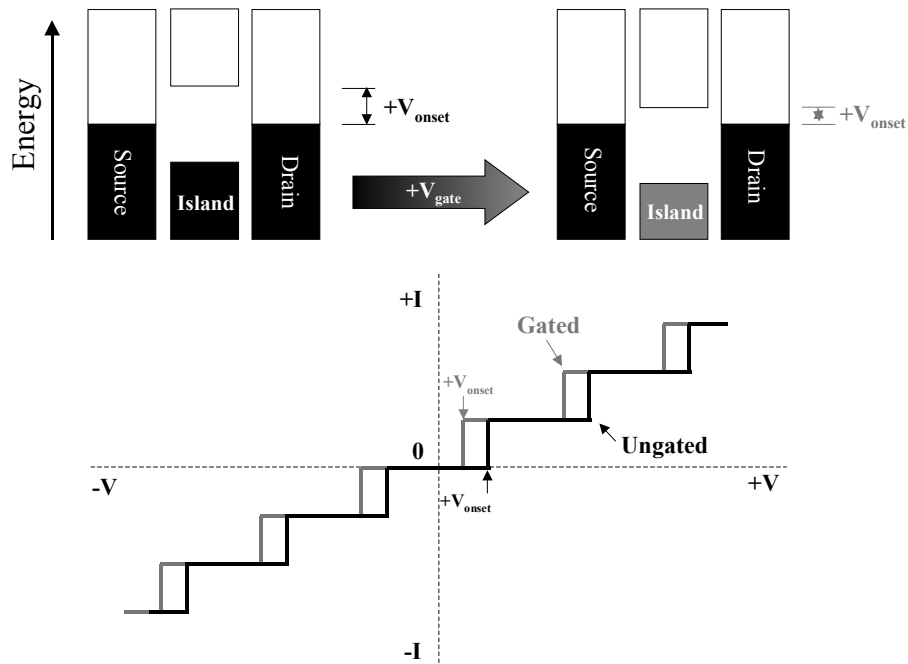


Figure 1.7 Two coulomb staircases are shown with a third gate electrode present. The band diagrams of the double tunnel junction system of each are shown at zero applied bias. The diagram shown on the right (gray curve) has a positive bias applied to the gate electrode. This bias lowers the energy of all the states on the particle, which allows for onset of the first step in the positive bias to occur at a lower voltage. The coulomb gap has not been altered, so the steps are still separated by e/C , but they are shifted within the bias window.

The second mode of operation is exemplified by work performed by Yoo and co-workers¹⁸ where a scanning single electron-tunneling device was constructed to act as a surface probe. When the device was scanned over a surface, differences in surface charge as small as $.01e$ could be detected by monitoring the gating effect the local surface region had on the $I(V)$ response of the SET device. Various sensing schemes can be imagined where monitoring the $I(V)$ response between the source and drain electrodes can allow observation of very small changes in gate electrode potential.

Single electron tunneling devices have been fabricated in several ways. Electron beam lithography has been used to pattern a metal island between two electrodes²¹. While this affords complete control over the dimensions and constitution of the structure,

it is very difficult and expensive to produce structures on this scale with lithography. Other approaches have involved assembling one^{16c} or a few metal nanoparticles^{16h} into the space between lithographically prepared source and drain electrodes. While this method is simpler and more reproducible than patterning the entire structure lithographically, construction of nanometer spaced electrodes is still not a routine process for most fabrication facilities. The easiest way for most laboratories to examine single electron tunneling is by using an STM to probe individual particles cast onto a conducting substrate^{16a, b, d, e, f, I, j}. In this system the substrate acts as one electrode, the STM tip the other and the nanoparticle is the metal island. This is the approach used in this dissertation to study the effect surface chemistry can have on the single electron tunneling properties of gold nanoparticles.

1.5 Surface chemistry's affect on electronic properties at the nanoscale

As the size of a material decreases, its surface-to-volume ratio increases. The extremely large surface-to-volume ratios that exist for nanoscale materials means that the surface chemistry can often play a dominant role in determining their overall properties. This has been shown to be true for the electronic properties of several nanoscale materials. Conductivity in carbon nanotubes is strongly dependent on oxygen adsorption to the nanotube surface²². Conductivities in atomic metal junctions have been seen to fluctuate largely and unpredictably in response to molecular adsorbates²³. Platinum nanowires have also been shown to change conductivity state in response to hydrogen sorption²⁴.

There is precedent for surface chemistry controlling electronic properties of macroscale materials as well. The ChemFET²⁵ is a design similar to the MOSFET described earlier where instead of using a metallic gate electrode to modulate the band structure of the conduction channel, the semiconductor surface is treated chemically such that some sort of molecular sorption event on the semiconductor surface coating causes a change in the local electric field of the depletion region and thus acts as a *chemical* gate. It seems plausible that if surface chemical changes on macroscale materials can result in a strong enough modulation of the local field to affect their current response, then single electron tunneling devices could be chemically gated in a similar manner via changes in the surface chemistry of the metal island.

Gold nanoparticles offer an ideal material for studies in this area. They can be readily synthesized in the size range required for single electron tunneling to be observed at room temperatures²⁶. Moreover, their surface chemistry is very similar to that of bulk gold allowing direct application of self-assembled monolayer (SAM) technology²⁷ to controlling the chemical structure of their surfaces²⁸. This provides an excellent platform to perform experiments aimed at determining if the surface chemistry of the metal island has a significant impact on the $I(V)$ response of single electron tunneling devices and if so, what the possible mechanisms for that impact are.

While these studies are stimulated by knowledge of current technologies such as the ChemFET and the MOSFET, the goal is not to simply produce a smaller version of these, but to gain further insight into the basic electronic properties of nanoscale materials. Motivations include an understanding of how devices produced from nanoscale materials can be structured in order to allow for stable operation in chemically

complex environments, exploring the possibility of low powered chemical gating mechanisms in nanoscale electronic devices, and attempting to detect individual molecular events in a small, compact package.

1.6 Scope

This dissertation describes STM measurements of individual gold nanoparticles that lead to the first observations of single electron tunneling in chemically complex environments, including solution phase measurements. These measurements show that single electron tunneling is strongly dependent on the surface chemistry of the metal island in the single electron-tunneling device. Chapters 5 and 6 demonstrate how certain particle-surface chemistries result in a nanoparticle whose coulomb charging energy is strongly affected by changes in the local chemical environment, while other surface chemistries result in very stable $I(V)$ response. Chapter 7 then shows that the chemical nature of the material separating the gold particle from the underlying substrate can have a strong impact on the current response of the structure. This suggests that these single electron-tunneling devices might be ideal systems for probing the electronic properties of individual molecules in a framework similar to those that might be used in molecular electronics applications.

Before these experimental results are presented, Chapter 2 provides a detailed theoretical analysis of single electron tunneling, including an analytic method for calculating steady-state current as a function of voltage using the semi-classical theory. Chapter 3 then describes the instrumentation used to measure the $I(V)$ response of

individual gold nanoparticles in this dissertation and Chapter 4 provides a proof-of-concept experiment where $I(V)$ measurements were made on particles of varying diameter to ensure that the $I(V)$ response can be attributed to single electron tunneling through individual gold nanoparticles.

1.7 Chapter One References

1. J. Bardeen and W.H. Brattain, *Phys. Rev.*, 1948, **74**, 230.
2. D. K. Ferry, ed. Quantum Transport in Ultrasmall Devices, Plenum Press, New York, 1995, 141.
3. a) D. F. Horne, "Photomasks, scales, and gratings", A. Hilger, Bristol, 1983. b) H. L. Stover ed., "Selected papers on optical microlithography", SPIE Optical Engineering Press, Bellingham, Washington, 1992.
4. a) N. B. Bowden, M. Weck, I. S. Choi and G. M. Whitesides, *Acc. Chem. Res.*, 2001, **34**, 231. b) J. L. Wilbur and G. M. Whitesides in "Nanotechnology" ed. G. Tripp, Springer-Verlag, New York, 1998, 331.
5. J. C. Ellenbogen, MITRE technical report number 98W0000024, The MITRE corporation, McLean, VA, January 1998.
6. A. R. West, "Basic Solid State Chemistry" 2nd edition, John Wiley and Sons, New York, 1996, 315.
7. C. B. Gorman, R. L. Carroll, R. R. Fuierer, *Langmuir*, 2001, **17**, 6923.
8. J. M. Tour, *Acc. Chem. Res.*, 2000, **33**, 791.
9. a) McCuen, P. L., *Nature*, 1998, **393**, 15. b)
10. Bachtold, A., P. Hadley, T. Nakanishi, C. Dekker, *Science*, 2001, **294**, 1317.
11. T. Rueckes, K. Kim, E. Joselevich, G.Y. Tseng, C.-L. Cheung, and C.M. Lieber, *Science* **289**, 94-97 (2000).
12. a) C. N. R. Rao, G. U. Kulkarni, P. J. Thomas, and P. P. Edwards, *Chem. Soc. Rev.*, 2000, **29**, 27-35. b) G. Schmid, M. Baumle, M. Geerkens, I. Heim, C. Osemann and T. Sawitowski, *Chem. Soc. Rev.*, 1999, **28**, 179-185. c) M. A. El-Sayed, *Acc. Chem. Res.*, 2001, **34**, 257.
13. M. Amman, K. Mullen and E. Ben-Jacob, *J. Appl. Phys.* 1989, **65**, 339.
14. <http://www.iue.tuwien.ac.at/publications/PhD%20Theses/wasshuber/node75.html>
15. L. P. Kouwenhoven and P. L. McEuen, in "Nanotechnology" ed. G. Timp, Springer-Verlag, New York, 1998, 471

16. a) P. J. Thomas, G. U. Kulkarni, C. N. R. Rao, *Chem. Phys. Lett.* 2000, **321**, 163.
b) L. E. Harrell, T. P. Bigioni, W. G. Cullen, R. L. Whetten and P. N. First, *J. Vac. Sci. Technol. B* 1999, 17, 2411. c) T. Sato, H. Ahmed, D. Brown and B. F. G. Johnson, *J. Appl. Phys.* 1997, 82, 696. d) S. T. Yau, P. Mulvaney, W. Xu and G. M. Spinks *Phys. Rev. B* 1998, 57, R15 124. e) E. Hartmann, P. Marquardt, J. Ditterich, P. Radojkovic and H. Steiberger, *App. Surf. Sci.*, 1996, 107, 197. f) R. P. Andres, T. Bein, M. Dorogi, S. Feng, J. I. Henderson, C. P. Kubiak, W. Mahoney, R. G. Osifchin and R. Refenberger, *Science*, 1996, 272, 1323. g) A. Bezryadin, C. Dekker and G. Schmid, *Appl. Phys. Lett.* 1997, 71, 1273. h) D. L. Klein, P. L. McEuen, J. E. Bowen-Katari, R. Roth and A. P. Alivisatos, *Appl. Phys. Lett.*, 1996, 68, 2574. i) J. G. A. Dubois, E. N. G. Verheijen, J. W. Gerritsen and H. van Kempen, *Phys. Rev. B*, 1993, 48, 11260. j) Barner, J. B. and Ruggiero, S. T., *Phys. Rev. Lett.*, 1987, 59, 807.
17. R. S. Ingram, M. J. Hostetler, R. W. Murray, T. G. Schaaff, J. T. Khoury, R. L. Whetten, T. P. Bigioni, D. K. Guthrie and P. N. First, *J. Am. Chem. Soc.*, 1997, 119, 9279.
18. M. J. Yoo, T. A. Fulton, H. F. Hess, R. L. Willett, L. N. Dunkleberger, R. J. Chichester, L. N. Pfeiffer and K. W. West, *Science*, 1997, 276, 579.
19. M. G. Ancona, *J. Appl. Phys.*, 1996, 79, 526.
20. M. Amman, K. Mullen, E. Ben-Jacob, *J. Appl. Phys.* 1989, **65**, 339.
21. E. H. Visscher, S. M. Verbrugh, J. Lindeman, P. Hadley and J. E. Mooij, *Appl. Phys. Lett.*, 1995, 66, 305.
22. P. G. Collins, K. Bradley, M. Ishigami, A. Zettl, *Science*, 2000, **287**, 1801.
23. A. Bogozi, O. Lam, J. Je, C. Li, N. J. Tao, L. A. Nagahara, I. Amlani, R. Tsui, *J. Am. Chem. Soc.*, 2001, **123**, 4585.
24. F. Favier, E. C. Walter, M. P. Zach, T. Benter, R. M. Penner, *Science*, 2001, 293, 2227
25. B., R. Eggins ed., "Chemical sensors and biosensors", John Wiley, New York, 2002.
26. a) G. Schmid ed. "Clusters and Colloids", VCH, New York, 1994. b) G. Schmid, *Chem. Rev.* 1992, 92, 1709. c) M. Brust, M. Walker, D. Bethell, J. J. Schiffrin, R. J. Whyman, *Chem. Comm.*, 1994, 801.
27. A. Ullman, *Chem. Rev.*, 1996, 96, 1533.
28. R. W. Murray, et al, *J. Am. Chem. Soc.*, 1996, 118, 4212.

Chapter 2

An analytic solution for the steady-state current response of a tunnel junction: A computational approach to the semi-classical theory of single electron tunneling.

A simplified view of a single electron tunneling structure was shown in Chapter 1. A full description of the current response of a double tunnel junction system as a function of applied voltage will now be presented. Section 2.1 presents the derivation of the semi-classical theory¹ used to calculate the steady state current of a double tunnel junction structure. Section 2.2 then presents several calculated $I(V)$ curves and describes their shape as a function of junction resistance and capacitance as well as temperature.

2.1 The semi-classical theory

Figure 2.1 shows the equivalent circuit for a double tunnel junction where R_i and C_i define the resistance and capacitance of the i th tunnel junction. The tunneling rates through the i th tunnel junction are defined as Γ_i^\pm where Γ_i^+ corresponds to tunneling onto the particle through the i th junction and Γ_i^- corresponds to tunneling off the particle through the i th junction. It will be shown that this rate is a function of applied voltage, V , and the excess number of electrons on the particle, n . The steady-state current flowing through the system at a particular voltage is defined by Kirkhoff's law to be the difference in the rate of tunneling onto the particle through the i th junction and the rate of tunneling off the particle through the i th junction:

$$\begin{aligned} I(V) &= -e(\Gamma_1^+(V) - \Gamma_1^-(V)) \\ I(V) &= -e(\Gamma_2^-(V) - \Gamma_2^+(V)) \end{aligned} \quad \text{equation 2.1}$$

This is complicated somewhat by the fact that the tunneling rates are a function not just of applied voltage, but also n , the excess number of electrons on the particle. At a

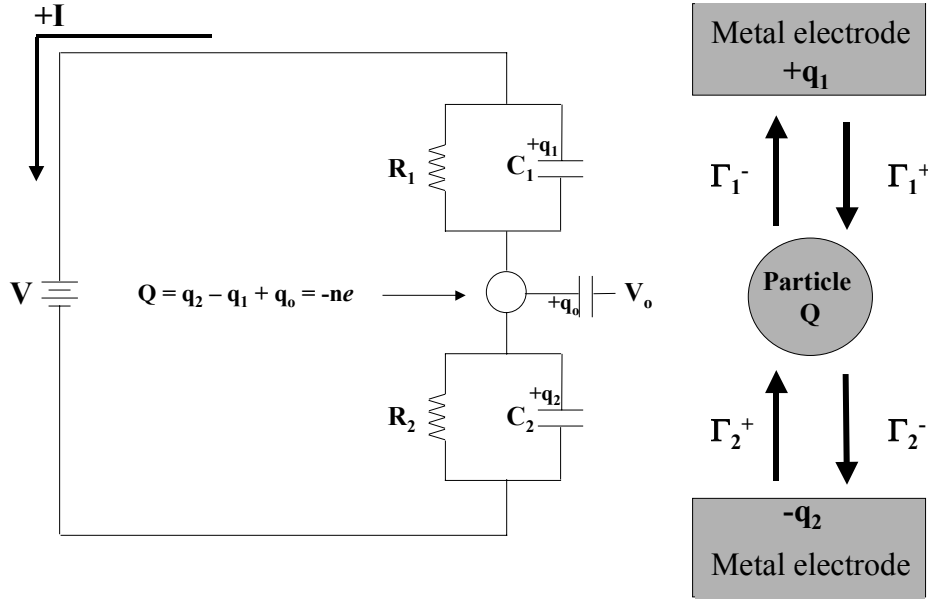


Figure 2.1 The equivalent circuit for a double-tunnel junction system is shown. The direction of positive current flow causes the charge associated with capacitor 1 to be positive in the electrode while that of capacitor 2 is negative in the electrode. The total charge on the particle is the sum of all capacitive charges from electrodes capacitively connected to it and is related to the integer number of excess electrons on the particle, n , through the charge of an electron, e . The rates of tunneling through each junction are shown on the right.

specific voltage, the particle has a very high probability of containing a specific number of excess electrons, $\rho(n_o, V)$. For real systems, there is also a measurable probability that the particle will exist with several different values of excess electrons. For these systems, the steady state current calculation must take into account contributions from all possible values of n :

$$\begin{aligned}
I(V) &= \sum_{n=-\infty}^{+\infty} -e\rho(n,V) \left(\Gamma_1^+(n,V) - \Gamma_1^-(n,V) \right) \\
I(V) &= \sum_{n=-\infty}^{+\infty} -e\rho(n,V) \left(\Gamma_2^-(n,V) - \Gamma_2^+(n,V) \right)
\end{aligned}
\tag{equation 2.2}$$

Where $\rho(n,V)$ is the probability of the particle containing n electrons when the applied voltage is V . While this is shown as a sum over all values of n , for a metal particle below 10nm in diameter at room temperature there are fewer than ten values of n that have a measurable probability of existing for a given voltage.

Examination of equation 2.2 shows that an analytic solution for the steady state current as a function of voltage for a given single electron tunneling structure will require a method for determining the rate of electron transfer through the tunnel junctions in both directions as a function of V and n , and a method for determining the probability that the system contains n excess electrons.

2.1.1 Analytic solution for tunneling rates

The tunnel rates can be determined by considering Fermi's golden rule²:

$$\begin{aligned}
\Gamma_i^+ &= \int_{-\infty}^{+\infty} \frac{2\pi}{\hbar} |T(E)|^2 D_i(E - E_i) f(E - E_i) D_p(E - E_p) [1 - f(E - E_p)] dE \\
\Gamma_i^- &= \int_{-\infty}^{+\infty} \frac{2\pi}{\hbar} |T(E)|^2 D_p(E - E_p) f(E - E_p) D_i(E - E_i) [1 - f(E - E_i)] dE
\end{aligned}
\tag{equation 2.3}$$

Where $T(E)$ is the tunneling matrix element, E_i is the Fermi energy of the electrode, E_p is the Fermi energy of the particle, $D_i(E - E_i)$ is the single electron density of states of the

electrode, $D_p(E - E_p)$ is the single electron density of states of the particle, $f(E - E_i)$ is the distribution of the electrode Fermi energy and $f(E - E_p)$ is the distribution of the particle Fermi energy. This integral is simplified significantly when the tunneling matrix and the density of states are taken to be independent of energy. Defining $\hbar/2\pi e^2 D_i D_p |T|^2$ as the resistance of the i th tunnel junction gives the tunnel rate as:

$$\begin{aligned}\Gamma_i^+ &= \frac{1}{e^2 R_i} \frac{-(E_p - E_i)}{1 - \exp((E_p - E_i)/k_b T)} \\ \Gamma_i^- &= \frac{1}{e^2 R_i} \frac{-(E_i - E_p)}{1 - \exp((E_i - E_p)/k_b T)}\end{aligned}\tag{equation 2.4}$$

where T is the temperature (K) and k_b is Boltzman's constant (J/K). This now defines the tunnel rates on and off the particle through each junction as a function of the associated junction resistance and the difference in the Fermi energies of the particle and associated electrode. For simplification the following definitions will be used in the rest of this derivation:

$$\begin{aligned}\Delta E_i^+ &= (E_p - E_i) \\ \Delta E_i^- &= (E_i - E_p)\end{aligned}\tag{equation 2.5}$$

The difference in Fermi energy of the particle and electrode can be determined without calculating the absolute values of each Fermi level by requiring energy to be conserved during an individual tunneling event. For this condition to hold, the difference in Fermi energy, ΔE_i^\pm must be equal to the sum of the change in potential energy of the

double tunnel junction (U) and the change in energy of the voltage source (W) that occur when an electron tunnels on or off the particle:

$$\Delta E_i^{\pm} = U(n \rightarrow n \pm 1) - W(n \rightarrow n \pm 1) \quad \text{equation 2.6}$$

2.1.1.1 Electrostatic energy of the system

The electrostatic energy of the tunnel junction, U , is defined by the capacitive elements of the equivalent circuit shown in Figure 2.1:

$$U = \frac{q_1^2}{2C_1} + \frac{q_2^2}{2C_2} + \frac{q_o^2}{2C_o} \quad \text{equation 2.7}$$

The induced charge from environmental capacitance, q_o , is considered to be constant and is not affected by changes in V , q_1 or q_2 . The total charge on the nanocrystal can then be written as:

$$Q = q_2 - q_1 + q_o = -ne \quad \text{equation 2.8}$$

where n is the integer number of excess electrons on the particle. The negative sign associated with q_1 is a result of the circuit convention shown in figure 2.1: q_1 is positive on the electrode side of C_1 and negative on the particle side, while q_2 is positive on the particle side of C_2 and negative on the electrode side. The charges q_1 and q_2 can be considered as separate because they exist separately on the electrodes connected to the

particle, but on the particle, one can not differentiate between q_1 and q_2 , and the total charge resulting from all capacitive interactions, Q , is all that is seen on the particle. The total voltage across the double tunnel junction can be written as

$$\begin{aligned} V &= V_1 + V_2 \\ V &= \frac{q_1}{C_1} + \frac{q_2}{C_2} \end{aligned} \quad \text{equation 2.9}$$

Solving for q_1 and q_2 gives:

$$\begin{aligned} q_1 &= V \frac{C_1 C_2}{(C_1 + C_2)} + \frac{neC_1}{(C_1 + C_2)} + \frac{q_o C_1}{(C_1 + C_2)} \\ q_2 &= V \frac{C_1 C_2}{(C_1 + C_2)} - \frac{neC_2}{(C_1 + C_2)} - \frac{q_o C_2}{(C_1 + C_2)} \end{aligned} \quad \text{equation 2.10}$$

Using equation 2.10 in equation 2.7 gives the change in electrostatic energy of the tunnel junction resulting from a transition from n excess electrons to $n \pm 1$ excess electrons on the particle:

$$\Delta U(n \rightarrow n \pm 1) = \frac{e}{(C_1 + C_2)} \left(\frac{e(1 \pm 2n)}{2} + q_o \right) \quad \text{equation 2.11}$$

2.1.1.2 Work done by the voltage source

The charge on the capacitor of each tunnel junction, q_1 and q_2 , can be considered separate because they exist on separate electrodes. But on the particle, all capacitive

charges sum to produce the total charge on the particle, Q . When the number of excess electrons on the particle changes due to a tunneling event, the voltage source must add or remove charge from the electrodes that are capacitively coupled to the particle in order to account for the change in equation 2.9 that results from changes in q_1 and q_2 . Figure 2.2 shows that when an electron tunnels off the particle through junction 2, q_1 must be changed by $eC_1/(C_1 + C_2)$ to account for this decrease in the total charge on the particle. The work done by the voltage source for a tunneling event on or off the particle through junction 2 is thus:

$$W_2 = \mp \frac{eC_1V}{(C_1 + C_2)} \quad \text{equation 2.12}$$

For an electron tunneling on/off the particle through junction 1, the required corresponding change in q_2 is $eC_2/(C_1 + C_2)$ and the work done by the voltage source is:

$$W_1 = \pm \frac{eC_2V}{(C_1 + C_2)} \quad \text{equation 2.13}$$

The sign related to the work done by the voltage source is a result of the convention chosen in figure 2.1 for positive current. Putting equations 2.12 and 2.13 into equation 2.6 now gives the difference in Fermi energy associated with a tunneling event:

$$\begin{aligned} \Delta E_1^\pm(n, V) &= \frac{e}{(C_1 + C_2)} \left(\frac{e(1 \pm 2n)}{2} \pm q_o \pm C_2V \right) \\ \Delta E_2^\pm(n, V) &= \frac{e}{(C_1 + C_2)} \left(\frac{e(1 \pm 2n)}{2} \pm q_o \mp C_1V \right) \end{aligned} \quad \text{equation 2.14}$$

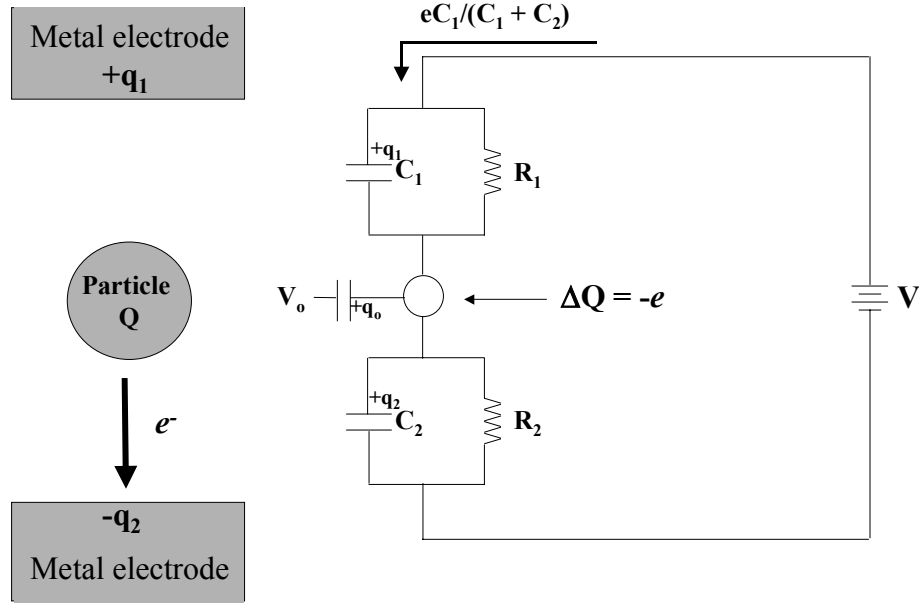


Figure 2.2 When an electron tunnels off the particle through junction 2, the total charge on the particle changes by $-e$. The charge on capacitor 1 must then be adjusted to account for this change by removing $eC_1/(C_1 + C_2)$ from electrode 1. This change in charge requires work from the voltage source.

Equation 2.14 can now be applied to equation 2.4 to give:

$$\Gamma_i^{\pm} = \frac{1}{2eR_i} \frac{-\Delta E_i^{\pm}}{1 - \exp(\Delta E_i^{\pm}/k_b T)} \quad \text{equation 2.15}$$

At absolute zero temperature, tunneling rates can have negative values. This occurs when the Fermi energy of the “drain” electrode is higher than the Fermi level of the associated “source” electrode. Without the aid of thermal energy, there is no way for an

electron to overcome this barrier to tunneling, therefore these negative tunneling rates should be assigned a value of zero.

With the tunneling rates in hand, it is now required to determine the probability of the particle containing n excess electrons in order to use equation 2.2 to determine the steady state current for a given voltage.

2.1.2 Determining $\rho(n, V)$

Normalization conditions require that:

$$\sum_{n=-\infty}^{+\infty} \rho(n, V) = 1 \quad \text{equation 2.16}$$

This requirement results in^{1b}:

$$\rho(n, V) = \frac{\prod_{i=-\infty}^{n-1} (\Gamma_1^+(i, V) + \Gamma_2^+(i, V)) \prod_{i=n+1}^{+\infty} (\Gamma_1^-(i, V) + \Gamma_2^-(i, V))}{\sum_{j=-\infty}^{+\infty} \left(\prod_{i=-\infty}^{j-1} (\Gamma_1^+(i, V) + \Gamma_2^+(i, V)) \prod_{i=j+1}^{+\infty} (\Gamma_1^-(i, V) + \Gamma_2^-(i, V)) \right)} \quad \text{equation 2.17}$$

Solving equation 2.17 is computationally difficult. Fortunately, a different route can be used for determining $\rho(n, V)$ for a finite number of n values.

2.1.2.1 Self-consistent iterative approach

Consider that under steady state current conditions, the rate of transition from the n to $n+1$ state must be the same as the rate of transition from the $n + 1$ state to the n state.

Thus:

$$\rho(n, V) (\Gamma_1^+(n, V) + \Gamma_2^+(n, V)) = \rho(n+1, V) (\Gamma_1^-(n+1, V) + \Gamma_2^-(n+1, V)) \quad \text{equation 2.18}$$

For metal nanoparticles smaller than 10nm in diameter within a five volt window, $\rho(n, V)$ will only be greater than zero for ~ 10 different values of n . Using equation 2.18, a self-consistent iterative approach can be used to determine the relative values of $\rho(n, V)$ for all relevant values of n and then normalization conditions applied to give the absolute values of all applicable $\rho(n, V)$:

$$\rho(n, V) = \frac{\text{relative} \rho(n, V)}{\sum_{i=n_{\min}}^{n_{\max}} \text{relative} \rho(i, V)} \quad \text{equation 2.19}$$

2.1.2.2 Calculating *relative* $\rho(n, V)$ values

The *relative* $\rho(n, V)$ values can be obtained by first determining the number of excess electrons that is most probable on the particle at the particular voltage, n_o . Section 2.1.2.3 describes this process. Once this state is determined, it is assigned a relative probability of 1:

$$\text{relative} \rho(n_o, V) = 1 \quad \text{equation 2.20}$$

After this assignment is made, all other *relative* $\rho(n, V)$ values can be calculated iteratively using equation 2.18:

$$\begin{aligned}
relative\rho(n+1,V) &= \frac{relative\rho(n,V)(\Gamma_1^+(n,V) + \Gamma_2^+(n,V))}{\Gamma_1^-(n+1,V) + \Gamma_2^-(n+1,V)} \\
relative\rho(n-1,V) &= \frac{relative\rho(n,V)(\Gamma_1^-(n,V) + \Gamma_2^-(n,V))}{\Gamma_1^+(n-1,V) + \Gamma_2^+(n-1,V)}
\end{aligned}$$

equation 2.21

2.1.2.3 Determining n_o

For an excess number of electrons, n_o , to be the most probable state of the particle, the following conditions must be valid:

$$\begin{aligned}
\rho(n_o, V) &> \rho(n_o + 1, V) \\
\rho(n_o, V) &> \rho(n_o - 1, V)
\end{aligned}$$

equation 2.22

Applying these conditions to equation 2.18 results in the following:

$$\begin{aligned}
(\Gamma_1^+(n_o - 1, V) + \Gamma_2^+(n_o - 1, V)) &\geq (\Gamma_1^-(n_o, V) + \Gamma_2^-(n_o, V)) \\
(\Gamma_1^-(n_o + 1, V) + \Gamma_2^-(n_o + 1, V)) &\geq (\Gamma_1^+(n_o, V) + \Gamma_2^+(n_o, V))
\end{aligned}$$

equation 2.23

These conditions can be used to determine the most probable number of excess electrons at a particular voltage and the value of $relative\rho(n_o, V)$ set equal to one.

2.1.4 Computational approach

It is important to present the derivation of the semi-classical model in its entirety. This complete presentation can be difficult to follow at times, so now a stepwise computational approach to calculating current as a function of voltage for given junction parameters is presented. For metal nanoparticles <8 nm in diameter examined over a

voltage range from -2 to $+2$ V, n values ranging from -4 to $+4$ are sufficient. For larger particles or a wider voltage window, more values of n may need to be considered.

1. Calculate the difference in Fermi energy of the particle and electrode for tunneling on and off the particle through each tunnel junction, ΔE_1^\pm and ΔE_2^\pm , as a function of voltage for all n values being considered using equation 2.14.
2. Plug these values into equation 2.15 to determine the rates of tunneling on and off the particle through each junction, Γ_1^\pm and Γ_2^\pm as a function of voltage for all values of n .
3. At each voltage, determine which value of n satisfies both conditions of equation 2.23. Assign the relative probability of the particle containing this number of excess electrons, $relative\rho(n_o, V)$ a value of 1. For particles <5 nm in diameter studied between -2.5 and $+2.5$ V, an easier approach can be taken: the $n = 0$ state has a valued probability at all voltages, so $relative\rho(0, V)$ can be assigned a value of 1 at all voltages.
4. Using equation 2.21 determine all other $relative\rho(n, V)$ values. Once all are determined, normalize these relative values using equation 2.19 to determine the absolute probability for each n value at each voltage, $\rho(n, V)$.
5. For each voltage, there is now a value for Γ_1^\pm , Γ_2^\pm , and $\rho(n, V)$ for all n values examined. These values can be applied to equation 2.2 to determine the steady state current at each voltage.

A procedure used in the software package Igor is shown in the Appendix. This routine allows $I(V)$ curves to be constructed using the above computational approach.

The user can change the junction parameters R_1 , R_2 , C_1 , C_2 , the temperature T , environmental charge on the particle, q_o , and an α term to account for any exponential co-tunneling events that may take place directly between source and drain electrodes.

The shape of the $I(V)$ curve changes in real-time as the user alters the input parameters.

Including an experimental $I(V)$ curve in the window with this calculated curve allows one

to tune the parameters until a good fit is met and in this way determine the junction parameters.

2.2 Current-voltage response as a function of input parameters

Section 2.1 provides the tools required to calculate $I(V)$ spectra for double tunnel junction systems. It is not intuitive from this derivation how each junction parameter will affect the $I(V)$ response of the system. In this section, calculated curves are presented and the relationship between curve shape and the various input parameters is derived.

2.2.1 Ideal systems

As a starting point, a curve calculated at absolute zero temperature with R_1 much greater than R_2 and C_1 greater than C_2 will be examined. Figure 2.3 was obtained by calculating the steady state current of the system at many different voltages as described in section 2.1 and then plotting these currents as a function of voltage. The rates of tunneling at 0.98V through each junction for several values of n excess electrons are shown in Figure 2.4. With two excess electrons on the particle, the only tunneling event that is allowed is for an electron to tunnel off the particle through junction 1. When the particle contains one excess electron, the particle can either gain an electron through junction 2, or an electron can tunnel off the particle through junction 1. The $n = 0$ state only allows for tunneling onto the particle through junction 2.

The probability of the particle existing in each of the three states shown, $\rho(n)$, makes sense when the rates of these tunneling events are examined. The $n = 0$ state quickly gains an electron to transform the particle to the $n = 1$ state. From here the

Calculated I(V) response of an ideal double tunnel junction

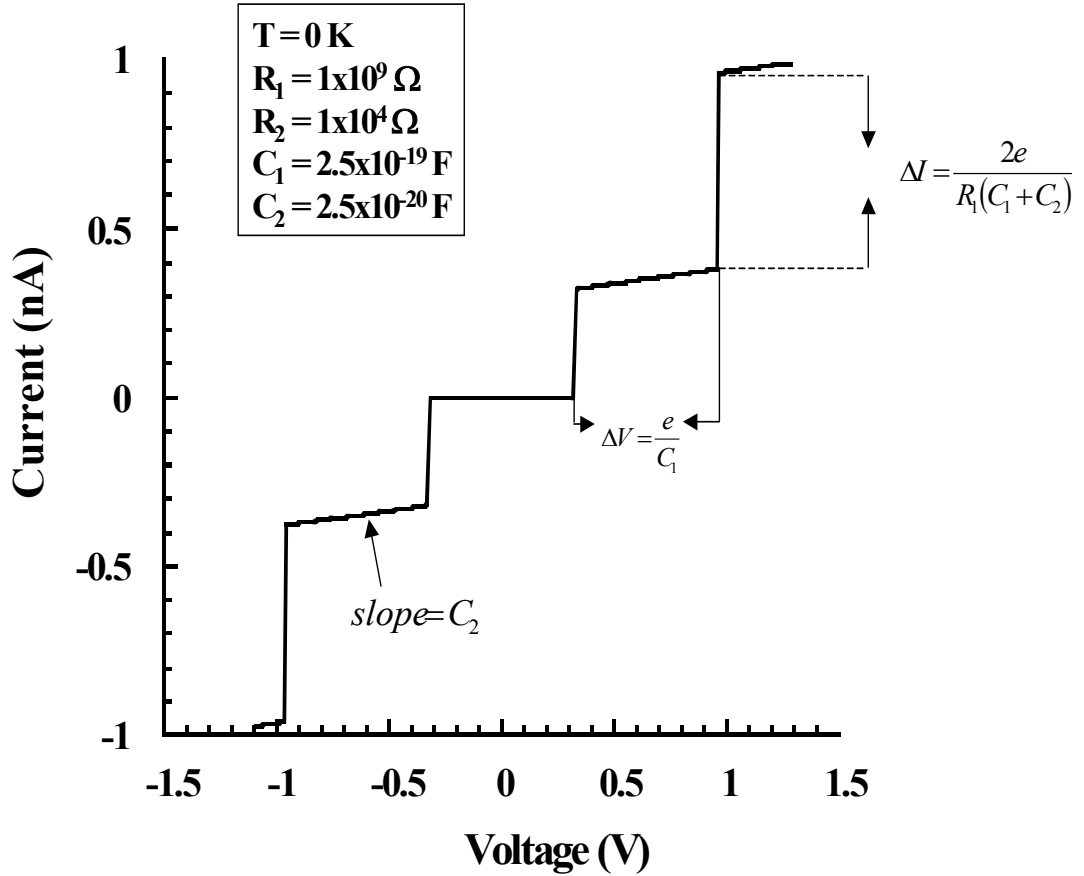


Figure 2.3 A current-voltage curve calculated using $T = 0$, $R_1 = 1 \times 10^9 \Omega$, $R_2 = 1 \times 10^4 \Omega$, $C_1 = 2.5 \times 10^{-19} \text{ F}$, $C_2 = 2.5 \times 10^{-20} \text{ F}$. The relationship between plateau width, plateau slope and initial current increase and the input parameters are shown.

particle can either lose an electron and return to the $n = 0$ state or gain an electron and increase the number of excess electrons to 2. The rate of tunneling onto the particle through junction 2 is much faster than the rate of tunneling off the particle through

junction 1 when $n = 1$, therefore it is much more probable that a particle with one excess electron under these conditions will gain an electron and climb to the $n = 2$ state.

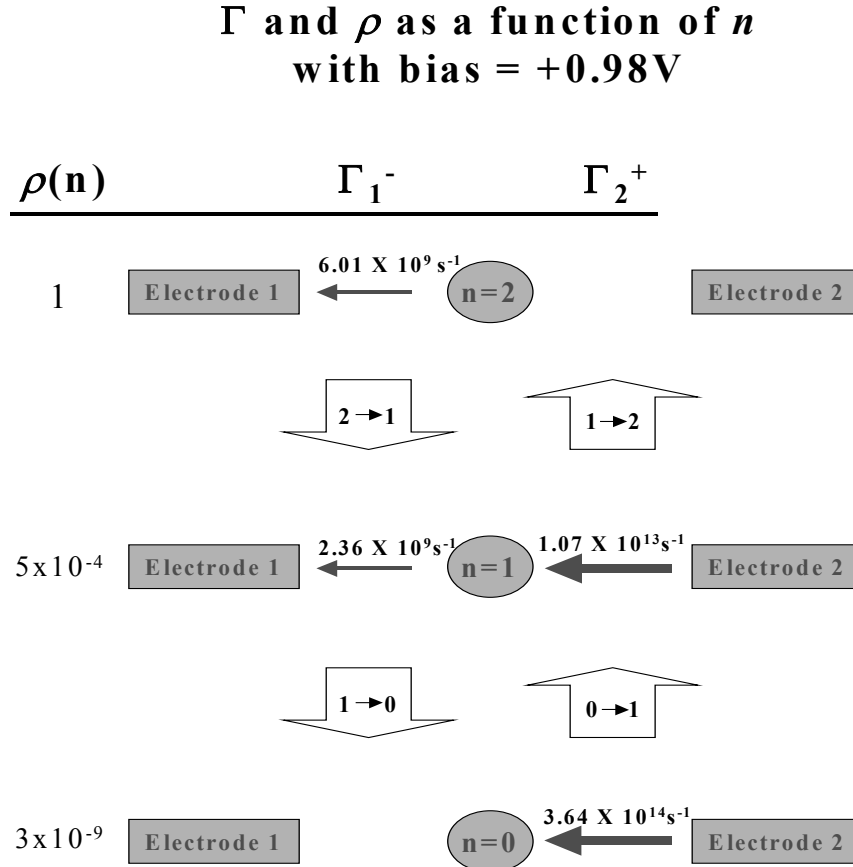


Figure 2.4 The rates of tunneling onto and off of the particle for the $n = 0, 1$ and 2 states are shown. An electron tunneling onto the particle through junction 2 will increase n to a value of $(n + 1)$ while an electron tunneling off the particle through junction 1 will cause a transition to the $(n - 1)$ state. Due to the much higher rate of transfer through junction 2, the most probable value for n at this voltage is 2. The probability of each state's existence at this voltage, $\rho(n)$ is also shown along the left side

The $n = 2$ state will then lose an electron slowly in comparison to the $n = 1 \rightarrow 2$ transition. Thus, the most likely cycle of events is for the particle in the $n = 1$ state to quickly gain an electron through junction 2 to raise the number of excess

electrons to 2, from which it will slowly lose an electron to return to the $n = 1$ state. The most probably state of the particle at +0.98 V is $n = 2$.

Figure 2.5 shows the same system under negative bias.

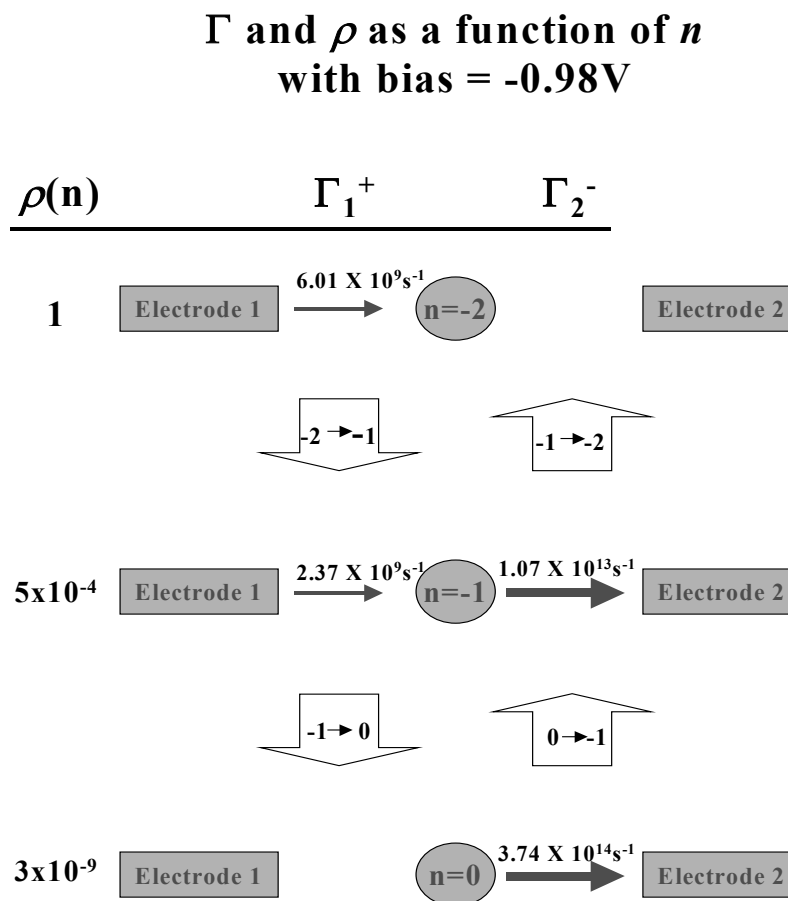


Figure 2.5 The tunneling rates at an applied bias of -0.98 V are shown for the $n = 0$, $n = -1$ and $n = -2$ states. It is clear that at this voltage, the $n = -2$ state is by far the most probable. The current through the system is then limited by the slow rate of tunneling onto the $n = -2$ particle to create the $n = -1$ state.

A similar cycle is produced with a rate-favored cycle of the $n = -1$ state quickly losing an electron through junction 2 to transform the particle into the $n = -2$ state where it slowly

gains an electron through junction 1 to return the particle to the $n = -1$ state. Thus the most probable number of excess electrons on the particle at -0.98 V is -2 . Two points should be clear from the above discussion

1. The most probable number of excess electrons (n_o) is determined by when the rate of tunneling through junction 2 becomes zero valued.
2. The current through the system is defined by the slow step, which is the rate of electron tunneling through junction 1.

Looking at equations 2.14 and 2.15 it can be seen that the rate of tunneling through junction 2 becomes non-zero when:

$$C_1 V > \frac{e(1+2n)}{2} + q_o \quad \text{equation 2.24}$$

For this condition to be held, n will have to increase from 0 to 1 when

$$V = \frac{e}{2C_1} + \frac{q_o}{C_1} \quad \text{equation 2.25}$$

After the first increase in n from 0, n will continue to increase at voltage intervals of

$$\Delta V = \frac{e}{C_1} \quad \text{equation 2.26}$$

in order to maintain the conditions of equation 2.24 that result in a non-zero rate through junction 2. These regularly spaced increases in n_o are what result in the current steps of figure 2.3. Looking at equations 2.14 and 2.15 again to see how the rate of tunneling through junction 1 is changed by an increase in n it is seen that:

$$\frac{\partial \Gamma_1}{\partial n} = \frac{e}{2R_1(C_1 + C_2)} \quad \text{equation 2.27}$$

Thus, at voltage intervals of e/C_1 , the current will increase by $e/2R_1(C_1 + C_2)$. Figure 2.6 shows current voltage curves for two systems where R_1 differs by a factor of two.

I(V) response as a function of R_1

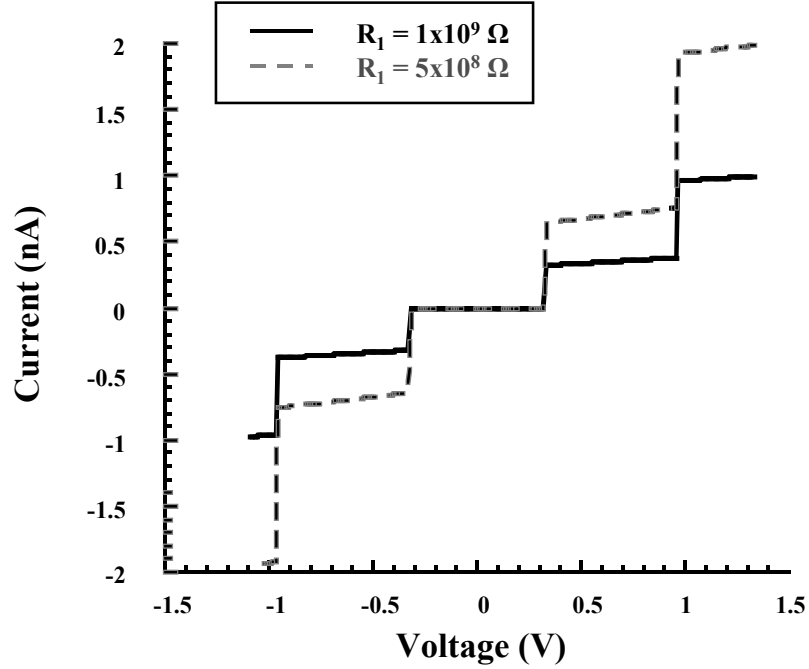


Figure 2.6 Calculated I(V) curves with $R_1 = 1 \times 10^9 \Omega$, and $R_1 = 5 \times 10^8 \Omega$. For both curves $T = 0$, $C_1 = 2.5 \times 10^{-19} \text{F}$ and $C_2 = 2.5 \times 10^{-20} \text{F}$.

Notice the larger step heights resulting from the lowered resistance. The rate of tunneling through junction 1 also increases with applied voltage:

$$\frac{\partial \Gamma_1}{\partial V} = C_2 \partial V \quad \text{equation 2.28}$$

This results in a linear increase in current with a slope of C_2 that these current spikes are superimposed on. Figure 2.3 has these three features clearly labeled.

The preceding example showed how an ideal coulomb staircase can be produced from a double tunnel junction. Most experimental data obtained from such structures

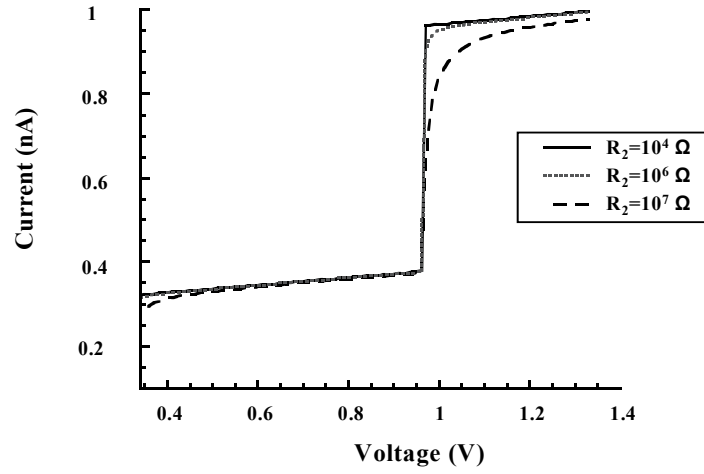
deviate significantly from this ideal sharp increase in current superimposed on a background current with a gentle positive slope. This is because most measurements are taken under conditions where the time constant of the first tunnel junction, R_1C_1 , is much closer in value to that of the second junction, R_2C_2 . The observations that result from these deviations from ideal conditions will now be examined.

2.2.2 Current-voltage response as a function of R_2

It was shown in the previous section that changes in R_1 result in changes in the observed step height. Figure 2.7 shows a single step in current-voltage curves as a function of R_2 . R_1 is kept constant for all curves and R_2 is progressively increased. The result is a rounding of the current step. This can be rationalized by looking at the rates of tunneling through each junction for the n_o and (n_o-1) states (bottom of Figure 2.7). As the rates of tunneling come closer to one another, the probability that the $n = 1$ state will lose an electron through junction 1 and send the particle to the $n = 0$ state is much closer to that of the $n = 1$ state gaining an electron through junction 2 and increasing n to 2. This causes the distribution of $\rho(n, V)$, the probability of the particle to be in the n th state at a particular voltage, to increase significantly (Figure 2.8). This increase in probability for the (n_o-1) state and (n_o-2) state causes the decrease in current and curvature in the transition region. The rates become most similar at the transition region, and this is where the contributions of these lower n states are seen the most.

a)

I(V) response as a function of R_2



b)

Γ and ρ as a function of R_1/R_2 Bias = 0.98V, $R_1 = 1 \times 10^9$

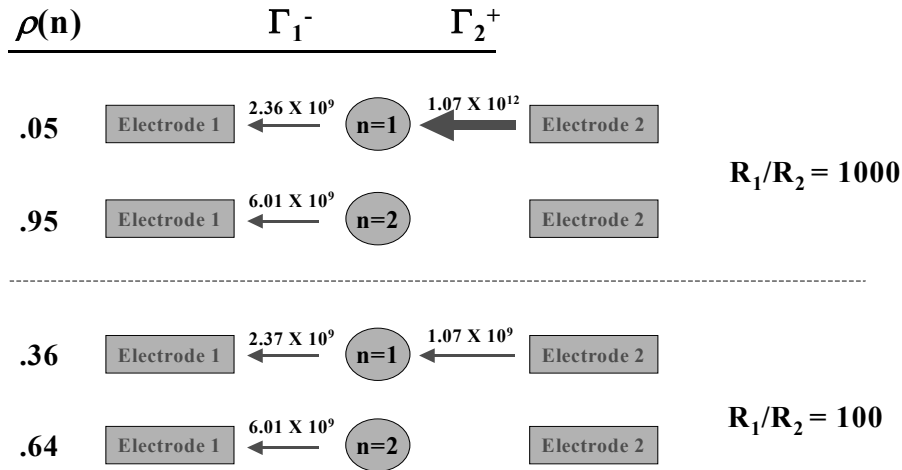


Figure 2.7 a) I(V) curves with $R_1 = 10^9 \Omega$, $C_1 = 2.5 \times 10^{-19} \text{ F}$, $C_2 = 2.5 \times 10^{-20} \text{ F}$ and $R_2 = 10^4 \Omega$, $10^6 \Omega$, and $10^7 \Omega$. Notice the rounding at the top of the transition region as R_2 approaches R_1 in value. b) Shows the rates of tunneling at 0.98V and $n = 1$ and 2 for the above systems with $R_2 = 10^6 \Omega$, and $10^7 \Omega$. Notice the $n = 1$ state of the lower system. Tunneling off the particle to produce the $n = 0$ state is now slightly faster than production of the $n = 2$ state. The $n = 0$ state can still only transition back to the $n = 1$ state, so the most probable state is still $n = 2$, but it is significantly much less probable now. This effect is seen most strongly in this transition region.

$\rho(n)$ as a function of R_2 at 0.98 V

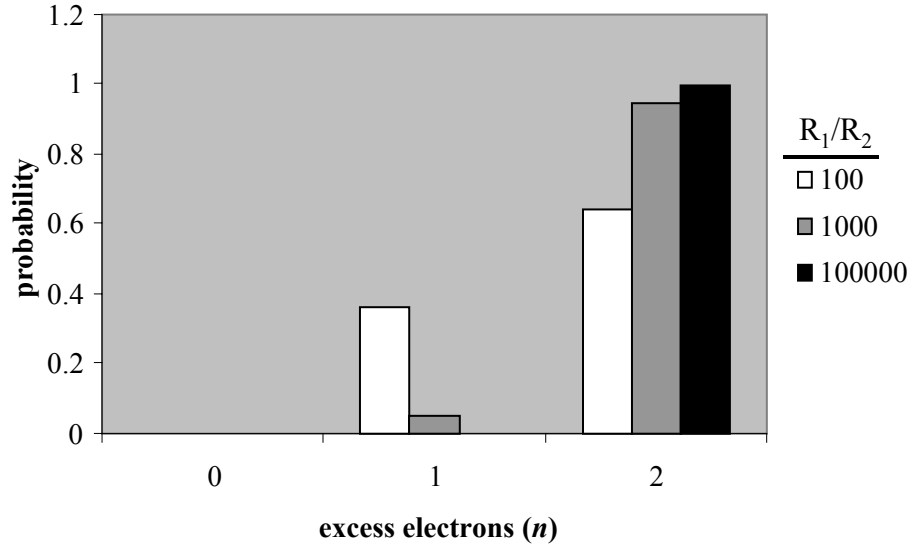
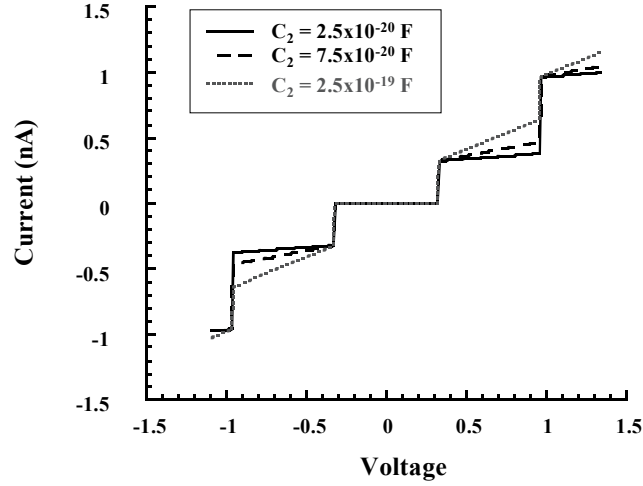


Figure 2.8 The probability of the $n = 0, 1$ and 2 states are shown for the three curves in Figure 2.7 at a bias of 0.98V. This increase in the probability of the $n = 1$ state in the transition region is what causes the decrease in the current response and rounding of the $I(V)$ curve.

2.2.3 Current voltage response as a function of C_2

Figure 2.9 shows current-voltage curves as function of C_2 . Equations 2.27 and 2.28 show that an increase in C_2 will 1) decrease the magnitude of the initial current step that occurs at the $n_o \rightarrow n_o + 1$ transition and 2) increase the slope of the current increase in the plateau region. Both of these are observed in figure 2.9. Interestingly, the total change in current within a voltage range of e/C_1 (one complete step-cycle) is the same independent of C_2 . This is not simply due to the fact that the increase in slope accounts for the smaller current jump due to the change in n , but is also a result of a change in the probability distribution of n (bottom of figure 2.9). The complication of the self-consistent process used to calculate $\rho(n, V)$ precludes a simple derivation for why the total

a) **Calculated I(V) response as a function of C_2**



b) **Probability distribution of n as a function of C_2**

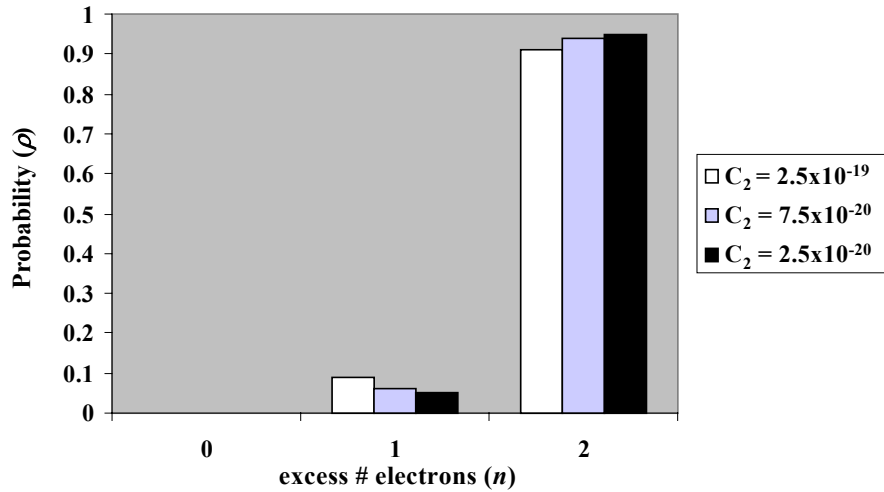


Figure 2.9 a) Current-voltage curves with $R_1 = 10^9 \Omega$, $R_2 = 10^4 \Omega$, $C_1 = 2.5 \times 10^{-19}$ F and various values of C_2 showing the affect on change in current at the transition region and plateau slope. Interestingly, the total current gained in one full step cycle is independent of C_2 . b) The probability distribution of excess electrons is also affected by changes in C_2 . This is for a double tunnel junction with $R_1 = 10^9 \Omega$, $R_2 = 10^6 \Omega$, and $C_1 = 2.5 \times 10^{-19}$ F at 0.98 V.

increase in current upon a voltage change of e/C_1 is independent of C_2 .

2.2.4 Effect of temperature on the current-voltage response

Increasing the temperature from absolute zero causes an increase in the probability distribution of excess electrons on the particle. This results in curvature at the transition region (figure 2.10).

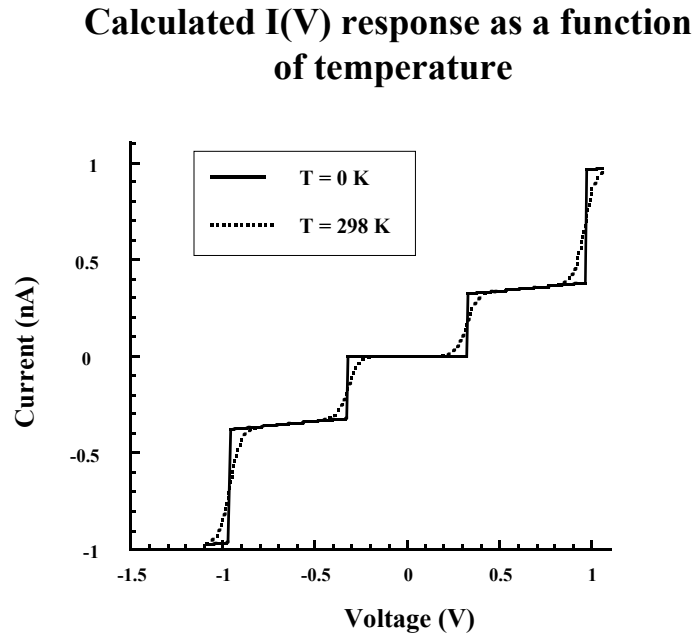


Figure 2.10 Current-voltage curves calculated using $R_1 = 10^9 \Omega$, $R_2 = 10^4 \Omega$, $C_1 = 2.5 \times 10^{-19} \text{ F}$, and $C_2 = 2.5 \times 10^{-19} \text{ F}$. The solid curve is at absolute zero while the dotted line is at room temperature. Notice that the $n \rightarrow n + 1$ transition now begins earlier because thermal energy can begin to populate the higher state before equation 2.24 is satisfied.

Unlike the curvature induced by similar values of R_1 and R_2 discussed in section 2.2.3, temperature imparts curvature at both the top and bottom of the transition region. This is because with thermal energy, there is now a probability that a tunneling event can occur

from an electrode of low Fermi energy to one of a higher Fermi energy level because of the population distribution that now exists for the Fermi surfaces. The higher the temperature the greater this curvature will become. When the thermal energy, $k_b T$ approaches the charging energy of the metal island e^2/C_1 , the curvature completely washes out any staircase features and single electron charging is no longer observed in the system.

2.3 Conclusions

An analytic approach to calculating the current voltage response of double tunnel junction structures has been presented. The results of these calculations help one to understand how physical and chemical changes of the structure can alter the current-voltage response. Figure 2.11 shows a calculated curve that comes much closer to approximating experimental data than those normally shown.

Calculated room temperature I(V) curve with typical junction parameters

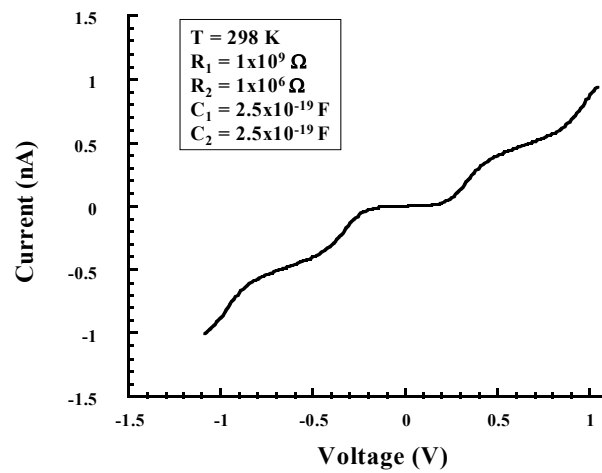


Figure 2.11 Current-voltage curve calculated using realistic experimental parameters.

This curve deviates from the ideal sharp coulomb staircase in many ways. The onset of the transition from $n \rightarrow n \pm 1$ shows significant curvature from both temperature effects and the similarity in junction resistances. The plateau region shows significant slope from a relatively large junction 2 capacitance. For experimental curves of this nature, the only way to accurately determine all junction parameters is to use the analytical method of section 2.1 to fit the data. Much can be learned without an accurate fit though. A measurement of the voltage width of a full step cycle will allow one to calculate the capacitance of junction 1 quantitatively using equation 2.21. Also, as seen in figure 2.9, the measurement of the change in current within one full step cycle (other than the first step) can allow one to determine the relative resistance of junction 2. This is not a quantitative determination because it is a convolution of the resistance and the probability distribution of excess electrons on the particle, which for most real systems is significant (as seen by the slope and curvature of the transition region) and means that two systems can only be compared relative to one another.

2.4 Chapter Two References

1. a) M. Amman, K. Mullen and E. Ben-Jacob, *J. Appl. Phys.* 1989, **65**, 339. b) M. Amman, R. Wilkins, E. Ben-Jacobs, P. D. Maker, and R. C. Jaklevic, *Phys. Rev. B*, 1991, **43**, 1146. c) K. Mullen, E. Ben-Jacob, R. C. Jaklevic and Z. Schuss, *Phys. Rev. B.*, 1988, **37**, 98. d) R. Wilkins, E. Ben-Jacob and R. C. Jaklevic, *Phys. Rev. Lett.*, 1989, **63**, 801. e) A. E. Hanna and M. Tinkham, *Phys. Rev. B.*, 1991, **44**, 5919. f) J. Lamb and R. C. Jaklevic, *Phys. Rev. Lett.*, 1969, **22**, 1371.
2. D. V. Averin and K. K. Likharev, "Mesoscopic Phenomena in Solids" ed. B. L. Altshuler, P. A. Lee, and R. A. Webb, North Holland, New York, 1991, 173. (this reference is mis-cited in all of the above references).

Chapter 3

Operation of the Digital Instruments Nanoscope IIIa multimode Scanning Tunneling Microscope.

This chapter will describe the instrumentation used throughout this dissertation. The scanning tunneling microscope has established itself as a standard technique for surface characterization. Detailed descriptions of its operation can be found in numerous sources¹, therefore the current discussion will be limited to the tunneling process that controls the tip-substrate separation and the unique qualities of the Digital Instruments Nanoscope IIIa instrument used.

3.1 STM operation

As its name suggests scanning tunneling microscope uses a tunneling current established between an atomically sharp tip and conductive substrate to probe the substrate's surface morphology and electronic structure. A piezo electric scanner causes the tip to raster across the surface while the instrument monitors changes in the tunneling current. Changes in the current can result from either a change in tip/substrate separation or a change in the local density of states in the substrate. The sharpness of the tip and sensitivity of tunneling current to very small changes in electrode separation and local density of states allows for a view of the substrate surface with atomic resolution. The work described in this dissertation used instrument settings that caused the instrument to keep the tunneling current between the tip and substrate constant by making adjustments in the tip/substrate separation with the piezo scanner and the instrument produces an image of the adjustments required to maintain this current. This is called constant-current mode of operation.

The tunneling current is established by applying a voltage bias between the tip and substrate. Tunneling occurs when an electron passes through an energy barrier when

that electron doesn't have sufficient energy to overcome this energy barrier (figure. 3.1).

Tunneling occurs when the two electrodes are close enough in space that their surface waves overlap. While a metallic surface seems to be a well defined boundary on the macroscale, consisting of a region that is clearly metallic electrode and an immediate change to region of atmosphere, there is a small, nanoscopic region extending out from the surface where the wave of any surface electrons decay exponentially. When two electrodes are brought close enough together, these surface waves can overlap, allowing an electron to tunnel from one electrode into the other, even though it never obtains the energy associated with an electron's existence in the barrier region (E_b in Figure 3.1). From this picture it can be seen that as the two electrodes are moved away from one another, the overlap of the surface waves will decay exponentially. The solution of the Shroedinger equation inside the barrier is:

$$\Psi(z) = \Psi(0)e^{-\kappa z}$$

equation 1.1

$$\kappa = \frac{\sqrt{2m(V - E)}}{\hbar}$$

where m is the mass of an electron, V is the potential in the barrier, E is the energy of the electron and z is the distance between the two electrodes. This decrease in overlap results in a decrease in the probability of tunneling for the electron and ultimately a decrease in the tunneling current observed between the two electrodes with a given applied bias.

$$I \propto e^{-2\kappa z}$$

equation 1.2

Electrode separation as a function of applied bias and operating current

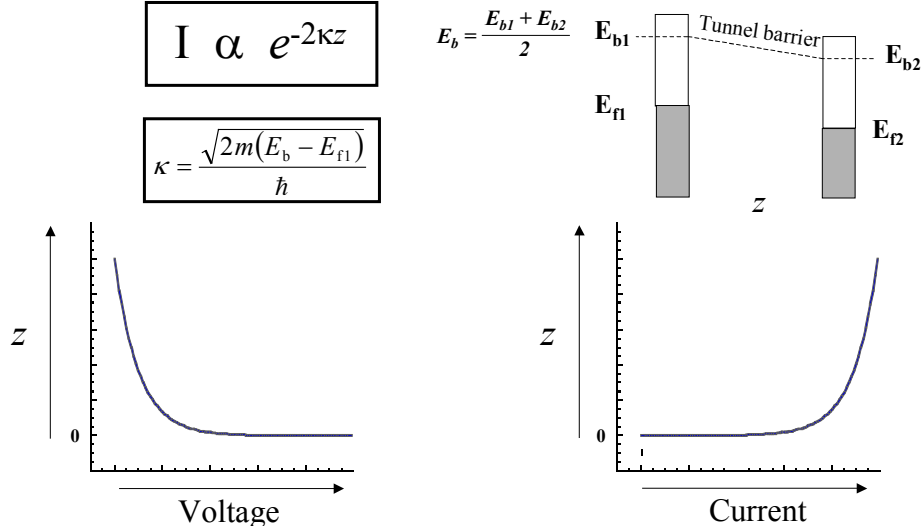


Figure 3.1 Two electrodes separated by $< 10\text{nm}$ by an insulating material are shown. The operation of the STM is based on the distance vs. Voltage and distance vs. Current plots shown at the bottom, where changes in current with a constant applied bias allow the user to map changes in tip/substrate separation. The applied bias and setpoint current chosen will determine the tip/substrate separation during constant-current mode operation.

Figure 3.1 shows the electrode separation (z) as a function of tunneling current with constant applied bias, and separation as a function of applied bias while constant tunneling current is maintained. It is seen from equation 1.1 that these are both exponential functions. An increase in STM operating bias will result in larger tip-substrate separation while a lower operating current (setpoint current) result in greater tip-substrate separation. It's important to note that the tunneling current is also a function of the medium in the barrier (barrier height) and the local density of states of both the tip and substrate. These must always be considered before blindly assigning experimental observations as resulting from an increase or decrease in tip-substrate separation.

3.2 Digital Instruments Nanoscope IIIa

The Digital Instruments Nanoscope IIIa multi-mode STM used in this dissertation has several unique ways of interfacing with the user that must be described in detail². This instrument allows for the collection of current vs. voltage spectroscopic data in what is termed continuous imaging tunneling spectroscopy mode (CITS). In this mode, the STM images the surface as usual, but 1024 times during the image capture, the feedback loop is turned off, tip-substrate held at constant separation, tip-substrate bias swept and the current response collected. These current-voltage curves are collected in a regularly spaced 32x32 array in the x-y plane of the image. Figure 3.2 shows the output of a typical CITS experiment. On the left hand side is the standard STM image. In the top right corner is a 32x32 pixel matrix that represents the spatial orientation of the current-voltage curves collected. The lower right shows the spectra obtained in the selected pixel. Having this pixelated image associated with the collected I(V) curves provides the user with a general idea of what surface feature the curve was collected near.

The user can define the number of current-samples taken during a voltage sweep, the voltage range swept, and the time between each sample within the individual spectra. The user cannot control where within the image the curves are collected or the direction of the bias sweep.

Figure 3.3 shows how the user-definable parameters adjust the data collection protocol. The voltage offset determines where the center of the voltage window is with respect to 0V. The sweep width defines the potential range as Voltage Offset – $\frac{1}{2}$ (sweep width) to Voltage Offset + $\frac{1}{2}$ (sweep width). The number of samples defines the number of times the current is sampled within a given voltage sweep. The sample period defines

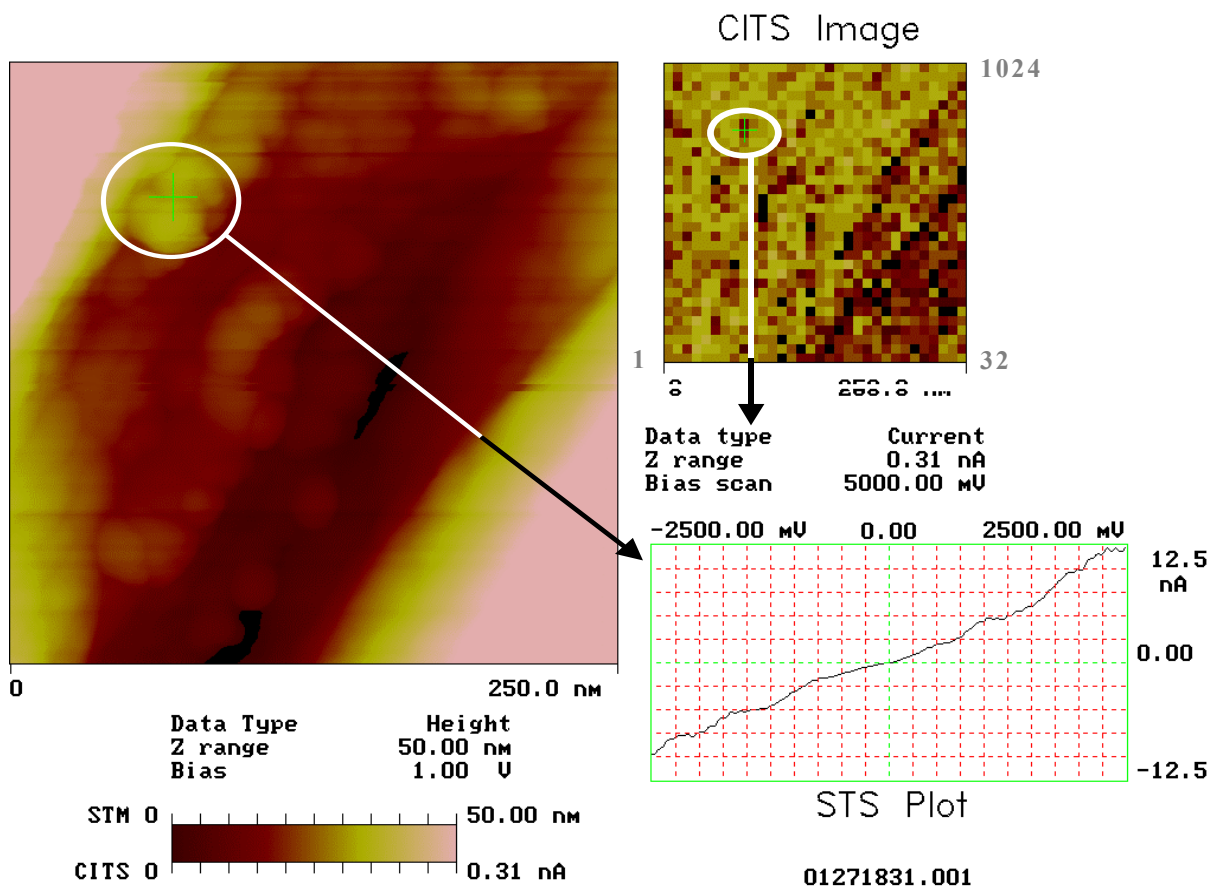


Figure 3.2 A screenshot from the Digital Instruments Nanoscope IIIa in CITS mode. The image on the left is the standard topographic image. The pixilated image in the upper right corner represents the 1024 I-V curves collected. The I-V curve in the lower right corner corresponds to the pixel and location in the topographic image marked by the white circles. The pixel-numbering scheme begins with 1 in the lower left hand corner counting across to 32 at the lowest right corner. The second row then begins with 33 on the left column and continues on to 64. This continues until pixel 1024 is reached in the top corner of the pixel image.

the time between sample points. This results in a total time required for a curve to be collected of

$$\text{Time} = \# \text{ Samples} * \text{Sample Period} \quad \text{equation 3.3}$$

And a sweep rate of

$$\text{Sweep Rate (V/s)} = (\# \text{ Samples} * \text{Sample Period}) / (\text{Sweep Width}) \quad \text{equation 3.4}$$

Parameters controlling voltage sweep during CITS operation

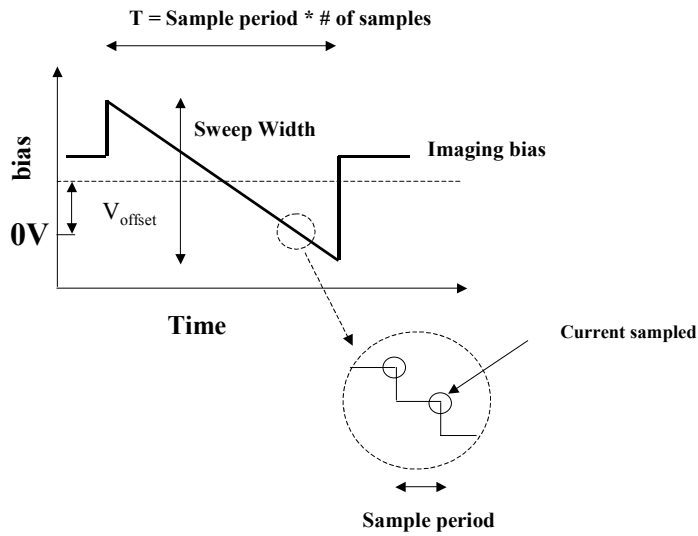


Figure 3.3 The parameters controlling the voltage sweep during I(V) data collection in CITS mode are shown. It is important to note that the potential is sweeps from positive to negative, that the potential is changed in a step-wise fashion with current samples being taken at the end of the voltage-hold period, and that the sweep rate in V/s is a function of both the sample period input parameter and the number of samples input parameters.

A very important software glitch must be noted: for the sample period to be altered, it requires two input cycles. Anytime the instrument is engaged, no matter what the “Sample Period” setting reads on the screen, the sample period is automatically set at 20us. To change from this setting the user must first enter an arbitrary new sample period. This ONLY engages the software to allow for the sample period to be changed. After this first arbitrary number is entered, the user may now input a new sample period that will finally take effect. Changing the sample period has a dramatic effect on the rate of imaging, so this can be used as a check to see if the sample period has actually been changed or not.

Sweep rate is an important consideration when working with low-current electronics. Low current electronics often have limited bandwidth due to noise suppression filters that are required for the low current operation. One must always be certain that the signal attempting to be measured lies within the bandwidth of the associated measurement electronics. For example, the booster box that is now in use with the low-current head on the DI Nanoscope IIIa has a maximum filter cutoff frequency of 1.5kHz. If one were to attempt to measure a coulomb staircase with a voltage window of –2.5V to +2.5V, expecting a step-width (cycle) of 600mV with instrument settings of 256 sample points and sample period of 50 μ s, one would first want to calculate the frequency of the signal that is hoped to be measured. In this instance, the total time of the voltage sweep is:

$$256 \text{ samples} * 50\mu\text{s}/\text{Sample} = 12,800 \mu\text{s}$$

The voltage scale can now be converted to a frequency scale:

$$5\text{V} / 12,800 \mu\text{s} = 390 \text{ V/s}$$

This means that a signal like the coulomb staircase proposed with a voltage cycle of 600mV will then have a frequency of:

$$\frac{390V/s}{0.600V} = 650s^{-1}$$

This frequency of 0.650 kHz falls within the allowable range of operation for the electronics. If one were to examine a coulomb staircase with step-widths narrower than 250 mV, the instrument would not be able to detect the signal.

CITS data can be exported from the DI machine as an ASCII file. It is important to know exactly which I(V) curves are desired from the CITS image when doing this. The ASCII file consists of a header file describing the instrument settings used during the experiment followed by rows of numbers that include the I(V) data. The CITS data generally start around row 400 +/- 20 rows. Each I(V) curve consists of a row of numbers associated with the current response. These numbers represent the 16-bit conversion that the DI instrument performs on the voltage output the current head provides. To convert this information to current in nanoamperes the following function must be performed on the raw numbers:

$$\text{Current} = (\text{DI output} * \text{sensitivity} * 20) / 65536 \quad \text{equation 3.5}$$

The I(V) curves are listed in order in this ASCII file, with pixel one being in the lower left corner of the pixel image, 32 being in the lower right corner, 33 being the leftmost

pixel in the second row from the bottom and so on until the 1024th pixel is reached in the top right corner of the pixel image. The user can find the desired curve while looking through the CITS data in the DI software, count the pixel number, and then find this curve in the ASCII file by counting down that number of rows from the first row corresponding to data in the file. Trial and error is sometimes required to find the row of data corresponding to pixel one: plot the data until a curve resembling the data seen in pixel one is found.

3.3 Conclusions

A very brief overview of the operation of an STM has been presented to allow the reader to understand the experiments that follow. If the reader is new to the world of scanning probe microscopies, the references provided will give a more detailed picture of instrument operation. Critical information for understanding the following experiments is that tip-substrate separation is controlled by instrument setpoint current. Particular anomalies discovered while using the Digital Instruments STM have been presented. There are certainly many more unique features of this instrument waiting to be discovered by the ambitious user.

3.4 Chapter Three References

1. a) D. Bonnell ed., "Scanning Probe Microscopy and Spectroscopy Theory, Techniques, and Applications" 2nd edition, Wiley-VCH, New York, **2001**. b) R. Wiesendanger, "Scanning Probe Microscopy", Cambridge University Press, New York, **1994**. c) C. J. Chen, "Introduction to Scanning Tunneling Microscopy", Oxford University Press, New York, **1993**.
2. Much of this information was obtained through discussions with Pat McPhail, DI tech support representative. Other excellent sources of information on the particulars of CITS operation include Dr. R. Lloyd Carroll, Ryan R. Furrier, Dr. Stephan Kraemer, Dr. Grace Credo, and R. Andrew Wassell.

Chapter 4

Current-voltage measurements of individual 5 and 10 nm diameter gold nanoparticles with a scanning tunneling microscope

4.1 Introduction

The work in this dissertation uses a scanning tunneling microscope to measure the electronic properties of individual gold nanoparticles. The approach is to start with a gold surface that has been modified with an organic self-assembled monolayer, cast particles on this surface, then probe the surface with an STM tip. Once an area of the substrate is found which contains a reasonable number (10-50) of dispersed nanoparticles the instrument is placed in CITS mode and current-voltage data collected. Measurements made when the STM tip is close to a gold nanoparticle should result in single electron tunneling behavior¹, where one tunnel junction is from tip to particle and the second is from the particle to the substrate (Figure 4.1).

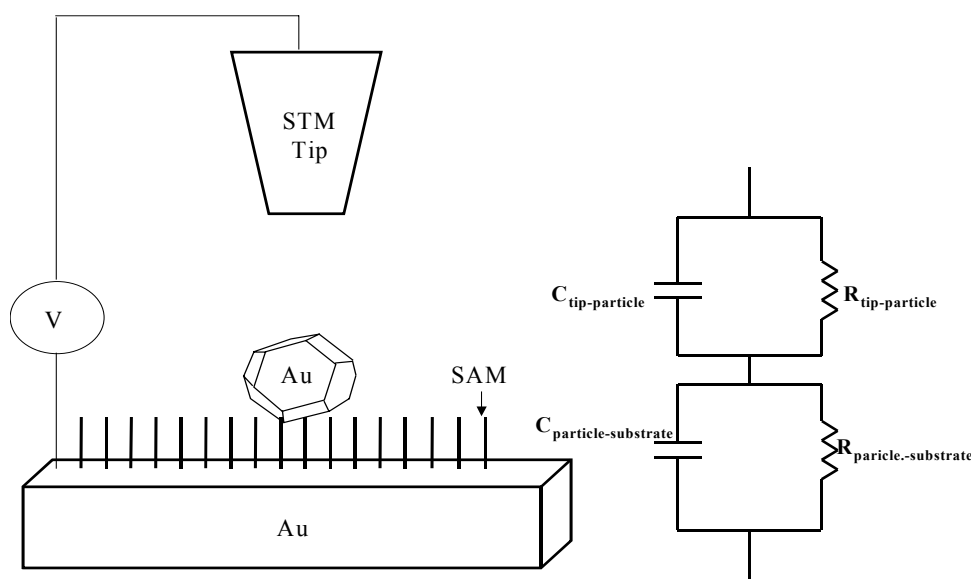


Figure 4.1 Cartoon illustrating the desired physical configuration for measuring single electron tunneling $I(V)$ response of individual gold nanoparticles with an STM tip.

The first experiments with this system were aimed at measuring a non-linear response near a gold particle and then asserting that this response was in fact due to single

electron tunneling through the tip-particle-substrate double tunnel junction structure. The size of the gold particle is one of the easiest parameters to control in this system, and will result in a predictable change in charging energy of any coulomb staircase behavior observed in the current-voltage data². This is because the capacitance of each tunnel junction is partially defined by the radius of the particle³.

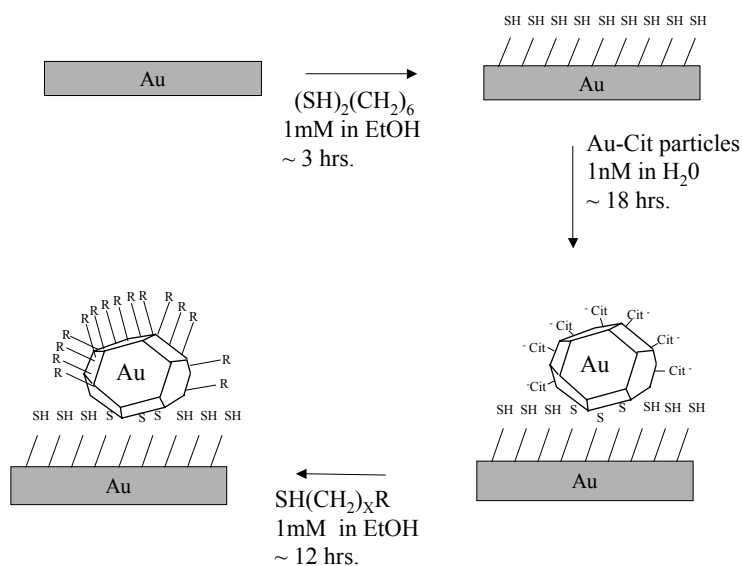
$$C = 4\pi\epsilon_0\epsilon\left(1 + \frac{r}{2L}\right) \quad \text{equation 4.1}$$

where ϵ_0 is the vacuum permittivity, ϵ is the permittivity of the material between the particle and electrode, r is the particle radius and L is the distance separating the particle and electrode. As the particle size is increased, the junction capacitances will also increase resulting in narrower voltage step-widths in any observed coulomb staircase data^{1d}. In this chapter current-voltage measurements of 5 and 10nm gold nanoparticles are taken to confirm that these STM based measurements are valid for measuring the single electron tunneling properties of individual gold nanoparticles.

4.2 Experimental

Glass slides with 50 angstroms of Ti as an adhesion layer and 1000 angstroms of gold evaporated on one surface were used as substrates. Substrates were prepared (Scheme 4.1) by first cleaning the gold slide in piranha solution for one minute followed by immersion in a ~10 mM solution of hexanedithiol in ethanol. After copious rinsing with ethanol and drying, the gold slide was then allowed to incubate in a solution of 5nm citrate

capped gold nanoparticles as received from BBI for ~4 hours. In this chapter, the native citrate capping ligands were left on the particle surface, but this citrate shell can be replaced with a thiol monolayer by immersing the slide in a solution of the desired displacing molecule for ~30 minutes. This will be done in future chapters.



Scheme 4.1 Cartoon of substrate preparation in order to obtain organic SAM modified gold surfaces containing a dispersed coating of individual citrate-capped gold nanoparticles. The citrate-capping ligand can be replaced with a thiol after particles are attached to the surface by incubating the slide in a the appropriate thiol solution.

The slide was then rinsed with water, dried and attached to a steel puck via conductive silver paint (Alfa Aesar). The substrates were probed with a Digital Instruments Nanoscope IIIa using cut Pt/Ir.

4.3 Results

A representative image of 5nm citrate-coated particles cast on a hexane dithiol monolayer is shown in Figure 5.2. Also shown are typical current-voltage curves collected near a particle and away from particles. Non-linear response resembling a coulomb staircase is seen only in curves collected near a gold particle. The average voltage step-width of twenty-eight curves taken near 5nm particles was 542 ± 34 mV.

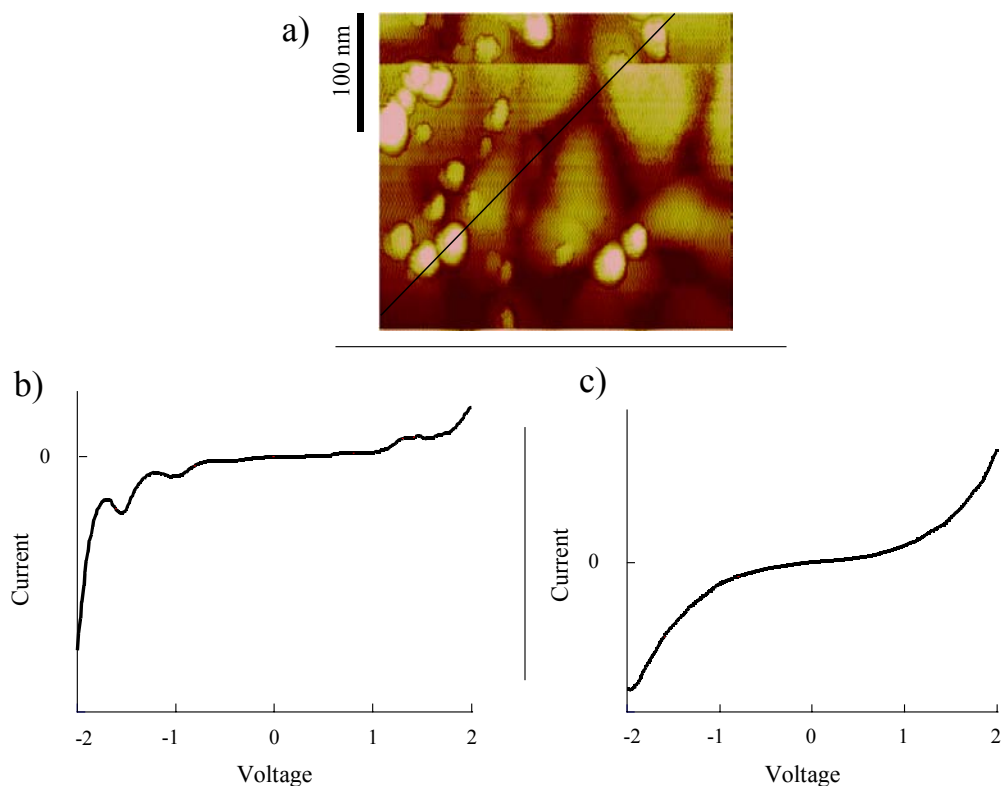


Figure 4.2 a) An STM image of 5nm citrate-capped particles on a hexane dithiol modified gold slide (bias = 400mV, setpoint current = 1nA) b) an I(V) curve measured when the STM tip was near a particle and c) an I(V) curve taken when the tip was away over a particle-free area of the surface.

Substrates prepared with 10nm gold nanoparticles show similarly shaped nonlinear current-voltage curves collected near the particles. The first derivative of I-V curves of

5nm and 10nm particles are shown in Figure 4.3. In the derivative plot, each step in the coulomb staircase is now seen as a peak. Ten curves taken near 10nm particles gave an average step width of 334 ± 38 mV.

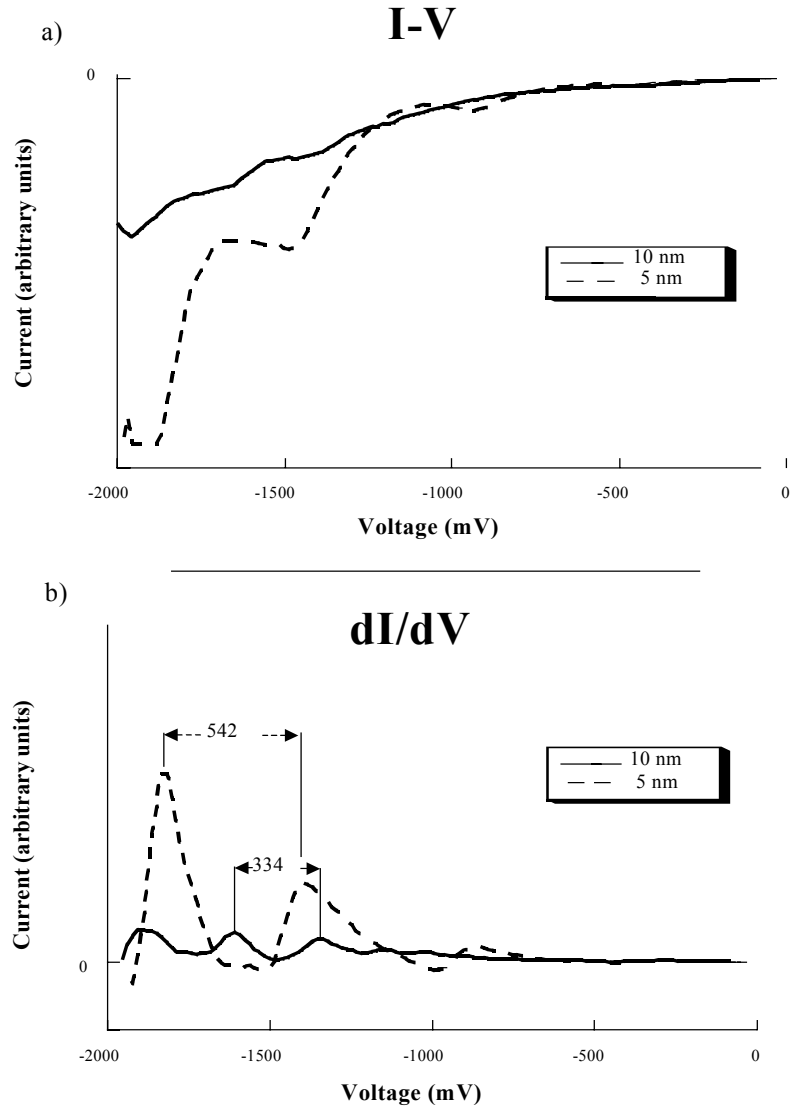


Figure 4.3 a) $I(V)$ curves over 5nm and 10nm citrate-capped particles in air. b) the first derivative with respect to voltage clearly shows the difference in step width for the two particle sizes.

4.4 Conclusions

The fact that non-linear I-V response is only observed near a gold particle, the voltage step widths show a narrow distribution for a given particle diameter and that the width decreased as particle diameter increased all support the hypothesis that the nonlinear response of these I(V) curves is due to single electron tunneling through individual gold particles. It is interesting to note that for a CITS image collected on similarly concentrated substrates of 5 nm and 10 nm particles, the 5nm sample will produce a higher number of curves showing single electron tunneling behavior, and those curves also show sharper transitions from one current state to the next. This agrees with the fact that the 10nm particles are approaching the thermal limits associated with observable single electron tunneling at room temperature. Probing gold nanoparticles cast onto monolayer-modified substrates with an STM appears to be a valid method for examining their single electron tunneling properties

4.5 Chapter Four References

1. a) L. E. Harrell, T. P. Bigioni, W. G. Cullen, R. L. Whetten and P. N. First, *J. Vac. Sci. Technol. B* 1999, **17**, 2411. b) R. P. Andres, T. Bein, M. Dorogi, S. Feng, J. I. Henderson, C. P. Kubiak, W. Mahoney, R. G. Osifchin and R. Refenberger, *Science*, 1996, **272**, 1323. c) R. S. Ingram, M. J. Hostetler, R. W. Murray, T. G. Schaaff, J. T. Khoury, R. L. Whetten, T. P. Bigioni, D. K. Guthrie and P. N. First, *J. Am. Chem. Soc.*, 1997, **119**, 9279.
2. P. J. Thomas, G. U. Kulkarni, C. N. R. Rao, *Chem. Phys. Lett.* 2000, **321**, 163.
3. D. L. Feldheim, K. C. Grabar, M. J. Natan and T. E. Mallouk, *J. Am. Chem. Soc.*, 1996, **118**, 7640.

Chapter 5

Single electron tunneling measurements of gold nanoparticles in solution: the role of capping-monolayer on determining the sensitivity of a particle's electronic properties to changes in the local chemical environment

5.1 Introduction

To date, most single electron tunneling measurements have been made at low temperatures in ultra-high vacuum environment¹. These measurements provide highly reproducible curves that are very easy to model due to limited thermal effects and controlled surface chemistry. Ten years of study in this clean environment have provided a solid foundation in understanding the role island size, tunnel junction asymmetry, and gate electrode potential play in defining the current-voltage response of these systems. This information is critically important for visualizing the relevance single electron tunneling structures may have in future device technologies. With this fundamental knowledge in hand, single electron tunneling can now be studied in more diverse and dynamic environments in order to gain an understanding of the challenges that will be faced in implementing proposed technologies (i.e. memory cells, sensors)². A first step in this direction is to measure single electron charging events of gold nanoparticles in solution phase and to examine what effect, if any, the dielectric of that solution has on the charging energetics of the system.

STM measurements are difficult to perform in solvents of high dielectric constant because leakage current is higher than the tunneling current required for proper feedback operation³. Standard materials used for electrical tip insulation are soluble in organic solvents, and measurements in water have been difficult to perform routinely in our lab. An easier way to examine single electron charging of gold nanoparticles in solutions of high dielectric constant is through differential pulse voltametry (DPV). DPV measurements of solutions of size monodisperse gold nanoparticles result in current peaks associated with single electron charging of the gold particles⁴.

$$E_{\text{peak}} = E_{\text{pzc}} + (z + 0.5e) / C_{\text{clu}} \quad (5.1)$$

These peaks are observable only in size monodisperse solutions where the distribution of charging energies of the particles is small. The voltage separation of these peaks is similar to the voltage step width observed in the I(V) response of an individual gold particle. The important difference is that the voltage separation of DPV charging events is a measure of the double-layer capacitance of the particle, not the capacitance of an individual tunnel junction.

Results are described for STM current-voltage measurements of individual citrate and octanethiol coated particles in dodecane and chloroform. To observe solvent related changes in particle charging energies for higher dielectric solvents, DPV measurements were made on solutions of triphenylphosphine-coated particles and octanethiol coated particles in toluene/acetonitrile mixtures ranging from 1:3 to 2:1 toluene to acetonitrile respectively.

5.2 Experimental

Scanning tunneling microscope measurements were performed with cut Pt/Ir tips. These tips were not insulated in any way. Substrates containing 5nm citrate-capped particles were prepared as described in Chapter 3. Substrates containing octanethiol capped particles were prepared by first immobilizing citrate capped particles on a dithiol surface, then rinsing the substrate with water, drying and incubating in a ~10 mM

ethanolic solution of octanethiol for ~30 minutes. A Teflon solution cell was attached to the top of the substrate with an o-ring seal to allow immersion of both tip and substrate in solvent. A solvent-saturated paper towel was placed over the STM head and the STM was covered while passing solvent-saturated nitrogen into the chamber to minimize solvent evaporation.

Differential pulse voltammetry measurements were made with a PARC 273a. A 3mm gold working electrode, platinum wire counter electrode and Ag/AgCl reference electrode were used. Various mixtures of acetonitrile and toluene (as received from Aldrich) were used as solvent, all with 0.1 M tetrabutylammonium hexafluorophosphate (Fisher) as electrolyte. Scan rate of 10 mV/s, step height of 5 mV, pulse height of 50 mV and pulse width of 50 mV were used.

Triphenylphosphine-capped gold nanoparticles were prepared in a two-step process. First, a gold-triphenylphosphine complex was formed, then this precursor along with excess triphenylphosphine was exposed to reducing agent to form nanoparticles. The precursor was formed by dissolving 0.787g of triphenylphosphine in 25mL of ethanol and adding this to 25mL of 1 wt% aqueous solution of tetrachloroaurate (3:1 molar ratio of P(Ph)_3 to HAuCl_4) under vigorous stirring. The solution immediately lost its yellow color and a white precipitate formed. The mixture was allowed to stir for twenty-four hours. The solvent was then removed through rotary evaporation leaving a white product. Particles were formed from his product by dissolving 0.102g of the crude product in 50 mL of ethanol along with 0.790g of triphenylphosphine. Freshly prepared aqueous sodium borohydride (8.7mg NaBH_4 in 25 mL of H_2O) was added to this solution slowly over three minutes under vigorous stirring. The solution gradually changed color

from clear, to yellow, to amber and then a dark brown. This solution stirred overnight and eventually obtained an orange color with white precipitate. Solvent was removed via rotary evaporation and the crude product suspended in 15mL of ethanol and placed in the refrigerator overnight. The ethanol was decanted carefully, leaving behind gold nanoparticles with diameter of 1.4nm as a rust-colored solid. These could be suspended in various organic solvents (e.g. benzene, toluene and DCM).

5.3 Results

Using an uncoated STM tip, we were able to image 5nm citrate capped particles attached to a gold substrate under dodecane solution and obtain $I(V)$ curves with a similar response to those seen in air. An analysis of seventeen curves showed an average step width of 604 ± 40 mV for this system (bias = 500 mV, setpoint = 1 nA). Upon switching the solvent from dodecane ($\epsilon = 2.00$) to chloroform ($\epsilon = 4.81$), (Fig. 1) the average step-width decreased (538 ± 74 mV for 27 curves) while the variation in step width from curve to curve increased. Twenty-two curves taken in dodecane with a 900 mV bias and 1 nA setpoint gave a step width average of 605 ± 40 mV.

Octanethiol-capped particles in dodecane produced similar $I(V)$ curves to the citrate-capped particles of the same size in dodecane (fig. 2), with twenty-seven curves giving an average step-width of 619 ± 32 mV (bias = 500 mV, setpoint = 1 nA). Current-voltage curves in chloroform gave the same step width (620 ± 42 mV, 24 curves).

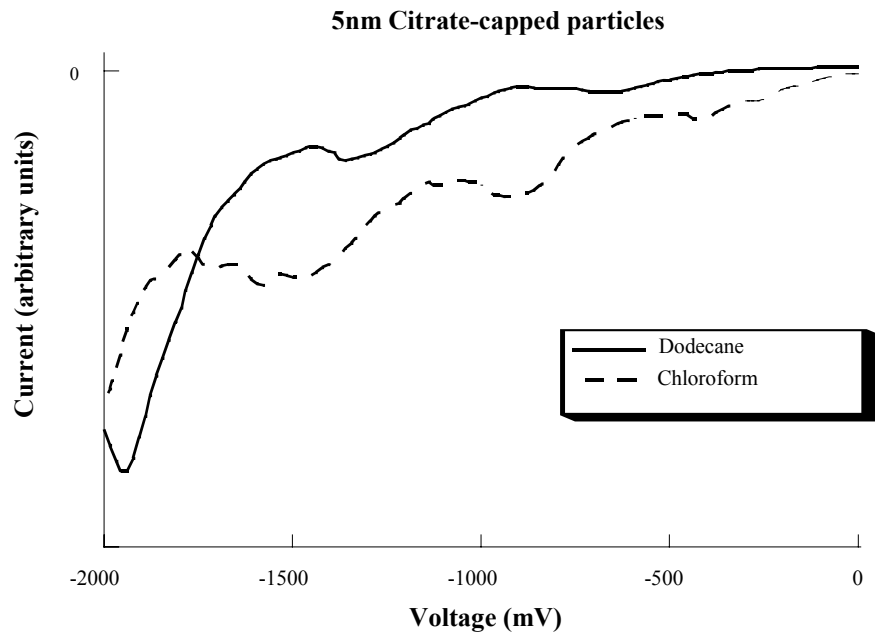


Figure 5.1 Representative I(V) curves of individual 5nm citrate-capped particles obtained under dodecane and chloroform. The voltage step width is narrower in chloroform than in dodecane.

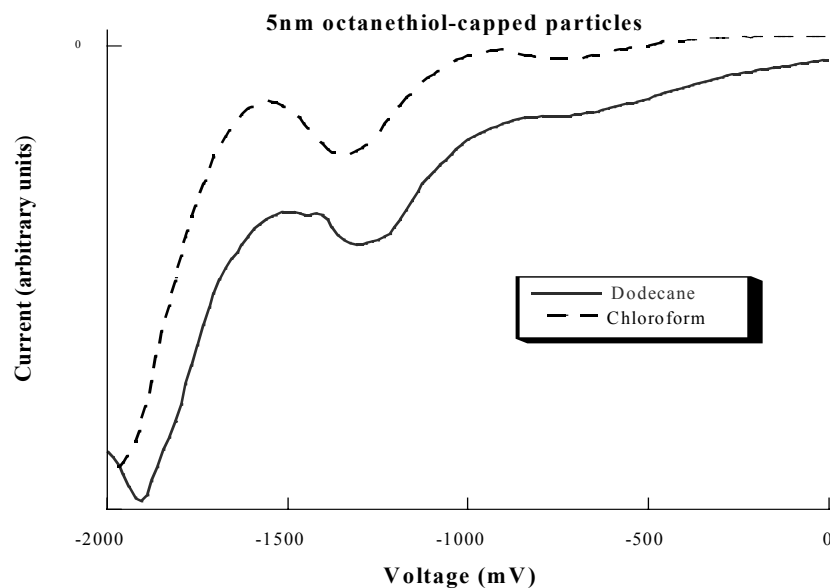


Figure 5.2 Representative I(V) curves of individual 5nm octanethiol-capped particles obtained under dodecane and chloroform.

In order to examine single electron charging phenomenon in higher dielectric solvents, solutions of size-monodisperse triphenylphosphine-coated and octanethiol-coated particles were examined electrochemically. Differential pulse voltammetry results for 1.4 nm triphenylphosphine-coated particles in various toluene/acetonitrile solvent systems are shown in Figure 3. The voltage spacing of charging peaks are 508mV, 440mV, 418mV and 230mV for 2:1, 1:1, 1:2 and 1:3 ratios of toluene:acetonitrile respectively (increasing solvent dielectric). DPV of octanethiol-coated particles gave 260mV and 238mV separation between charging peaks for 4:1 and 2:1 toluene:acetonitrile solutions.

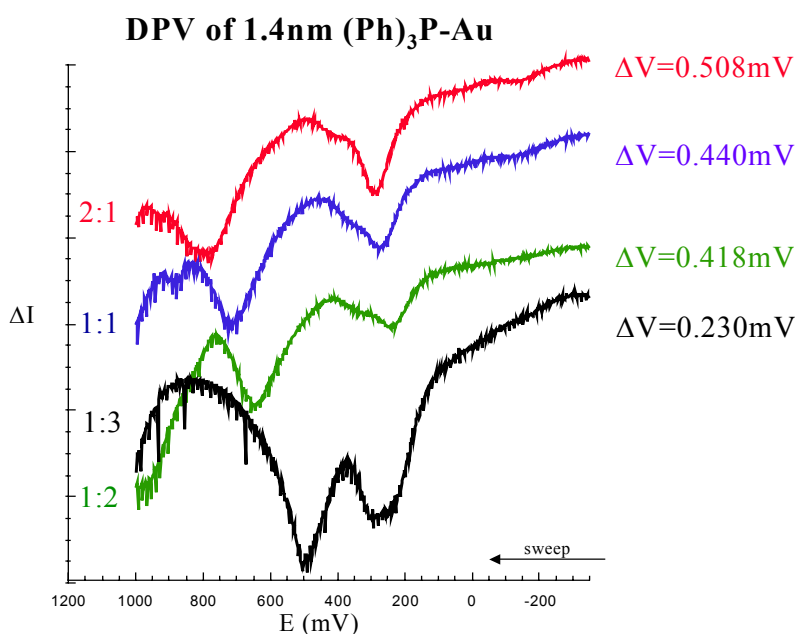


Figure 5.3 Differential Pulse Voltammograms of 1.4nm triphenylphosphine-capped particles in toluene/acetonitrile solutions ranging from 2:1 to 1:2 respectively. As the amount of acetonitrile increases, the charging energy decreases.

5.4 Discussion

Equation 4.1 describes how the dielectric constant of the material separating a metallic sphere from a metallic plate should affect the capacitance of that junction. An increase in the dielectric constant of the material between the plate and sphere will result in an increase in the junction capacitance. The solution voltammetry of triphenylphosphine-coated particles show an increase in particle capacitance with an increase in solvent dielectric. The capacitance of octanethiol-coated particles on the other hand does not show a solvent dependence (Table 5.1).

Table 5.1 Particle double-layer capacitance is tabulated as a function of both particle capping-ligand and solvent composition. Triphenylphosphine-capped particles were 1.4nm in diameter while octanethiol-capped particles were 1.6nm.

Capping-Ligand	Toluene:Acetonitrile	Capacitance (aF)
Triphenylphosphine	2:1	.315
	1:1	.364
	1:2	.383
	1:3	.697
Octanethiol	4:1	.616
	3:1	.682
	2:1	.673

An interpretation of this result is that the triphenylphosphine capping layer is disordered and allows solvent penetration very close to the particle surface while octanethiol capping ligands form a tightly ordered monolayer and provide a stable

dielectric around the particle independent of solvent composition (Figure 5.4). This suggests that the capacitance of a nanoparticle is dictated only by the dielectric constant of the material very close to its surface (e.g. the first molecular layer).

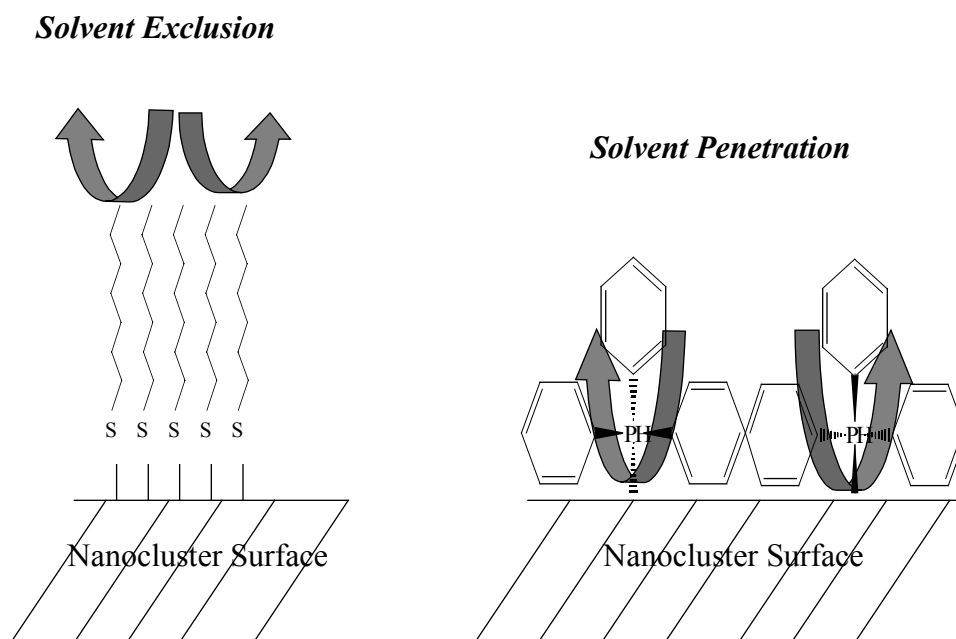


Figure 5.4 A tightly packed monolayer such as that produced by the octanethiol molecule shown on the left, will not allow solvent to penetrate close to the particle surface, whereas a sterically bulky capping-ligand such as triphenylphosphine shown at right will allow for solvent molecules to reach the particle surface.

Measurements of the $I(V)$ response of individual particles show a similar trend (Table 5.2). For a non-ordered capping layer (citrate) the tunnel-junction capacitance is dependent on solvent dielectric while the junction capacitance for an octanethiol-capped particle is independent of solvent dielectric.

Table 5.2 The capacitance of the particle/substrate junction calculated from the voltage step width of I(V) curves taken over individual particles is tabulated with respect to particle capping ligand and solvent.

Capping Ligand	Solvent	Capacitance (aF)
Citrate	Dodecane	0.265 +/- .016
	Chloroform	0.298 +/- .036
Octanethiol	Dodecane	0.258 +/- .013
	Chloroform	0.258 +/- .016

It is important to note that the step widths measured in dodecane for citrate-capped particles at different bias voltages were the same. An increase in imaging bias will cause an increase in tip height (equation 3.2) which will alter the average tip-particle separation for the I(V) curves examined. This is important for two reasons. First, the data collected in chloroform were compared to data collected under dodecane with the same feedback conditions. Because the resistance associated with chloroform is less than that of dodecane, the STM tip will be closer to the surface in a dodecane solution than under a chloroform solution under the same bias and setpoint settings³. The fact that the step-width did not change with a change in applied bias allows the two data sets to be compared. It has been previously reported that the voltage step-width doesn't change with changes in tip-height^{1h, 6}.

5.4 Conclusions

We have observed for the first time single-electron tunneling in a solution environment. The chemical nature of the solution was shown to have a marked effect on the single electron tunneling and single electron charging properties of gold nanoparticles, but only for particles coated with disordered capping ligands. Tailoring the structure of the molecular capping-layer on the particle surface can control the sensitivity of the single electron tunneling/charging properties of particles to changes in their local chemical environment. This could be of importance in designing SET circuits that will provide stable response even in chemically diverse environments. The ability to construct a nanoparticle whose capacitance varies with changes in its local chemical environment also suggests possibilities for new particle-based chemical sensing schemes and chemical gating mechanisms for single electron tunneling devices.

5.6 Chapter Five References

1. a) D. L. Klein, P. L. McEuen, J. E. Bowen-Katari, R. Roth, A. P. Alivisatos, *Appl. Phys. Lett.*, 1996, **68**, 2574. b) T. Sato, H. Ahmed, D. Brown and B. F. G. Johnson, *J. Appl. Phys.*, 1997, **82**, 696. c) E. Hartmann, P. Marquardt, J. Ditterich, P. Radojkovic and H. Steiberger, *App. Surf. Sci.*, 1996, **107**, 197 d) J. G. A. Dubois, E. N. G. Verheijen, J. W. Gerritsen and H. van Kempen, *Phys. Rev. B*, 1993, **48**, 11260. e) L. E. Harrell, T. P. Bigioni, W. G. Cullen, R. L. Whetten and P. N. First, *J. Vac. Sci. Technol. B* 1999, **17**, 2411. f) A. E. Hanna and M. Tinkham, *Phys. Rev. B.*, 1991, **44**, 5919. g) Barner, J. B. and Ruggiero, S. T., *Phys. Rev. Lett.*, 1987, **59**, 807. h) R. Wilkins, E. Ben-Jacob and R. C. Jaklevic, *Phys. Rev. Lett.*, 1989, **63**, 801. i) R. Wilkins, M. Amman, E. Ben-Jacob and R. C. Jaklevic, *Phys. Rev. B.*, 1990, **42**, 8698. j) P. J. M. van Benthum, R. T. M. Smokers and H. van Kempen, *Phys. Rev. Lett.*, 1988, **60**, 2543. k) T. A. Fulton and G. J. Dolan, *Phys. Rev. Lett.*, 1987, **59**, 109. l) K. Mullen, E. Ben-Jacob, R. C. Jaklevic and Z. Schuss, *Phys. Rev. B*, 1988, **37**, 98.
2. a) M. G. Ancona, *J. Appl. Phys.*, 1996, 79, 526. b) D. L. Feldheim, C. D. Keating, *Chem. Soc. Rev.*, 1998, **27**, 1.
3. W. Schmickler and D. Henderson, *J. Electroanal. Chem.*, 1990, **290**, 283.
4. R. W. Murray, et al, *J. Am. Chem. Soc.*, 1996, **118**, 4212.
5. D. L. Feldheim, K. C. Grabar, M. J. Natan and T. E. Mallouk, *J. Am. Chem. Soc.*, 1996, **118**, 7640.
6. R. P. Andres, T. Bein, M. Dorogi, S. Feng, J. I. Henderson, C. P. Kubiak, W. Mahoney, R. G. Osifchin and R. Refenberger, *Science*, 1996, **272**, 1323.

Chapter 6

A tailored response in the single electron tunneling properties of individual gold nanoparticles to changes in buffer solution pH

6.1 Introduction

The expected change in $I(V)$ response observed with respect to both particle size and surrounding dielectric (Tables 4.1 and 5.1) support the hypothesis that we are monitoring single electron tunneling through individual particles and that the response can be strongly affected by changes in the surface chemistry of the particle. We wanted to build on this concept by tailoring the particle surface chemistry in such a way as to cause the single electron tunneling response of the particle to selectively change in response to a specific change in its local chemical environment. Our hypothesis (Figure 6.1) was that if we made a gold particle with a protecting ligand containing some sort of reactive moiety A, then selective chemical change of this group from A to B would result in a measurable change in the $I(V)$ response of that particle.

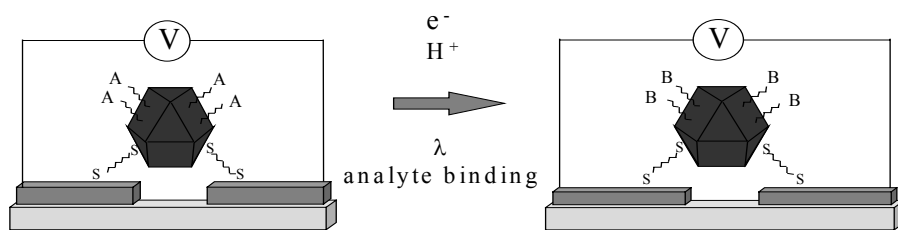


Figure 6.1 The hypothesis was that a chemical change of the particle surface chemistry, through a change in oxidation state, degree of protonation, photooxidation or some type of analyte binding will result in a change in the $I(V)$ response of the particle when connected to two electrodes in a double-tunnel junction mode.

This change could be in response to a change in the surface charge of the particle which would result in both a change in the particle capacitance, and a change in the q_o term of

Equation 2.14, acting as a gate to shift the position of the I(V) curve within the bias window. The reaction could also result in a change of monolayer order causing a change in the I(V) response of the particle in a similar manner as described in Chapter Four for citrate capped particles compared to octanethiol capped particles.

A first experiment to test this hypothesis was to make particles with a molecule whose degree of protonation will change as a function of solvent pH. This chapter describes the I(V) response of 1,6-mercaptohexamine coated particles, galvinol coated particles and octanethiol coated particles in aqueous buffer solutions ranging from pH 5 to pH 12. The amine terminated molecule is neutral at high pH and becomes a protonated cation as the pH drops through its pKa of $\sim 10^1$. Galvinol on the other hand is a neutral molecule at low pH and deprotonates to form the anion as the pH is increased through its pKa $\sim 11^2$. Octanethiol was used as a control as it remains charge neutral in solutions of all pH values (Figure 6.2).

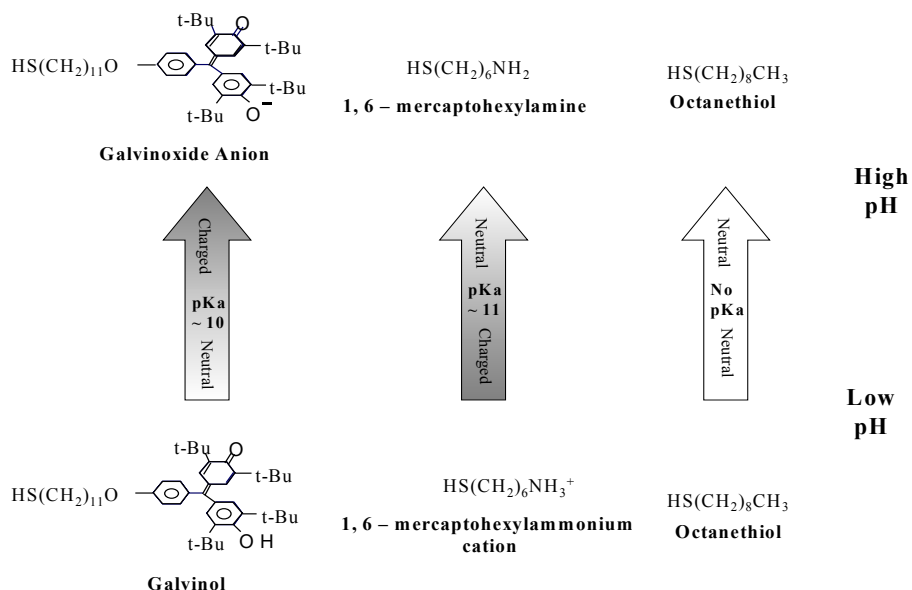


Figure 6.2 The chemical transformations of the three molecules studied in this chapter in response to changes in solvent pH are diagramed. It is important to note which molecules are charged at both high and low pH solutions.

6.2 Experimental

Octanethiol particles were synthesized via the Brust prep³. Substrates containing these particles were prepared by first modifying a gold slide with an octanethiol SAM as described in Chapter 4 and then incubating the slide in the octanethiol-capped particle solution for ~4 hours. Galvinol capped particles were synthesized via a modified Brust prep where galvinol was used in place of octanethiol to stabilize the particle surface. Substrates containing these particles were prepared using a clean gold slide modified with an octanethiol SAM and then incubating it in the galvinol-capped particle solution for ~4 hours. Substrates with amine coated particles were prepared as described in Chapter 4 where 5nm citrate-capped particles were first attached to a dithiol modified gold slide and then the substrate soaked in a ~10 mM solution of 1, 6-mercaptohexylamine for a few hours. Potassium phosphate buffer solutions were prepared making sure to keep ionic strength the same at all pHs.

Insulated STM tips were prepared by coating cut Pt/Ir tips with hot melt glue. To expose the apex, the tip was mounted upside down in a tip holder and a hot soldering iron was held near the end of the tip, heating the glue and causing it to flow down the tip. Heat was removed when there appeared to be only a very thin layer of glue at the apex of the tip. There is a narrow range of optimal thickness that is difficult to achieve where the insulating layer is thin enough to allow the STM tip to operate properly, yet thick enough to minimize leakage current.

The solution STM experiments were performed as described in Chapter 5. The pH of the buffer solution in the fluid cell was tested with pH paper after a data set was collected and compared to the pH of the stock solution to ensure that the pH had not changed during the experiment.

6.3 Results

The $I(V)$ curves measured over amine-coated particles in aqueous solution show well-defined coulomb staircase response at all pH values examined (Figure 6.3). At pH 12 with the amine group in its neutral state, a voltage step width of 296 ± 25 mV is observed. As the pH is lowered and the amine is protonated, the step width decreased from 276 ± 5 mV at pH 8, to 229 ± 24 at pH 5. The position of the coulomb staircase along the voltage axis is irreproducible for a given pH. This irreproducibility of staircase position is true of all coulomb-staircase data described in this dissertation.

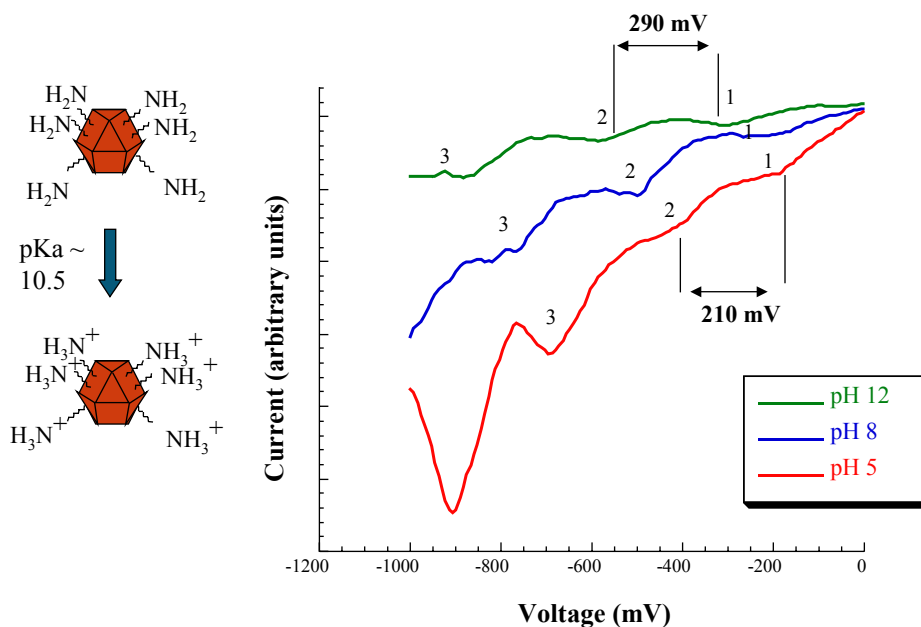


Figure 6.2 I(V) curves collected over amine-capped particles in buffer solutions of pH 5, 8 and 12. The step width decreases as the pH decreases.

Galvinol-capped gold particles also result in coulomb staircase response in the I(V) measurements (Figure 6.4). However, curves from these particles have an opposite response to pH from the amine-capped particles, showing a decrease in step width with *increase* in solution pH ($x \pm y$ mV at pH5, $a \pm b$ mV at pH 8 and $c \pm d$ at pH 12). Octanethiol modified particles showed no difference in step width between pH 5 and pH 12 (Figure 6.5). Junction capacitance is tabulated as a function of capping ligand, particle size and solution pH in Table 6.1.

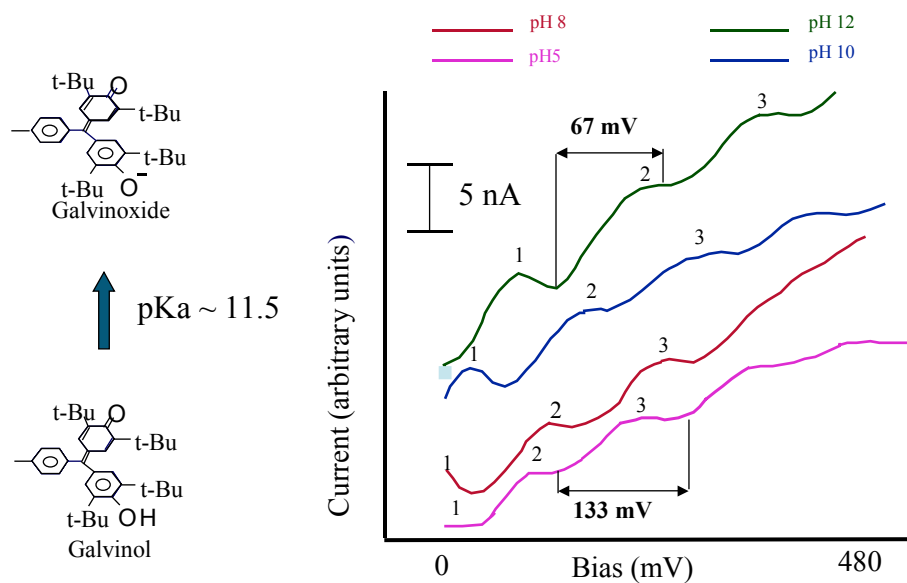


Figure 6.4 Current-voltage curves collected over individual galvinol-capped particles in buffer solutions of pH 5, 8, 10 and 12. The voltage step width decreases in higher pH solutions.

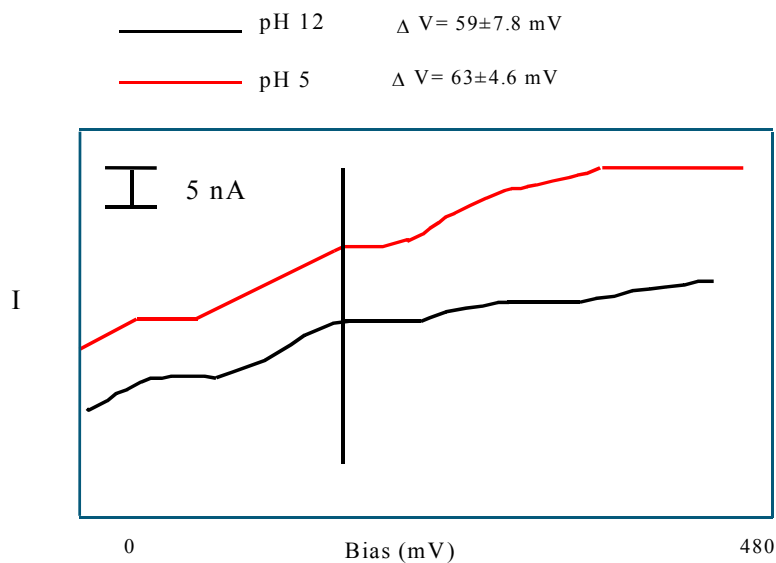


Figure 6.5 Current-voltage curves collected over individual octanethiol capped particles in buffer solutions of pH 5 and 12. No differences in the step width are seen at these two extreme pH values.

Table 6.1 Particle-substrate junction capacitance is tabulated as a function of capping ligand, particle size and solution pH.

Nanoparticle	Medium	Diameter (nm)	C(aF)
Gal-Au	H ₂ O (pH 5)	8	1.2±0.12
	H ₂ O (pH 8)		1.8±0.14
	H ₂ O (pH 12)		2.4±0.20
Amino-Au	H ₂ O (pH 5)	5	0.70±0.08
	H ₂ O (pH 8)		0.58±0.011
	H ₂ O (pH 12)		0.54±0.05
C ₈ -Au	H ₂ O (pH 5)	5	2.7±0.30
	H ₂ O (pH 12)		2.5±0.10

6.4 Discussion

The significance of these data is most clearly seen in Figure 6.6 where step width is plotted as a function of solution pH for both the amine and galvinol coated particles. The amine-coated particles show their lowest charging energy at low pH and galvinol particles show theirs at high pH, but *both* particles show their lowest charging energy when they exist in their charged state.

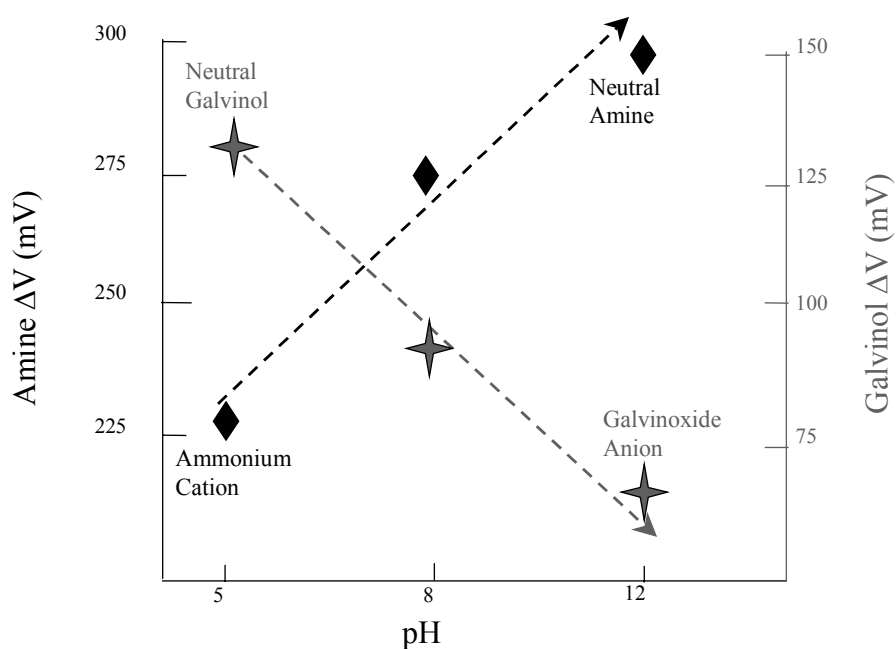


Figure 6.6 Voltage step-width is plotted as a function of pH for both amine and galvinol-capped particles. It is important to note that both molecules have their narrowest step width in their charged states. The dotted lines are not meant to suggest that the changes in step-widths are linear with pH. They are simply present to show the direction of change with pH for each capping-ligand.

The octanethiol coated particles, whose surface charge does not change within the pH range examined, show no difference in charging energy with respect to change in solution pH. These data suggest that, rather than being simply a function of pH, the electronic properties of gold nanoparticles are strongly dependent on the charge of the capping monolayer. It is also clear from the three different and predictable responses to pH for the three particle systems examined that the change in $I(V)$ response is the result of specific changes in the particle monolayer, not some other solvent-related effect (i.e. slight differences in buffer ionic strength, pH dependent change in tip density of states, etc.).

An increase in capacitance with increase in monolayer charge is also observed for the double layer capacitance of bulk planar electrodes modified with organic monolayers⁴. Figure 6.7 shows the structure of a ferrocene-terminated monolayer coated electrode and the equivalent circuit for the junction capacitances that contribute to its double layer capacitance (i.e. electrode/monolayer capacitance and monolayer/solution capacitance).

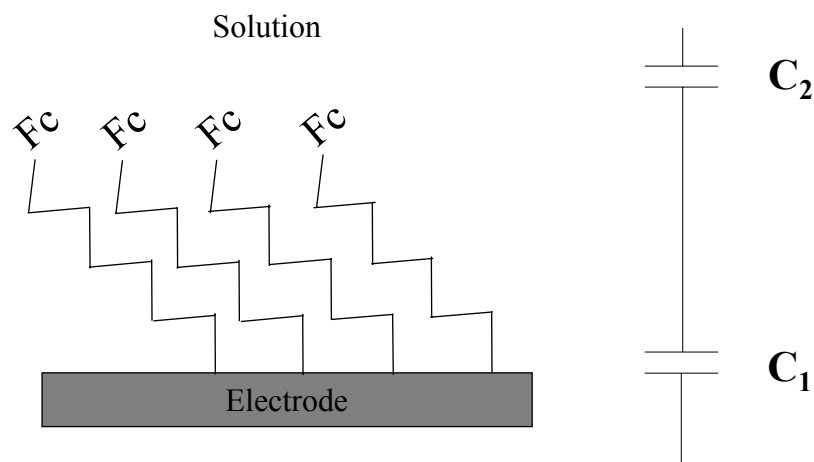


Figure 6.7 A ferrocene-terminated monolayer-coated electrode exposed to solution and the equivalent circuit associated with the double layer capacitance for this system

The observed double layer capacitance is equal to the total circuit capacitance⁵.

$$\frac{1}{C_{dl}} = \frac{1}{C_1} + \frac{1}{C_2} \quad \text{equation 6.1}$$

The monolayer/solution capacitance (C_2) is much larger than the monolayer/electrode capacitance (C_1) for these systems. This means that while a change in charge of the monolayer end-group results in a dramatic change in the solution/monolayer capacitance, C_2 , this capacitance has a negligible overall contribution to the double-layer capacitance and thus a change in monolayer charge alone will not result in a change in the electrode capacitance. The change in this double layer capacitance that results from a change in end-group charge is due to structural rearrangement in the substrate monolayer due to the presence of the charge, not simply the charge itself. This model agrees with results observed in Chapter 5, where a disordered monolayer allowed for solvent penetration to the particle surface. In the experiments with amine and galvinol-capped particles, it seems probable that the junction capacitance increased with an increase in monolayer charge due to increased disorder in the monolayer and increased penetration of water to the particle surface, whose large dielectric constant causes a decrease in charging energy.

It appears, though that the galvinol monolayer coating gold nanoparticles would be poorly packed and highly disordered even in the neutral state. These particles still show a dramatic change in capacitance when the monolayer is charged, suggesting that the eleven-carbon alkyl group attaching the galvinol group to the surface provides some sort of order in the neutral state. From this it appears that changes in charge even for bulky capping ligands such as single-stranded oligonucleotides, should result in observable changes in the $I(V)$ response of a particle, as long as the bulky ligand is tethered to the particle surface through an alkyl chain to provide a somewhat ordered foundation.

The irreproducibility of staircase-position makes it impossible to comment on the effect capping-ligand charge has on the q_o term of Equation 2.14⁶. This irreproducibility is a function of the extreme sensitivity of single electron tunneling to small changes in local charge⁷. This sensitivity means that each particle examined on a surface will have a very different q_o term, even under the same chemical conditions. Assuming that the q_o term is stable for a particular particle located on a surface over time at room temperature, the only way to determine the effect capping-ligand charge would have on q_o would be to perform I(V) measurements on the exact same particle as its surface charge is altered. This experiment would be an extreme technical challenge, and it is unclear whether q_o would be stable with time for a particular particle under any conditions outside ultra-high vacuum.

6.5 Conclusions

The results presented here show that particles can be designed to have a defined change in their I(V) response when specific changes in their local chemical environments occur. The change in response is governed by a change in junction capacitance. Importantly, it has been shown that the change in chemical environment can result in either an increase or a decrease in capacitance by designing the structural rearrangement that occurs in the particle capping monolayer upon changing the local chemical environment in a specific way. As seen previously, an octanethiol monolayer can be used to produce a particle that has a stable I(V) response in various chemical environments.

This ability to tailor the I(V) response of the particle to a very specific change in

local chemical environment suggests gold nanoparticles could be useful in new chemical sensing paradigms⁸. It is important to note that while the pH range examined in these experiments was broad, the effect on the particle surface was a change in protonation of approximately twenty molecules. This extreme sensitivity to only a few molecular events suggests that gold nanoparticles could find a niche in chemical sensing applications that require a strong response to the presence of only a few molecules such as drug discovery, proteomics and biological warfare agent detection.

6.6 Chapter Six References

1. F. Carey, "Organic Chemistry" 3rd edition, McGraw-Hill, New York, **1996** 900.
2. L.C. Brousseau, III, Q. Zhao, D. A. Shultz, and D. L. Feldheim, *J. Am. Chem. Soc.*, 1998, **120**, 7645.
3. M. Brust, M. Walker, D. Bethell, J. J. Schiffrin, R. J. Whymann, *Chem. Comm.*, 1994, 801.
4. M. D. Porter, T. B. Bright, D. L. Allara, C. E. D. Chidsey, *J. Am. Chem. Soc.*, 1997, **119**, 9279.
5. D. Halliday, R. Resnick and F. Walker, "Fundamentals of Physics Extended" 5th edition, Wiley and Sons, New York, 1997.
6. A. E. Hanna and M. Tinkham, *Phys. Rev. B.*, 1991, **44**, 5919.
7. M. J. Yoo, T. A. Fulton, H. F. Hess, R. L. Willett, L. N. Dunkleberger, R. J. Chichester, L. N. Pfeiffer and K. W. West, *Science*, 1997, **276**, 579.
8. D. L. Feldheim, C. D. Keating, *Chem. Soc. Rev.*, 1998, **27**, 1.

Chapter 7

The role of the supporting monolayer in defining single electron tunneling current magnitude for particle/monolayer/substrate structures probed with an STM.

7.1 Introduction

A major research thrust in the area of nanoelectronics has been the study of individual molecules as possible active components in electronic device designs¹. Many molecules have shown non-linear $I(V)$ response under UHV conditions which suggests that functional electronic circuits could be built from these molecules. Also of importance is the fact that molecular self-assembly is the most widely proposed mechanism for bottom-up circuit construction from individual nanostructures². Understanding the electronic properties of the molecules that will guide this assembly is critical in designing optimum circuit architectures. Studying not just the electronic properties of isolated molecules or nanostructures, but the properties of a self-assembled device where the molecules and component-materials are interacting as they would in a self-assembled circuit, is of critical importance.

Wiring-up individual molecules is an extreme challenge. While Dekker and co-workers have succeeded in placing a very large, individual, double stranded DNA molecule between two electrodes³ and measuring its $I(V)$ response, most other methods for taking measurements, such as break junctions and sandwich structures have analyzed hundreds, if not thousands of molecules. Break-junctions⁴ are unstable, transient structures, and the nature of the molecule/metal interface in these devices is poorly understood. Sandwich structures⁵ created by evaporating metal onto a monolayer coated conductive substrate require difficult and costly processing steps and often result in short-circuits. Mercury-drop experiments⁶, where a monolayer protected drop of mercury is brought into contact with a monolayer coated conductive substrate, are unstable and only useful for measurement of multilayers due to the requirement that both surfaces be coated

with a monolayer to avoid short circuit formation. These measurements are all performed on a relatively large surface with an unknown number of molecules, making it impossible to calculate relevant information for an individual molecule. When examining large surfaces of self-assembled monolayers, it is quite possible that the response of the structure is defined in large part by a few defect sites within the structure and is not representative of one or a few molecules connected between two electrodes. STM allows for the probing of individual molecules with the tip⁶, but the molecule is only physically connected to one electrode, limiting its ability to mimic proposed circuit designs.

Recently Lindsay used a conductive AFM to probe a large gold nanoparticle resting on a monolayer-coated gold substrate⁷. These measurements showed that a large particle attached to a gold substrate through an octanedithiol monolayer was significantly more conductive than a similar particle attached to the substrate through a methyl terminated octanethiol layer. These experiments assume that the AFM tip/particle contact is ohmic and that the particle is large enough to behave as a bulk electrode. Quantized variation in particle conductivities were observed, suggesting that the system was sensitive enough to measure properties at the single-molecule level. Kubiak has previously measured the coulomb staircase response of a 2.4 nm gold particle attached to a gold surface coated with an α, α' -xylyldithiol monolayer⁸. A numerical fit of the coulomb staircase data allowed him to calculate a resistance of 2.0 M Ω for the molecule connecting the particle to the surface, which was in agreement with accepted values.

Particle-based measurements show a clear advantage for probing the electronic response of molecules to the experiments described earlier. They allow one to probe a small number of molecules that are physically contacting two electrode surfaces. These

structures are stable over long periods of time, are very easy to form, and are truly self-assembled structures. Measurement of the single electron tunneling response of a particle attached to a surface through a molecular layer also allows for the separation of the capacitive and resistive contributions to the overall junction impedance in one simple measurement.

There is significant theoretical and experimental information explaining the role the structure of a molecular chain plays in defining the rate of electron transport from one end of the chain to the other. However, very little work has been aimed at understanding the effect the metal/molecule contact has on the steady state current response of a complete electrode/molecule/electrode assembly. The Lindsay experiment above shows that the end-group that attaches the molecule to a metal electrode can have a marked effect on the resistance measured for the structure. Seminario has performed theoretical calculations that suggest both the type of electrode and the molecular end-group play a significant role in defining the junction resistance due to differences in alignment of the Fermi levels of the metal and the molecule¹⁰.

This chapter describes the measurement of single electron tunneling properties of 1.4 nm triphenylphosphine coated gold nanoparticles attached to a gold substrate through two different molecules (Figure 7.1). First a hexanedithiol monolayer was applied to the gold substrate, connecting the particle to the molecule via a sulfur-gold bond. This was then compared to measurements made on particles connected to a gold-coated slide through a nitrogen-gold bond via mercaptoheptamine. The results from the Lindsay experiment suggest that a stronger chemical bond between particle and molecule should result in a less resistive structure. These experiments compare the thiol/gold linkage to

an amine/gold linkage to see if a change in single electron tunneling response of the two systems is observed.

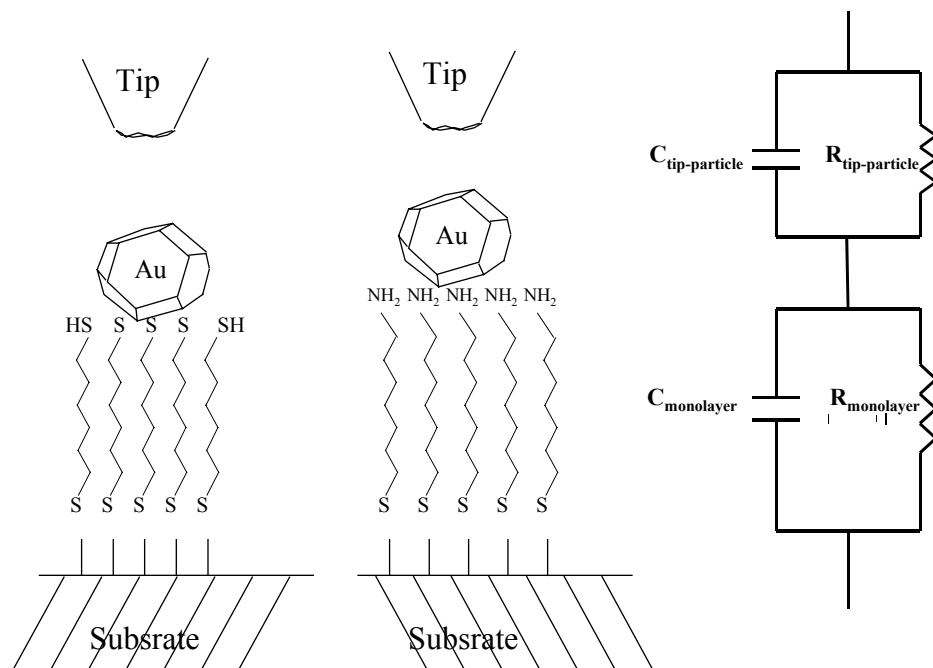


Figure 7.1 Diagram of the experiment performed. 1.4 nm gold particles were attached to a gold substrate through either a 1,6-hexanedithiol or a 1,7-mercaptoheptamine monolayer. The structure results in a double tunnel junction due to the tip-particle junction and the monolayer junction connecting the particle to the substrate.

7.2 Experimental

Triphenylphosphine-capped gold particles were synthesized as described in Chapter 5. Gold substrates were cleaned and modified as described in Chapter 4 with either 1,6-hexanedithiol or 1,7-mercaptoheptamine. These substrates were then incubated in solutions of triphenylphosphine-capped particles for ~4 hours. Current-voltage curves were taken with a DI Nanoscope IIIa in CITS mode with bias = 1 V and various setpoint currents.

7.3 Results

Coulomb staircase response was observed for triphenylphosphine-capped particles attached to gold substrates by both 1,6-hexanedithiol and 1,7-mercaptoheptamine. Figure 7.2 shows representative curves obtained for each supporting monolayer. Thirty-eight curves taken over particles supported on a 1,6-hexanedithiol monolayer with a bias voltage of 1 V and a setpoint current of 500 pA were analyzed and resulted in an average step width of 689 ± 83 mV and an average step height of 10.50 ± 8.72 nA. These data, and all others described here are for the second current step in the negative bias direction from zero (see Figure 7.2). The “step-height” refers to the total current gained in one cycle of the I(V) curve (i.e. on average, over

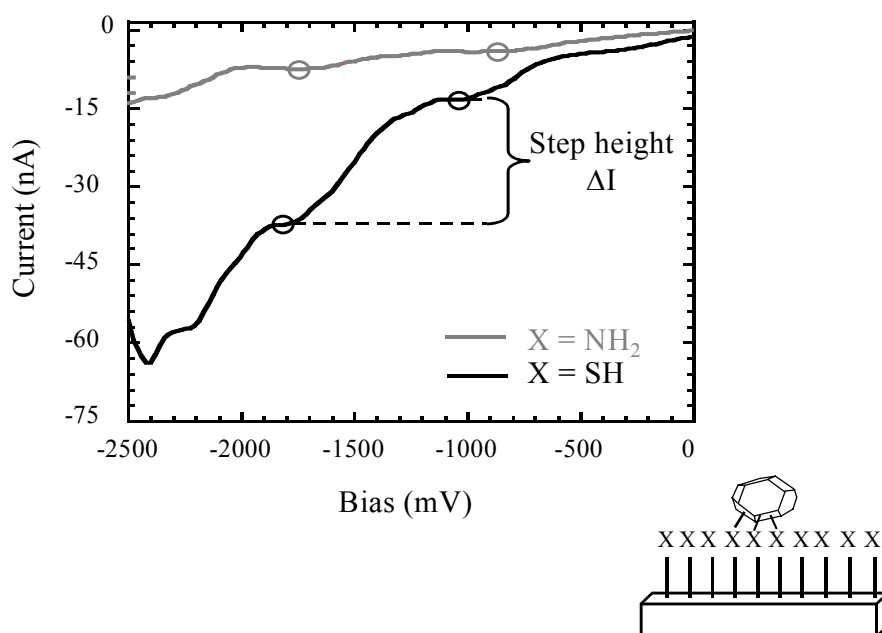


Figure 7.2 Representative current-voltage curves of 1.4 nm triphenylphosphine capped gold particles attached to a gold substrate with 1,7-mercaptoheptamine(—) and 1,6-hexanedithiol (—). The second step in the negative bias direction was used for current measurements. The step height was considered to be the full current gain within one complete cycle (see circles on curves). Note the larger step height for the dithiol supporting monolayer.

a voltage span of 689 mV). Particles supported by a 1,7-mercaptoheptamine monolayer were examined with a 1 V bias and setpoint currents of 500, 1000, and 5000 pA. Data for all experiments are shown in Table 7.1. Figure 7.3 presents this data in histogram form. Step width did not vary within these measurements.

Table 7.1 Current change for the second step in the negative bias direction are shown for several data sets. 1,7-mercaptoheptamine was studied with various STM setpoint currents. All curves were collected with 1V imaging bias.

Monolayer	Setpoint	Avg. Step height (nA)	# of curves
1,7-mercaptoheptamine	5000	4.08 ± 1.98	48
1,7-mercaptoheptamine	1000	2.55 ± 1.71	77
1,7-mercaptoheptamine	500	2.07 ± 1.02	20
1,6-hexanedithiol	500	10.50 ± 8.72	37

7.4 Discussion

The voltage step widths observed here are broader than those for the 5 nm citrate-capped particles discussed in earlier chapters. This is consistent with the smaller size of these triphenylphosphine-capped particles. The greater distribution in the voltage step widths suggests that there is a greater dispersity in the particle diameter for these

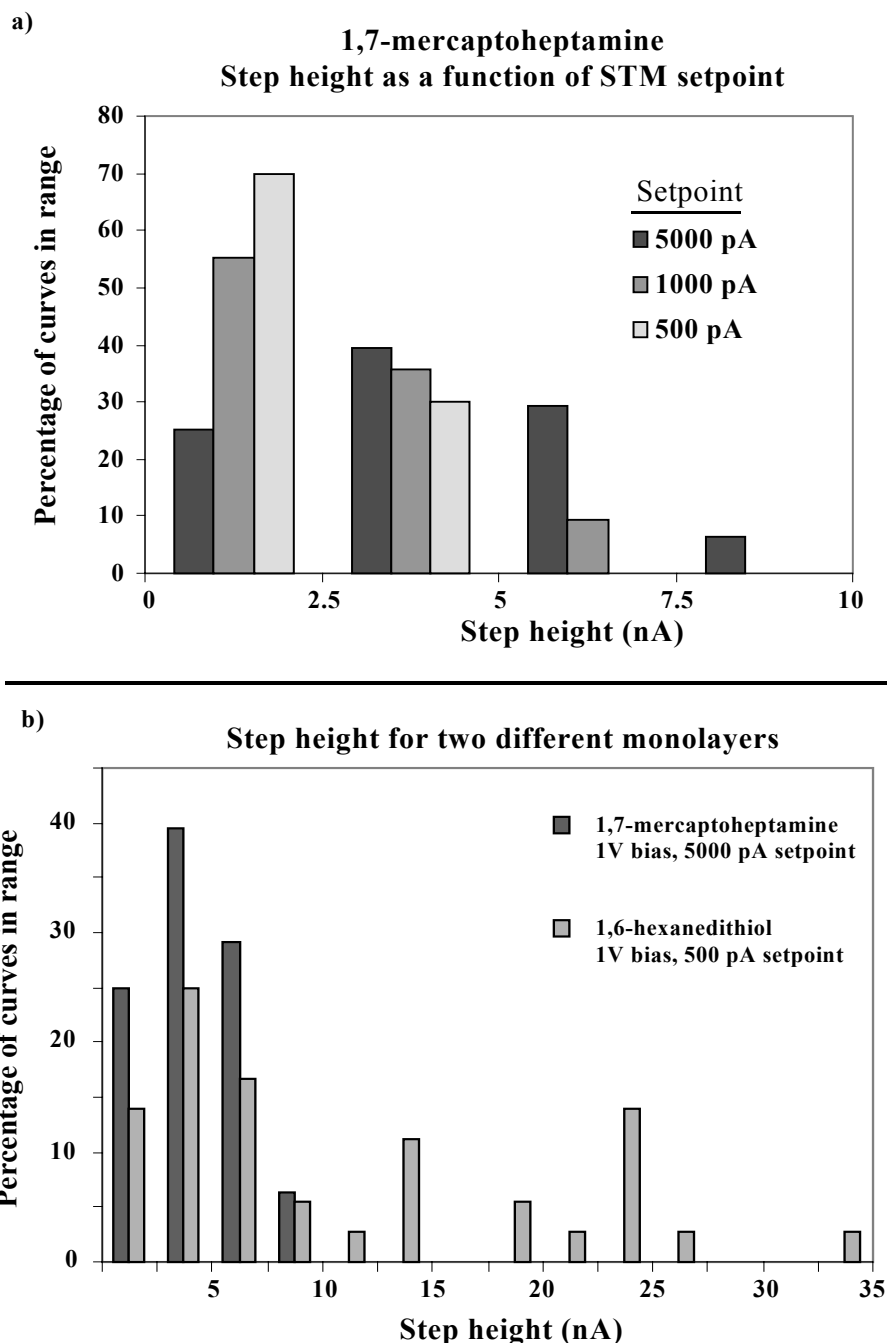


Figure 7.3 a) Step height represented in histogram form for particles supported on a 1,7-mercaptoheptamine monolayer with various imaging setpoint currents. A lower setpoint should result in a larger average tip-particle separation and a larger junction resistance. The change in step height with change in particle-tip junction resistance suggests that this is the more resistive junction. b) step height collected for particles resting on a 1,7-mercaptoheptamine monolayer and particles on a 1,6-hexanedithiol monolayer. The STM conditions were chosen such that the tip-particle separation should be greater for the dithiol data, yet on average, the current response is still stronger for these data (larger percentage of curves at high step height).

samples. This increase in variance could also be due to greater variation in the particle/substrate junction.

The current height of each step is related to the larger of the two tunnel junction resistances, $R_{\text{tip-particle}}$ and $R_{\text{monolayer}}$ (Figure 7.1) as described in Section 2.2.1. Curves were collected over particles attached to a 1,7-mercaptoheptamine monolayer at various setpoint currents (e.g. different tip-substrate separations. See Section 3.1). As the setpoint increases, the STM tip scans the surface with a smaller tip-substrate separation. As the tip-substrate separation decreases, the tip-particle resistance decreases and, if the tip-particle resistance is the defining junction for current flow, the current height in the $I(V)$ curves will increase. This trend is observed in these data, as the histograms of Figure 7.3a show, thus $R_{\text{tip-particle}}$ is the defining junction and which suggests that the step height can reveal relative information about the magnitude of $R_{\text{tip-particle}}$.

The distribution of these current heights is fairly broad. This is more than likely due to the experimental method used for collecting the current-voltage curves. While at a given setpoint the tip-substrate spacing will be consistent, the same can not be said for the tip-particle separation, because the user has no control over where the $I(V)$ curves are collected with respect to the particle in CITS mode (Figure 7.4). Thus, one $I(V)$ curve resulting in a coulomb staircase may be taken with the tip directly over a particle while another may be taken when the tip is off to the side of a particle. While this limitation precludes any quantitative statements to be made regarding the relative junction resistances, the histograms of Figure 7.3a striking differences that allow qualitative statements to be made.

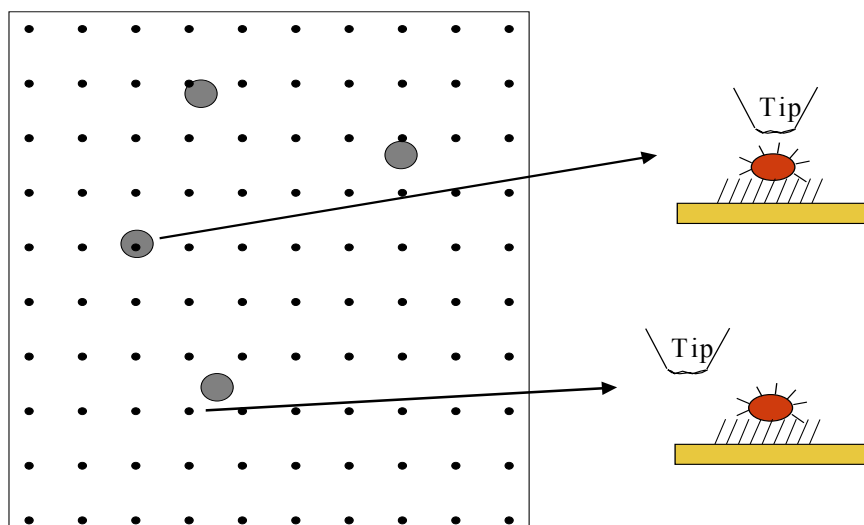


Figure 7.4 Cartoon representation of CITS data collection mode. An image is shown on the left containing four nanoparticles. The 10x10 matrix shows positions in that image where I(V) curves were collected. On the right, it can be seen that while tip-substrate separation may be constant for the entire image, if the lateral tip-particle spacing differs for two measurements, the tip-particle separation will also differ. Therefore, a given data set with a particular bias and setpoint will still produce a distribution of tip-particle barrier widths for I(V) measurements.

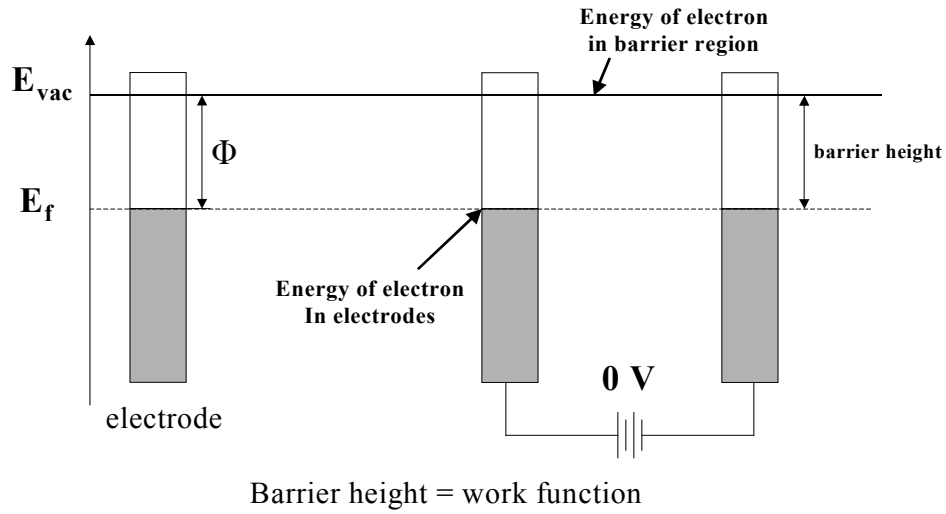
Figure 7.3b shows step-height histograms for particles connected to a gold substrate via hexanedithiol (bias = 1V, setpoint = 500 pA) compared to a histogram for particles resting on a 1, 7-mercaptoheptamine monolayer (bias = 1V, setpoint = 5nA). The differences are striking. Measurements made over a dithiol surface, on average, show a much larger current response. As Section 2.2.1 outlines, the data in Figure 7.3 suggests that this difference in current response between the dithiol monolayer and the mercapto-amine monolayer should be due to a change in the tip-particle resistance, not the particle substrate resistance. It appears from the data that the tip-particle junction over the dithiol monolayer is less resistive than the tip-particle junction for the mercaptoamine monolayer. This is in spite of the fact that experimental condition were

chosen such to provide, on average, greater tip-particle separation for the dithiol experiment: a lower setpoint was used which should provide greater tip-substrate separation. This is a very interesting result, as it suggests that not only does the nature of the molecule/particle interface have an affect on the rate of tunneling through the molecule, but it also affects the rate of tunneling onto the particle through space from other electrodes as well. To understand this, one must look at what can affect the rate of tunneling through a barrier.

As described in Chapter 3, the rate of tunneling between two electrodes is strongly affected by the distance separating those two electrodes. This is known as the tunneling barrier width. As just described, the barrier width (tip-particle separation) for the measurements over the dithiol surface should actually be larger than for the mercapto-amine surface. This would suggest a weaker current response from this system, not larger.

The rate of tunneling is also affected by the barrier height (Figure 7.5a). The barrier height refers to the difference in energy of an electron in the barrier region compared to the energy of an electron in the electrode region of the system¹⁰. This height is determined by the average of the work functions (Φ) of the two electrodes. The work function of an electrode describes the energy required to remove an electron from the electrode into vacuum. Figure 7.5b shows how changing the work function of one of the electrodes can change the barrier height of a tunnel junction consisting of two electrodes separated by vacuum. If the work function of the second electrode is lowered, then when

a) Barrier height of two electrodes with the same work function.



b) Barrier height for electrodes with different work functions.

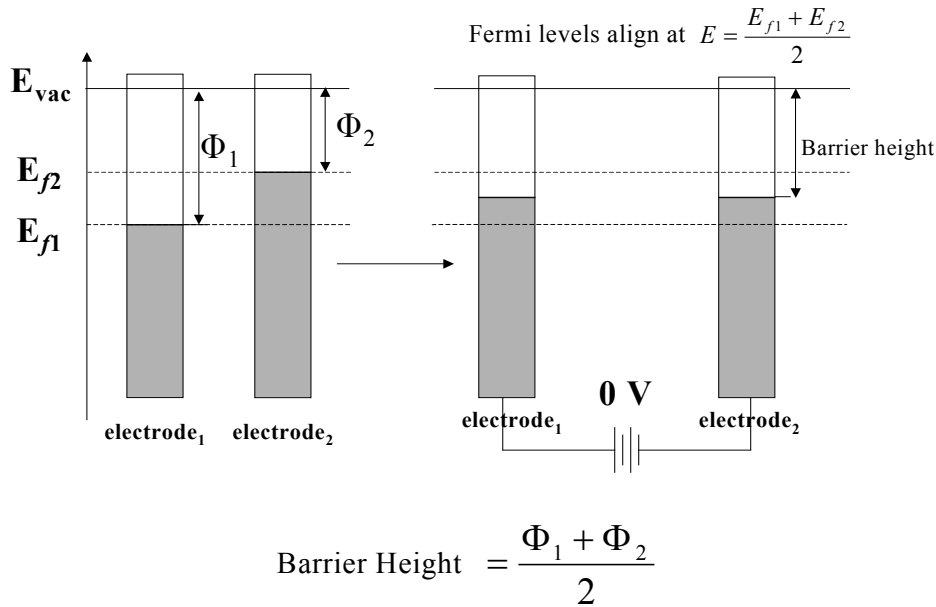


Figure 7.5 a) The work function of an electrode is the amount of energy required to remove an electron from its Fermi level into vacuum. For a tunnel junction made from two electrodes with the same work function separated by vacuum, the tunnel barrier height is simply their work function, as this describes the difference between the energy of an electron in the electrode and the energy of an electron in the barrier region. b) For electrodes differing in work function, their Fermi levels will align at an energy halfway between the original Fermi levels, E_{f1} and E_{f2} . If the tunnel barrier is again vacuum, then the height to tunneling will now be the average of the two work functions.

the electrodes are connected and their Fermi levels align, the energy of the electrons in the electrodes will be closer to that of an electron in vacuum. A lower barrier height results in a much less resistive tunnel junction.

The work function of the nanoparticle could easily be affected by molecular adsorption to its surface, as this is seen in bulk metal electrodes¹⁰. As figure 7.5b shows, a change in the Fermi level of the particle will result in alteration of the particle's work function. The nitrogen atom of the amine linkage is more electronegative than the sulfur atom of the thiol linkage. This larger electronegativity should result in a greater electron withdrawing power of the amine terminated molecule and an increase in the particles work function compared to a particle with a surface monolayer formed with a less electronegative functional group. This is a possible mechanism for explaining the increased current step-height observed for particles connected to a gold slide through a hexanedithiol monolayer compared to particles connected through a 1,7-mercaptoheptamine monolayer.

The distribution in current step-heights appears much broader for the dithiol monolayer, but this is a result of the bin-width compared to the maximum current. If the mercaptoamine data were plotted using a bin size that was proportional to its maximum current value, the distribution would appear equally broad.

To determine this tunnel junction quantitatively and to learn anything about the resistance of the particle-substrate junction, a model for single electron tunneling must be numerically fit to the experimental data. The current model used for single electron tunneling is the semi-classical theory described in Chapter 2. Figure 7.6 shows an attempt to fit the semi-classical theory to a typical current-voltage curve. While this fit is

Semi-Classical Theory Compared to Experimental Data

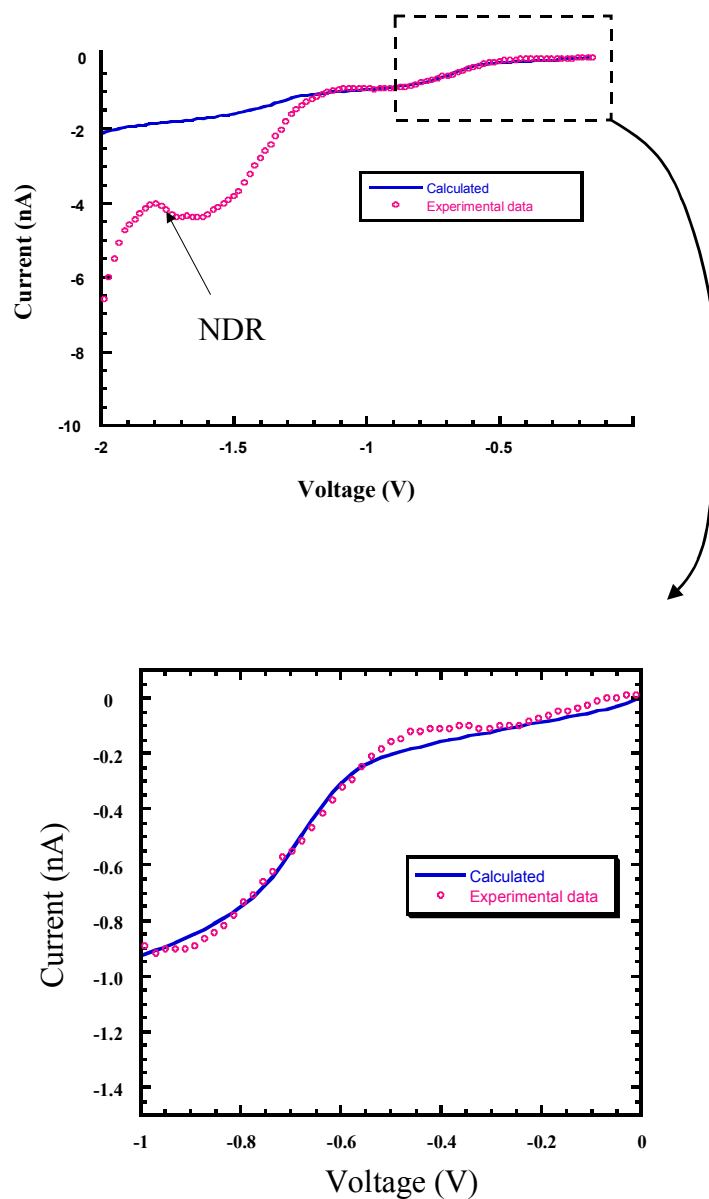


Figure 7.6 A typical I(V) curve collected over a particle resting on a 1,6-hexanedithiol monolayer is shown (o). The solid line is a curve calculated using the Igor routine presented in the Appendix. Note the increase in step-height at larger voltages and the NDR peak in the experimental data that is not accounted for in the semi-classical model. As shown in the lower zoom-in, the semi-classical model can accurately fit data over a smaller voltage window.

accurate at lower biases (see zoom-in in the bottom of the Figure), it is impossible to fit the semi-classical model across the complete voltage window examined. The two features that aren't accounted for in the semi-classical theory are 1) the step-height of the data presented here usually increases with increasing applied bias and 2) negative differential resistance (NDR), where current decreases upon increasing applied bias, is often seen in the plateau region of the data presented in this dissertation.

A number of explanations exist for the increase in step-height upon increasing bias. First, the semi-classical model doesn't consider any other possible tunneling pathways or mechanisms. An exponential co-tunneling pathway could result in an increase in step-height with increasing applied bias. Also, particle motion during the experiment could result in a change in junction resistance during the time frame of the experiment. Charging of the particle could conceivably lead to it being attracted to the oppositely charged electrode. At the higher end of the bias window examined here, monolayer decomposition and thermionic emission are quite possible. Unfortunately, to examine single electron tunneling at room temperature, wide step-widths and large applied biases are required.

The NDR observed in the plateau region could be a result of either empty localized states in the substrate acting as charge traps or a local density of states existing in one of the two electrodes. Others have observed charge trapping significant enough to lead to NDR. It is also highly likely that the STM tip used in these experiments has a local density of states. Similar tips have been used in our group to measure NDR in molecules⁶ and a requirement of those measurements is that a local density of states exists in the tip. Attempts are being made to modify the semi-classical theory to account

for these anomalies and to determine if fitting just the lower voltage region can provide meaningful insight into the data.

7.5 Conclusions

The data presented in this chapter show conclusively that there is a change in current response with tip height for a given particle/monolayer system. It was also shown that a gold particle attached to a substrate through a 1,6-hexanedithiol monolayer has a high probability of producing a stronger current response than a particle attached to a substrate with a 1,7-mercaptoheptamine monolayer. A possible mechanism for this change in response is the higher electronegativity of nitrogen compared to sulfur. A new STM controller is currently being installed in our laboratory that will allow for more precise control over the tip-particle separation. This should provide more consistent data and also allow us to perform accurate current vs. tip-height measurements. These measurements will allow for accurate separation of the contribution of barrier height and barrier width to the total junction resistance, making assignment of a mechanism for the difference in current response easier. Unfortunately, the semi-classical model of single electron tunneling can only be used for qualitative comparison of these data. The theory must be modified for numerical fitting of STM measurements at room temperature and atmospheric conditions to allow for co-tunneling events and quantum mechanical considerations. Without a model to numerically fit to the data, no comment can be made about the role of substrate monolayer in changing the particle-substrate resistance.

7.6 Chapter Seven References

1. J. M. Tour, *Acc. Chem. Res.*, 2000, **33**, 791.
2. J. L. Wilbur and G. M. Whitesides in "Nanotechnology" ed. G. Tripp, Springer-Verlag, New York, 1998, 331.
3. D. Porath, A. Bezryadin, S. de Vries and C. Dekker, *Nature*, 2000, **403**, 635.
4. M. A. Reed, C. Zhou, C. J. Muller, T. P. Burgin, J. M. Tour, *Science*, 1997, **278**, 252.
5. J. Chen, M. A. Reed, A. M. Ravlett, J. M. Tour, *Science*, 1999, **286**, 1550.
6. C. B. Gorman, R. L. Carroll, R. R. Fuieler, *Langmuir*, 2001, **17**, 6923.
7. X. D. Cui, A. Primak, X. Zarate, J. Tomfohr, O. F. Sankey, A. L. Moore, T. A. Moore, D. Gust, G. Harris, S. M. Lindsay, *Science*, 2001, **294**, 571.
8. R. P. Andres, T. Bein, M. Dorogi, S. Feng, J. I. Henderson, C. P. Kubiak, W. Mahoney, R. G. Osifchin and R. Refenberger, *Science*, 1996, **272**, 1323.
9. J. M. Seminario, C. E. De La Cruz and P. A. Derosa, *J. Am. Chem. Soc.*, 2001, **123**, 5616.
10. D. Bonnell ed., "Scanning Probe Microscopy and Spectroscopy Theory, Techniques, and Applications" 2nd Edition, Wiley-VCH, New York, 2001.
11. a) Vilan, A.; Shanzer, A.; Cahen, D. "Molecular control over Au/GaAs diodes", *Nature* **2000**, *404*, 166-168. b) Ashkenasy, G.; Cahen, D.; Cohen, R.; Shanzer, A.; Vilan, A. "Molecular engineering of semiconductor surfaces and devices", *Accounts Chem. Res.* **2002**, *35*, 121-128. c) Cahen, D.; Kahn, A. "Electron energetics at surfaces and interfaces: Concepts and experiments", *Adv. Mater.* **2003**, *15*, 271-277.

APPENDIX

The following is a procedure written in Igor for calculating steady-state current as a function of voltage with the semi-classical theory. The user is can vary the input parameters R_1 , R_2 , C_1 , C_2 , q_o and temperature. For this procedure to work, the user must first create a wave that contains all voltages of interest. The user must also create 108 other waves with the exact same dimensions as the voltage wave. A final wave containing the input parameters must be created where $c[0] = R_1$, $c[1] = R_2$, $c[2] = C_1$, $c[3] = C_2$, $c[4] = q_o$ and $c[5] = \text{Temperature}$ and $c[6]$ defines an α term for co-tunneling considerations. Comments will appear in bold italic typeface.

```
Function calcDE1on (c, V, n)
    Variable V
    wave c
    Variable n
    Variable d = 1.602e-19
    return ((d/(c[2]+c[3]))*((d/2) + d*n + c[4] + c[3]*V))
end
```

This first function is used to calculate ΔE_1^+ values for n values ranging from -6 to $+6$. The user will need to create 13 waves to contain these values for each value of n used. So for example, a wave called DE1on61 would be filled by inputting the following into the command line:

DE1on61 =: calcDE1on(coef, Voltage, -6)

Where coef is the name of the wave containing the input parameters and Voltage is the name of the wave containing the voltage values. In this way the other 12 waves can be filled with ΔE_1^+ for the corresponding n value.

```
Function calcDE1off (c, V, n)
    Variable V
    wave c
    Variable n
    Variable d = 1.602e-19
    return ((d/(c[2]+c[3]))*((d/2) - d*n - c[4] - c[3]*V))
end
```

```
Function calcDE2on (c, V, n)
    Variable V
    wave c
    Variable n
    Variable d = 1.602e-19
    return ((d/(c[2]+c[3]))*((d/2) + d*n + c[4] - c[2]*V))
```

```

end

Function calcDE2off (c, V, n)
    Variable V
    wave c
    Variable n
    Variable d = 1.602e-19
    return ((d/(c[2]+c[3]))*((d/2) - d*n - c[4] + c[2]*V))
end

```

These three functions are used in the exact same manner as the first in order to calculate ΔE_1^- , ΔE_2^+ and ΔE_2^- . The user has now filled 47 of the 108 waves previously mentioned.

```

Function calcrate1 (c, E1)
    Variable E1
    wave c
    Variable d = 1.602e-19
    Variable kT = ((1.38e-23) * (c[5]))
    Variable Temp = (1 - exp(E1/kT))
    Variable resistance = (d^2)*(c[0])
    Variable rate = (1/resistance)*((-E1)/Temp)
    If (rate <= 0)
        return 0
    else
        return rate
    endif
end

```

This function is used to calculate the Γ_1^+ and Γ_1^- . The user must first have the waves for ΔE_1^+ , ΔE_1^- , ΔE_2^+ and ΔE_2^- filled in. Then the following will be entered in the command line to fill a wave containing Γ_1^+ at each voltage with an n value of -6:

r1on61 := calcrate1 (coef, DE1on61)

The waves containing Γ_1^+ values at each voltage for the other n values, -5 to +6, can be filled by inputting the same command and changing DEon61 to the wave corresponding to the desired n value for the wave being calculated. Γ_1^- can be calculated by using the proper DE1offx wave in the above input line.

```

Function calcrate2 (c, E2)
    Variable E2
    wave c
    Variable d = 1.602e-19
    Variable kT = ((1.38e-23) * (c[5]))

```



```

Variable Temp = (1 - exp(E2/kT))
Variable resistance = ((d^2)*(c[1]))
Variable rate = (1/resistance)*((-E2)/Temp)
If (rate <= 0)
    return 0
else
    return rate
endif
end

```

This function is used in the same way as the previous one to calculate Γ_2^+ and Γ_2^- values. The user has now filled in 47 more of the original 108 waves.

```

Function
calcp51(r1on61,r1off61,r2on61,r2off61,r1on51,r1off51,r2on51,r2off51,r1on41,r1
off41,r2on41,r2off41,r1on31,r1off31,r2on31,r2off31,r1on21,r1off21,r2on21,r2off
21,r1on11,r1off11,r2on11,r2off11,r1on0,r1off0,r2on0,r2off0,r1on1,r1off1,r2on1,r
2off1,r1on12,r1off12,r2on12,r2off12,r1on13,r1off13,r2on13,r2off13,r1on14,r1off
14,r2on14,r2off14,r1on15,r1off15,r2on15,r2off15,r1on16,r1off16,r2on16,r2off16)
    Variable r1on51
    Variable r1off51
    Variable r2on51
    Variable r2off51
    Variable r1on41
    Variable r1off41
    Variable r2on41
    Variable r2off41
    Variable r1on31
    Variable r1off31
    Variable r2on31
    Variable r2off31
    Variable r1on21
    Variable r1off21
    Variable r2on21
    Variable r2off21
    Variable r1on11
    Variable r1off11
    Variable r2on11
    Variable r2off11
    Variable r1on0
    Variable r1off0
    Variable r2on0
    Variable r2off0
    Variable r1on1
    Variable r1off1

```

```

Variable r2on1
Variable r2off1
Variable r1on12
Variable r1off12
Variable r2on12
Variable r2off12
Variable r1on13
Variable r1off13
Variable r2on13
Variable r2off13
Variable r1on14
Variable r1off14
Variable r2on14
Variable r2off14
Variable r1on15
Variable r1off15
Variable r2on15
Variable r2off15
Variable r1on16
Variable r1off16
Variable r2on16
Variable r2off16
Variable r1on61
Variable r1off61
Variable r2on61
Variable r2off61
Variable prob1 = (r1on0 + r2on0)/(r1off1 + r2off1)
Variable prob12 = prob1 * (r1on1 + r2on1)/(r1off12 + r2off12)
Variable prob13 = prob12 * (r1on12 + r2on12)/(r1off13 + r2off13)
Variable prob14 = prob13 * (r1on13 + r2on13)/(r1off14 + r2off14)
Variable prob15 = prob14 * (r1on14 + r2on14)/(r1off15 + r2off15)
Variable prob16 = prob15 * (r1on15 + r2on15)/(r1off16 + r2off16)
Variable prob11 = (r1off0 + r2off0)/(r1on11 + r2on11)
Variable prob21 = prob11 * (r1off11 + r2off11)/(r1on21 + r2on21)
Variable prob31 = prob21 * (r1off21 + r2off21)/(r1on31 + r2on31)
Variable prob41 = prob31 * (r1off31 + r2off31)/(r1on41 + r2on41)
Variable prob51 = prob41 * (r1off41 + r2off41)/(r1on51 + r2on51)
Variable prob61 = prob51 * (r1off51 + r2off51)/(r1on61 + r2on61)
return prob51/(1 + prob1 + prob12 + prob13 + prob14 + prob15 + prob16
+ prob11 + prob21 + prob31 + prob41 + prob51 + prob61)
end

```

This function is used to calculate $r(-5)$ at all voltages considered. The parameters for this function are the rates on and off the particle for all values of n being considered, where $r1on61$ corresponds to Γ_1^+ for $n = -6$ and $r2off12$ corresponds to Γ_2^- for $n = 2$. These rate waves must be calculated before the probability waves can be calculated.

The command line input will be similar to those described above with significantly more variables in the parentheses. It is imperative that the order of the parameters declared in the command line input is the same as the parameters listed in the procedure file.

Function

calcp41(r1on61,r1off61,r2on61,r2off61,r1on51,r1off51,r2on51,r2off51,r1on41,r1off41,r2on41,r2off41,r1on31,r1off31,r2on31,r2off31,r1on21,r1off21,r2on21,r2off21,r1on11,r1off11,r2on11,r2off11,r1on0,r1off0,r2on0,r2off0,r1on1,r1off1,r2on1,r2off1,r1on12,r1off12,r2on12,r2off12,r1on13,r1off13,r2on13,r2off13,r1on14,r1off14,r2on14,r2off14,r1on15,r1off15,r2on15,r2off15,r1on16,r1off16,r2on16,r2off16)

Variable r1on51

Variable r1off51

Variable r2on51

Variable r2off51

Variable r1on41

Variable r1off41

Variable r2on41

Variable r2off41

Variable r1on31

Variable r1off31

Variable r2on31

Variable r2off31

Variable r1on21

Variable r1off21

Variable r2on21

Variable r2off21

Variable r1on11

Variable r1off11

Variable r2on11

Variable r2off11

Variable r1on0

Variable r1off0

Variable r2on0

Variable r2off0

Variable r1on1

Variable r1off1

Variable r2on1

Variable r2off1

Variable r1on12

Variable r1off12

Variable r2on12

Variable r2off12

Variable r1on13

Variable r1off13

Variable r2on13

```

Variable r2off13
Variable r1on14
Variable r1off14
Variable r2on14
Variable r2off14
Variable r1on15
Variable r1off15
Variable r2on15
Variable r2off15
Variable r1on16
Variable r1off16
Variable r2on16
Variable r2off16
Variable r1on61
Variable r1off61
Variable r2on61
Variable r2off61
Variable prob1 = (r1on0 + r2on0)/(r1off1 + r2off1)
Variable prob12 = prob1 * (r1on1 + r2on1)/(r1off12 + r2off12)
Variable prob13 = prob12 * (r1on12 + r2on12)/(r1off13 + r2off13)
Variable prob14 = prob13 * (r1on13 + r2on13)/(r1off14 + r2off13)
Variable prob15 = prob14 * (r1on14 + r2on14)/(r1off15 + r2off15)
Variable prob16 = prob15 * (r1on15 + r2on15)/(r1off16 + r2off16)
Variable prob11 = (r1off0 + r2off0)/(r1on11 + r2on11)
Variable prob21 = prob11 * (r1off11 + r2off11)/(r1on21 + r2on21)
Variable prob31 = prob21 * (r1off21 + r2off21)/(r1on31 + r2on31)
Variable prob41 = prob31 * (r1off31 + r2off31)/(r1on41 + r2on41)
Variable prob51 = prob41 * (r1off41 + r2off41)/(r1on51 + r2on51)
Variable prob61 = prob51 * (r1off51 + r2off51)/(r1on61 + r2on61)
return prob41/(1 + prob1 + prob12 + prob13 + prob14 + prob15 + prob16
+ prob11 + prob21 + prob31 + prob41 + prob51 + prob61)
end

```

Function

```

calcp31(r1on61,r1off61,r2on61,r2off61,r1on51,r1off51,r2on51,r2off51,r1on41,r1
off41,r2on41,r2off41,r1on31,r1off31,r2on31,r2off31,r1on21,r1off21,r2on21,r2off
21,r1on11,r1off11,r2on11,r2off11,r1on0,r1off0,r2on0,r2off0,r1on1,r1off1,r2on1,r
2off1,r1on12,r1off12,r2on12,r2off12,r1on13,r1off13,r2on13,r2off13,r1on14,r1off
14,r2on14,r2off14,r1on15,r1off15,r2on15,r2off15,r1on16,r1off16,r2on16,r2off16)
Variable r1on51
Variable r1off51
Variable r2on51
Variable r2off51
Variable r1on41
Variable r1off41
Variable r2on41

```

Variable r2off41
 Variable r1on31
 Variable r1off31
 Variable r2on31
 Variable r2off31
 Variable r1on21
 Variable r1off21
 Variable r2on21
 Variable r2off21
 Variable r1on11
 Variable r1off11
 Variable r2on11
 Variable r2off11
 Variable r1on0
 Variable r1off0
 Variable r2on0
 Variable r2off0
 Variable r1on1
 Variable r1off1
 Variable r2on1
 Variable r2off1
 Variable r1on12
 Variable r1off12
 Variable r2on12
 Variable r2off12
 Variable r1on13
 Variable r1off13
 Variable r2on13
 Variable r2off13
 Variable r1on14
 Variable r1off14
 Variable r2on14
 Variable r2off14
 Variable r1on15
 Variable r1off15
 Variable r2on15
 Variable r2off15
 Variable r1on16
 Variable r1off16
 Variable r2on16
 Variable r2off16
 Variable r1on61
 Variable r1off61
 Variable r2on61
 Variable r2off61
 Variable prob1 = (r1on0 + r2on0)/(r1off1 + r2off1)

```

Variable prob12 = prob1 * (r1on1 + r2on1)/(r1off12 + r2off12)
Variable prob13 = prob12 * (r1on12 + r2on12)/(r1off13 + r2off13)
Variable prob14 = prob13 * (r1on13 + r2on13)/(r1off14 + r2off13)
Variable prob15 = prob14 * (r1on14 + r2on14)/(r1off15 + r2off15)
Variable prob16 = prob15 * (r1on15 + r2on15)/(r1off16 + r2off16)
Variable prob11 = (r1off0 + r2off0)/(r1on11 + r2on11)
Variable prob21 = prob11 * (r1off11 + r2off11)/(r1on21 + r2on21)
Variable prob31 = prob21 * (r1off21 + r2off21)/(r1on31 + r2on31)
Variable prob41 = prob31 * (r1off31 + r2off31)/(r1on41 + r2on41)
Variable prob51 = prob41 * (r1off41 + r2off41)/(r1on51 + r2on51)
Variable prob61 = prob51 * (r1off51 + r2off51)/(r1on61 + r2on61)
return prob31/(1 + prob1 + prob12 + prob13 + prob14 + prob15 + prob16
+ prob11 + prob21 + prob31 + prob41 + prob51 + prob61)
end

```

Function

```

calcp21(r1on61,r1off61,r2on61,r2off61,r1on51,r1off51,r2on51,r2off51,r1on41,r1
off41,r2on41,r2off41,r1on31,r1off31,r2on31,r2off31,r1on21,r1off21,r2on21,r2off
21,r1on11,r1off11,r2on11,r2off11,r1on0,r1off0,r2on0,r2off0,r1on1,r1off1,r2on1,r
2off1,r1on12,r1off12,r2on12,r2off12,r1on13,r1off13,r2on13,r2off13,r1on14,r1off
14,r2on14,r2off14,r1on15,r1off15,r2on15,r2off15,r1on16,r1off16,r2on16,r2off16)

```

```

Variable r1on51
Variable r1off51
Variable r2on51
Variable r2off51
Variable r1on41
Variable r1off41
Variable r2on41
Variable r2off41
Variable r1on31
Variable r1off31
Variable r2on31
Variable r2off31
Variable r1on21
Variable r1off21
Variable r2on21
Variable r2off21
Variable r1on11
Variable r1off11
Variable r2on11
Variable r2off11
Variable r1on0
Variable r1off0
Variable r2on0
Variable r2off0
Variable r1on1

```

```

Variable r1off1
Variable r2on1
Variable r2off1
Variable r1on12
Variable r1off12
Variable r2on12
Variable r2off12
Variable r1on13
Variable r1off13
Variable r2on13
Variable r2off13
Variable r1on14
Variable r1off14
Variable r2on14
Variable r2off14
Variable r1on15
Variable r1off15
Variable r2on15
Variable r2off15
Variable r1on16
Variable r1off16
Variable r2on16
Variable r2off16
Variable r1on61
Variable r1off61
Variable r2on61
Variable r2off61
Variable prob1 = (r1on0 + r2on0)/(r1off1 + r2off1)
Variable prob12 = prob1 * (r1on1 + r2on1)/(r1off12 + r2off12)
Variable prob13 = prob12 * (r1on12 + r2on12)/(r1off13 + r2off13)
Variable prob14 = prob13 * (r1on13 + r2on13)/(r1off14 + r2off14)
Variable prob15 = prob14 * (r1on14 + r2on14)/(r1off15 + r2off15)
Variable prob16 = prob15 * (r1on15 + r2on15)/(r1off16 + r2off16)
Variable prob11 = (r1off0 + r2off0)/(r1on11 + r2on11)
Variable prob21 = prob11 * (r1off11 + r2off11)/(r1on21 + r2on21)
Variable prob31 = prob21 * (r1off21 + r2off21)/(r1on31 + r2on31)
Variable prob41 = prob31 * (r1off31 + r2off31)/(r1on41 + r2on41)
Variable prob51 = prob41 * (r1off41 + r2off41)/(r1on51 + r2on51)
Variable prob61 = prob51 * (r1off51 + r2off51)/(r1on61 + r2on61)
return prob21/(1 + prob1 + prob12 + prob13 + prob14 + prob15 + prob16
+ prob11 + prob21 + prob31 + prob41 + prob51 + prob61)
end

```

Function

```

calcp11(r1on61,r1off61,r2on61,r2off61,r1on51,r1off51,r2on51,r2off51,r1on41,r1
off41,r2on41,r2off41,r1on31,r1off31,r2on31,r2off31,r1on21,r1off21,r2on21,r2off

```

21,r1on11,r1off11,r2on11,r2off11,r1on0,r1off0,r2on0,r2off0,r1on1,r1off1,r2on1,r2off1,r1on12,r1off12,r2on12,r2off12,r1on13,r1off13,r2on13,r2off13,r1on14,r1off14,r2on14,r2off14,r1on15,r1off15,r2on15,r2off15,r1on16,r1off16,r2on16,r2off16)

Variable r1on51

Variable r1off51

Variable r2on51

Variable r2off51

Variable r1on41

Variable r1off41

Variable r2on41

Variable r2off41

Variable r1on31

Variable r1off31

Variable r2on31

Variable r2off31

Variable r1on21

Variable r1off21

Variable r2on21

Variable r2off21

Variable r1on11

Variable r1off11

Variable r2on11

Variable r2off11

Variable r1on0

Variable r1off0

Variable r2on0

Variable r2off0

Variable r1on1

Variable r1off1

Variable r2on1

Variable r2off1

Variable r1on12

Variable r1off12

Variable r2on12

Variable r2off12

Variable r1on13

Variable r1off13

Variable r2on13

Variable r2off13

Variable r1on14

Variable r1off14

Variable r2on14

Variable r2off14

Variable r1on15

Variable r1off15

Variable r2on15


```

Variable r2off15
Variable r1on16
Variable r1off16
Variable r2on16
Variable r2off16
Variable r1on61
Variable r1off61
Variable r2on61
Variable r2off61
Variable prob1 = (r1on0 + r2on0)/(r1off1 + r2off1)
Variable prob12 = prob1 * (r1on1 + r2on1)/(r1off12 + r2off12)
Variable prob13 = prob12 * (r1on12 + r2on12)/(r1off13 + r2off13)
Variable prob14 = prob13 * (r1on13 + r2on13)/(r1off14 + r2off13)
Variable prob15 = prob14 * (r1on14 + r2on14)/(r1off15 + r2off15)
Variable prob16 = prob15 * (r1on15 + r2on15)/(r1off16 + r2off16)
Variable prob11 = (r1off0 + r2off0)/(r1on11 + r2on11)
Variable prob21 = prob11 * (r1off11 + r2off11)/(r1on21 + r2on21)
Variable prob31 = prob21 * (r1off21 + r2off21)/(r1on31 + r2on31)
Variable prob41 = prob31 * (r1off31 + r2off31)/(r1on41 + r2on41)
Variable prob51 = prob41 * (r1off41 + r2off41)/(r1on51 + r2on51)
Variable prob61 = prob51 * (r1off51 + r2off51)/(r1on61 + r2on61)
return prob11/(1 + prob1 + prob12 + prob13 + prob14 + prob15 + prob16
+ prob11 + prob21 + prob31 + prob41 + prob51 + prob61)
end

```

Function

```

calcp0(r1on61,r1off61,r2on61,r2off61,r1on51,r1off51,r2on51,r2off51,r1on41,r1o
ff41,r2on41,r2off41,r1on31,r1off31,r2on31,r2off31,r1on21,r1off21,r2on21,r2off2
1,r1on11,r1off11,r2on11,r2off11,r1on0,r1off0,r2on0,r2off0,r1on1,r1off1,r2on1,r2
off1,r1on12,r1off12,r2on12,r2off12,r1on13,r1off13,r2on13,r2off13,r1on14,r1off1
4,r2on14,r2off14,r1on15,r1off15,r2on15,r2off15,r1on16,r1off16,r2on16,r2off16)
Variable r1on51
Variable r1off51
Variable r2on51
Variable r2off51
Variable r1on41
Variable r1off41
Variable r2on41
Variable r2off41
Variable r1on31
Variable r1off31
Variable r2on31
Variable r2off31
Variable r1on21
Variable r1off21
Variable r2on21

```

Variable r2off21
 Variable r1on11
 Variable r1off11
 Variable r2on11
 Variable r2off11
 Variable r1on0
 Variable r1off0
 Variable r2on0
 Variable r2off0
 Variable r1on1
 Variable r1off1
 Variable r2on1
 Variable r2off1
 Variable r1on12
 Variable r1off12
 Variable r2on12
 Variable r2off12
 Variable r1on13
 Variable r1off13
 Variable r2on13
 Variable r2off13
 Variable r1on14
 Variable r1off14
 Variable r2on14
 Variable r2off14
 Variable r1on15
 Variable r1off15
 Variable r2on15
 Variable r2off15
 Variable r1on16
 Variable r1off16
 Variable r2on16
 Variable r2off16
 Variable r1on61
 Variable r1off61
 Variable r2on61
 Variable r2off61
 Variable prob1 = (r1on0 + r2on0)/(r1off1 + r2off1)
 Variable prob12 = prob1 * (r1on1 + r2on1)/(r1off12 + r2off12)
 Variable prob13 = prob12 * (r1on12 + r2on12)/(r1off13 + r2off13)
 Variable prob14 = prob13 * (r1on13 + r2on13)/(r1off14 + r2off13)
 Variable prob15 = prob14 * (r1on14 + r2on14)/(r1off15 + r2off15)
 Variable prob16 = prob15 * (r1on15 + r2on15)/(r1off16 + r2off16)
 Variable prob11 = (r1off0 + r2off0)/(r1on11 + r2on11)
 Variable prob21 = prob11 * (r1off11 + r2off11)/(r1on21 + r2on21)
 Variable prob31 = prob21 * (r1off21 + r2off21)/(r1on31 + r2on31)

```

Variable prob41 = prob31 * (r1off31 + r2off31)/(r1on41 + r2on41)
Variable prob51 = prob41 * (r1off41 + r2off41)/(r1on51 + r2on51)
Variable prob61 = prob51 * (r1off51 + r2off51)/(r1on61 + r2on61)
return 1/(1 + prob1 + prob12 + prob13 + prob14 + prob15 + prob16 +
prob11 + prob21 + prob31 + prob41 + prob51 + prob61)
end

```

Function

```

calcp1(r1on61,r1off61,r2on61,r2off61,r1on51,r1off51,r2on51,r2off51,r1on41,r1o
ff41,r2on41,r2off41,r1on31,r1off31,r2on31,r2off31,r1on21,r1off21,r2on21,r2off2
1,r1on11,r1off11,r2on11,r2off11,r1on0,r1off0,r2on0,r2off0,r1on1,r1off1,r2on1,r2
off1,r1on12,r1off12,r2on12,r2off12,r1on13,r1off13,r2on13,r2off13,r1on14,r1off1
4,r2on14,r2off14,r1on15,r1off15,r2on15,r2off15,r1on16,r1off16,r2on16,r2off16)

```

Variable r1on51

Variable r1off51

Variable r2on51

Variable r2off51

Variable r1on41

Variable r1off41

Variable r2on41

Variable r2off41

Variable r1on31

Variable r1off31

Variable r2on31

Variable r2off31

Variable r1on21

Variable r1off21

Variable r2on21

Variable r2off21

Variable r1on11

Variable r1off11

Variable r2on11

Variable r2off11

Variable r1on0

Variable r1off0

Variable r2on0

Variable r2off0

Variable r1on1

Variable r1off1

Variable r2on1

Variable r2off1

Variable r1on12

Variable r1off12

Variable r2on12

Variable r2off12

Variable r1on13

```

Variable r1off13
Variable r2on13
Variable r2off13
Variable r1on14
Variable r1off14
Variable r2on14
Variable r2off14
Variable r1on15
Variable r1off15
Variable r2on15
Variable r2off15
Variable r1on16
Variable r1off16
Variable r2on16
Variable r2off16
Variable r1on61
Variable r1off61
Variable r2on61
Variable r2off61
Variable prob1 = (r1on0 + r2on0)/(r1off1 + r2off1)
Variable prob12 = prob1 * (r1on1 + r2on1)/(r1off12 + r2off12)
Variable prob13 = prob12 * (r1on12 + r2on12)/(r1off13 + r2off13)
Variable prob14 = prob13 * (r1on13 + r2on13)/(r1off14 + r2off13)
Variable prob15 = prob14 * (r1on14 + r2on14)/(r1off15 + r2off15)
Variable prob16 = prob15 * (r1on15 + r2on15)/(r1off16 + r2off16)
Variable prob11 = (r1off0 + r2off0)/(r1on11 + r2on11)
Variable prob21 = prob11 * (r1off11 + r2off11)/(r1on21 + r2on21)
Variable prob31 = prob21 * (r1off21 + r2off21)/(r1on31 + r2on31)
Variable prob41 = prob31 * (r1off31 + r2off31)/(r1on41 + r2on41)
Variable prob51 = prob41 * (r1off41 + r2off41)/(r1on51 + r2on51)
Variable prob61 = prob51 * (r1off51 + r2off51)/(r1on61 + r2on61)
return prob1/(1 + prob1 + prob12 + prob13 + prob14 + prob15 + prob16 +
prob11 + prob21 + prob31 + prob41 + prob51 + prob61)
end

```

Function

```

calep12(r1on61,r1off61,r2on61,r2off61,r1on51,r1off51,r2on51,r2off51,r1on41,r1
off41,r2on41,r2off41,r1on31,r1off31,r2on31,r2off31,r1on21,r1off21,r2on21,r2off
21,r1on11,r1off11,r2on11,r2off11,r1on0,r1off0,r2on0,r2off0,r1on1,r1off1,r2on1,r
2off1,r1on12,r1off12,r2on12,r2off12,r1on13,r1off13,r2on13,r2off13,r1on14,r1off
14,r2on14,r2off14,r1on15,r1off15,r2on15,r2off15,r1on16,r1off16,r2on16,r2off16)
Variable r1on51
Variable r1off51
Variable r2on51
Variable r2off51
Variable r1on41

```

Variable r1off41
Variable r2on41
Variable r2off41
Variable r1on31
Variable r1off31
Variable r2on31
Variable r2off31
Variable r1on21
Variable r1off21
Variable r2on21
Variable r2off21
Variable r1on11
Variable r1off11
Variable r2on11
Variable r2off11
Variable r1on0
Variable r1off0
Variable r2on0
Variable r2off0
Variable r1on1
Variable r1off1
Variable r2on1
Variable r2off1
Variable r1on12
Variable r1off12
Variable r2on12
Variable r2off12
Variable r1on13
Variable r1off13
Variable r2on13
Variable r2off13
Variable r1on14
Variable r1off14
Variable r2on14
Variable r2off14
Variable r1on15
Variable r1off15
Variable r2on15
Variable r2off15
Variable r1on16
Variable r1off16
Variable r2on16
Variable r2off16
Variable r1on61
Variable r1off61
Variable r2on61

```

Variable r2off61
Variable prob1 = (r1on0 + r2on0)/(r1off1 + r2off1)
Variable prob12 = prob1 * (r1on1 + r2on1)/(r1off12 + r2off12)
Variable prob13 = prob12 * (r1on12 + r2on12)/(r1off13 + r2off13)
Variable prob14 = prob13 * (r1on13 + r2on13)/(r1off14 + r2off14)
Variable prob15 = prob14 * (r1on14 + r2on14)/(r1off15 + r2off15)
Variable prob16 = prob15 * (r1on15 + r2on15)/(r1off16 + r2off16)
Variable prob11 = (r1off0 + r2off0)/(r1on11 + r2on11)
Variable prob21 = prob11 * (r1off11 + r2off11)/(r1on21 + r2on21)
Variable prob31 = prob21 * (r1off21 + r2off21)/(r1on31 + r2on31)
Variable prob41 = prob31 * (r1off31 + r2off31)/(r1on41 + r2on41)
Variable prob51 = prob41 * (r1off41 + r2off41)/(r1on51 + r2on51)
Variable prob61 = prob51 * (r1off51 + r2off51)/(r1on61 + r2on61)
return prob12/(1 + prob1 + prob12 + prob13 + prob14 + prob15 + prob16
+ prob11 + prob21 + prob31 + prob41 + prob51 + prob61)
end

```

Function

```

calcp13(r1on61,r1off61,r2on61,r2off61,r1on51,r1off51,r2on51,r2off51,r1on41,r1
off41,r2on41,r2off41,r1on31,r1off31,r2on31,r2off31,r1on21,r1off21,r2on21,r2off
21,r1on11,r1off11,r2on11,r2off11,r1on0,r1off0,r2on0,r2off0,r1on1,r1off1,r2on1,r
2off1,r1on12,r1off12,r2on12,r2off12,r1on13,r1off13,r2on13,r2off13,r1on14,r1off
14,r2on14,r2off14,r1on15,r1off15,r2on15,r2off15,r1on16,r1off16,r2on16,r2off16)
Variable r1on51
Variable r1off51
Variable r2on51
Variable r2off51
Variable r1on41
Variable r1off41
Variable r2on41
Variable r2off41
Variable r1on31
Variable r1off31
Variable r2on31
Variable r2off31
Variable r1on21
Variable r1off21
Variable r2on21
Variable r2off21
Variable r1on11
Variable r1off11
Variable r2on11
Variable r2off11
Variable r1on0
Variable r1off0
Variable r2on0

```

```

Variable r2off0
Variable r1on1
Variable r1off1
Variable r2on1
Variable r2off1
Variable r1on12
Variable r1off12
Variable r2on12
Variable r2off12
Variable r1on13
Variable r1off13
Variable r2on13
Variable r2off13
Variable r1on14
Variable r1off14
Variable r2on14
Variable r2off14
Variable r1on15
Variable r1off15
Variable r2on15
Variable r2off15
Variable r1on16
Variable r1off16
Variable r2on16
Variable r2off16
Variable r1on61
Variable r1off61
Variable r2on61
Variable r2off61
Variable prob1 = (r1on0 + r2on0)/(r1off1 + r2off1)
Variable prob12 = prob1 * (r1on1 + r2on1)/(r1off12 + r2off12)
Variable prob13 = prob12 * (r1on12 + r2on12)/(r1off13 + r2off13)
Variable prob14 = prob13 * (r1on13 + r2on13)/(r1off14 + r2off13)
Variable prob15 = prob14 * (r1on14 + r2on14)/(r1off15 + r2off15)
Variable prob16 = prob15 * (r1on15 + r2on15)/(r1off16 + r2off16)
Variable prob11 = (r1off0 + r2off0)/(r1on11 + r2on11)
Variable prob21 = prob11 * (r1off11 + r2off11)/(r1on21 + r2on21)
Variable prob31 = prob21 * (r1off21 + r2off21)/(r1on31 + r2on31)
Variable prob41 = prob31 * (r1off31 + r2off31)/(r1on41 + r2on41)
Variable prob51 = prob41 * (r1off41 + r2off41)/(r1on51 + r2on51)
Variable prob61 = prob51 * (r1off51 + r2off51)/(r1on61 + r2on61)
return prob13/(1 + prob1 + prob12 + prob13 + prob14 + prob15 + prob16
+ prob11 + prob21 + prob31 + prob41 + prob51 + prob61)
end

```

Function

calcp14(r1on61,r1off61,r2on61,r2off61,r1on51,r1off51,r2on51,r2off51,r1on41,r1off41,r2on41,r2off41,r1on31,r1off31,r2on31,r2off31,r1on21,r1off21,r2on21,r2off21,r1on11,r1off11,r2on11,r2off11,r1on0,r1off0,r2on0,r2off0,r1on1,r1off1,r2on1,r2off1,r1on12,r1off12,r2on12,r2off12,r1on13,r1off13,r2on13,r2off13,r1on14,r1off14,r2on14,r2off14,r1on15,r1off15,r2on15,r2off15,r1on16,r1off16,r2on16,r2off16)

Variable r1on51

Variable r1off51

Variable r2on51

Variable r2off51

Variable r1on41

Variable r1off41

Variable r2on41

Variable r2off41

Variable r1on31

Variable r1off31

Variable r2on31

Variable r2off31

Variable r1on21

Variable r1off21

Variable r2on21

Variable r2off21

Variable r1on11

Variable r1off11

Variable r2on11

Variable r2off11

Variable r1on0

Variable r1off0

Variable r2on0

Variable r2off0

Variable r1on1

Variable r1off1

Variable r2on1

Variable r2off1

Variable r1on12

Variable r1off12

Variable r2on12

Variable r2off12

Variable r1on13

Variable r1off13

Variable r2on13

Variable r2off13

Variable r1on14

Variable r1off14

Variable r2on14

Variable r2off14


```

Variable r1on15
Variable r1off15
Variable r2on15
Variable r2off15
Variable r1on16
Variable r1off16
Variable r2on16
Variable r2off16
Variable r1on61
Variable r1off61
Variable r2on61
Variable r2off61
Variable prob1 = (r1on0 + r2on0)/(r1off1 + r2off1)
Variable prob12 = prob1 * (r1on1 + r2on1)/(r1off12 + r2off12)
Variable prob13 = prob12 * (r1on12 + r2on12)/(r1off13 + r2off13)
Variable prob14 = prob13 * (r1on13 + r2on13)/(r1off14 + r2off13)
Variable prob15 = prob14 * (r1on14 + r2on14)/(r1off15 + r2off15)
Variable prob16 = prob15 * (r1on15 + r2on15)/(r1off16 + r2off16)
Variable prob11 = (r1off0 + r2off0)/(r1on11 + r2on11)
Variable prob21 = prob11 * (r1off11 + r2off11)/(r1on21 + r2on21)
Variable prob31 = prob21 * (r1off21 + r2off21)/(r1on31 + r2on31)
Variable prob41 = prob31 * (r1off31 + r2off31)/(r1on41 + r2on41)
Variable prob51 = prob41 * (r1off41 + r2off41)/(r1on51 + r2on51)
Variable prob61 = prob51 * (r1off51 + r2off51)/(r1on61 + r2on61)
return prob14/(1 + prob1 + prob12 + prob13 + prob14 + prob15 + prob16
+ prob11 + prob21 + prob31 + prob41 + prob51 + prob61)
end

```

Function

```

calcp15(r1on61,r1off61,r2on61,r2off61,r1on51,r1off51,r2on51,r2off51,r1on41,r1
off41,r2on41,r2off41,r1on31,r1off31,r2on31,r2off31,r1on21,r1off21,r2on21,r2off
21,r1on11,r1off11,r2on11,r2off11,r1on0,r1off0,r2on0,r2off0,r1on1,r1off1,r2on1,r
2off1,r1on12,r1off12,r2on12,r2off12,r1on13,r1off13,r2on13,r2off13,r1on14,r1off
14,r2on14,r2off14,r1on15,r1off15,r2on15,r2off15,r1on16,r1off16,r2on16,r2off16)
Variable r1on51
Variable r1off51
Variable r2on51
Variable r2off51
Variable r1on41
Variable r1off41
Variable r2on41
Variable r2off41
Variable r1on31
Variable r1off31
Variable r2on31
Variable r2off31

```

Variable r1on21
 Variable r1off21
 Variable r2on21
 Variable r2off21
 Variable r1on11
 Variable r1off11
 Variable r2on11
 Variable r2off11
 Variable r1on0
 Variable r1off0
 Variable r2on0
 Variable r2off0
 Variable r1on1
 Variable r1off1
 Variable r2on1
 Variable r2off1
 Variable r1on12
 Variable r1off12
 Variable r2on12
 Variable r2off12
 Variable r1on13
 Variable r1off13
 Variable r2on13
 Variable r2off13
 Variable r1on14
 Variable r1off14
 Variable r2on14
 Variable r2off14
 Variable r1on15
 Variable r1off15
 Variable r2on15
 Variable r2off15
 Variable r1on16
 Variable r1off16
 Variable r2on16
 Variable r2off16
 Variable r1on61
 Variable r1off61
 Variable r2on61
 Variable r2off61
 Variable prob1 = (r1on0 + r2on0)/(r1off1 + r2off1)
 Variable prob12 = prob1 * (r1on1 + r2on1)/(r1off12 + r2off12)
 Variable prob13 = prob12 * (r1on12 + r2on12)/(r1off13 + r2off13)
 Variable prob14 = prob13 * (r1on13 + r2on13)/(r1off14 + r2off14)
 Variable prob15 = prob14 * (r1on14 + r2on14)/(r1off15 + r2off15)
 Variable prob16 = prob15 * (r1on15 + r2on15)/(r1off16 + r2off16)

```

Variable prob11 = (r1off0 + r2off0)/(r1on11 + r2on11)
Variable prob21 = prob11 * (r1off11 + r2off11)/(r1on21 + r2on21)
Variable prob31 = prob21 * (r1off21 + r2off21)/(r1on31 + r2on31)
Variable prob41 = prob31 * (r1off31 + r2off31)/(r1on41 + r2on41)
Variable prob51 = prob41 * (r1off41 + r2off41)/(r1on51 + r2on51)
Variable prob61 = prob51 * (r1off51 + r2off51)/(r1on61 + r2on61)
return prob15/(1 + prob1 + prob12 + prob13 + prob14 + prob15 + prob16
+ prob11 + prob21 + prob31 + prob41 + prob51 + prob61)
end

```

Function

```

calcp16(r1on61,r1off61,r2on61,r2off61,r1on51,r1off51,r2on51,r2off51,r1on41,r1
off41,r2on41,r2off41,r1on31,r1off31,r2on31,r2off31,r1on21,r1off21,r2on21,r2off
21,r1on11,r1off11,r2on11,r2off11,r1on0,r1off0,r2on0,r2off0,r1on1,r1off1,r2on1,r
2off1,r1on12,r1off12,r2on12,r2off12,r1on13,r1off13,r2on13,r2off13,r1on14,r1off
14,r2on14,r2off14,r1on15,r1off15,r2on15,r2off15,r1on16,r1off16,r2on16,r2off16)
Variable r1on51
Variable r1off51
Variable r2on51
Variable r2off51
Variable r1on41
Variable r1off41
Variable r2on41
Variable r2off41
Variable r1on31
Variable r1off31
Variable r2on31
Variable r2off31
Variable r1on21
Variable r1off21
Variable r2on21
Variable r2off21
Variable r1on11
Variable r1off11
Variable r2on11
Variable r2off11
Variable r1on0
Variable r1off0
Variable r2on0
Variable r2off0
Variable r1on1
Variable r1off1
Variable r2on1
Variable r2off1
Variable r1on12
Variable r1off12

```

```

Variable r2on12
Variable r2off12
Variable r1on13
Variable r1off13
Variable r2on13
Variable r2off13
Variable r1on14
Variable r1off14
Variable r2on14
Variable r2off14
Variable r1on15
Variable r1off15
Variable r2on15
Variable r2off15
Variable r1on16
Variable r1off16
Variable r2on16
Variable r2off16
Variable r1on61
Variable r1off61
Variable r2on61
Variable r2off61
Variable prob1 = (r1on0 + r2on0)/(r1off1 + r2off1)
Variable prob12 = prob1 * (r1on1 + r2on1)/(r1off12 + r2off12)
Variable prob13 = prob12 * (r1on12 + r2on12)/(r1off13 + r2off13)
Variable prob14 = prob13 * (r1on13 + r2on13)/(r1off14 + r2off13)
Variable prob15 = prob14 * (r1on14 + r2on14)/(r1off15 + r2off15)
Variable prob16 = prob15 * (r1on15 + r2on15)/(r1off16 + r2off16)
Variable prob11 = (r1off0 + r2off0)/(r1on11 + r2on11)
Variable prob21 = prob11 * (r1off11 + r2off11)/(r1on21 + r2on21)
Variable prob31 = prob21 * (r1off21 + r2off21)/(r1on31 + r2on31)
Variable prob41 = prob31 * (r1off31 + r2off31)/(r1on41 + r2on41)
Variable prob51 = prob41 * (r1off41 + r2off41)/(r1on51 + r2on51)
Variable prob61 = prob51 * (r1off51 + r2off51)/(r1on61 + r2on61)
return prob16/(1 + prob1 + prob12 + prob13 + prob14 + prob15 + prob16
+ prob11 + prob21 + prob31 + prob41 + prob51 + prob61)
end

```

Function

```

calcp61(r1on61,r1off61,r2on61,r2off61,r1on51,r1off51,r2on51,r2off51,r1on41,r1
off41,r2on41,r2off41,r1on31,r1off31,r2on31,r2off31,r1on21,r1off21,r2on21,r2off
21,r1on11,r1off11,r2on11,r2off11,r1on0,r1off0,r2on0,r2off0,r1on1,r1off1,r2on1,r
2off1,r1on12,r1off12,r2on12,r2off12,r1on13,r1off13,r2on13,r2off13,r1on14,r1off
14,r2on14,r2off14,r1on15,r1off15,r2on15,r2off15,r1on16,r1off16,r2on16,r2off16)
Variable r1on51
Variable r1off51

```

Variable r2on51
Variable r2off51
Variable r1on41
Variable r1off41
Variable r2on41
Variable r2off41
Variable r1on31
Variable r1off31
Variable r2on31
Variable r2off31
Variable r1on21
Variable r1off21
Variable r2on21
Variable r2off21
Variable r1on11
Variable r1off11
Variable r2on11
Variable r2off11
Variable r1on0
Variable r1off0
Variable r2on0
Variable r2off0
Variable r1on1
Variable r1off1
Variable r2on1
Variable r2off1
Variable r1on12
Variable r1off12
Variable r2on12
Variable r2off12
Variable r1on13
Variable r1off13
Variable r2on13
Variable r2off13
Variable r1on14
Variable r1off14
Variable r2on14
Variable r2off14
Variable r1on15
Variable r1off15
Variable r2on15
Variable r2off15
Variable r1on16
Variable r1off16
Variable r2on16
Variable r2off16

```

Variable r1on61
Variable r1off61
Variable r2on61
Variable r2off61
Variable prob1 = (r1on0 + r2on0)/(r1off1 + r2off1)
Variable prob12 = prob1 * (r1on1 + r2on1)/(r1off12 + r2off12)
Variable prob13 = prob12 * (r1on12 + r2on12)/(r1off13 + r2off13)
Variable prob14 = prob13 * (r1on13 + r2on13)/(r1off14 + r2off13)
Variable prob15 = prob14 * (r1on14 + r2on14)/(r1off15 + r2off15)
Variable prob16 = prob15 * (r1on15 + r2on15)/(r1off16 + r2off16)
Variable prob11 = (r1off0 + r2off0)/(r1on11 + r2on11)
Variable prob21 = prob11 * (r1off11 + r2off11)/(r1on21 + r2on21)
Variable prob31 = prob21 * (r1off21 + r2off21)/(r1on31 + r2on31)
Variable prob41 = prob31 * (r1off31 + r2off31)/(r1on41 + r2on41)
Variable prob51 = prob41 * (r1off41 + r2off41)/(r1on51 + r2on51)
Variable prob61 = prob51 * (r1off51 + r2off51)/(r1on61 + r2on61)
return prob61/(1 + prob1 + prob12 + prob13 + prob14 + prob15 + prob16
+ prob11 + prob21 + prob31 + prob41 + prob51 + prob61)
end

```

These functions are used in a similar way to calculate $r(-6)$ through $r(+6)$ at all voltage values considered. The user has now defined 107 of the 108 waves described earlier.

```

Function calccurrent
(c,V,prob61,prob51,prob41,prob31,prob21,prob11,prob0,prob1,prob12,prob13,pr
ob14,prob15,prob16,r2on61,r2off61,r2on51,r2off51,r2on41,r2off41,r2on31,r2off3
1,r2on21,r2off21,r2on11,r2off11,r2on0,r2off0,r2on1,r2off1,r2on12,r2off12,r2on1
3,r2off13,r2on14,r2off14,r2on15,r2off15,r2on16,r2off16)
wave c
Variable V
Variable prob61
Variable prob51
Variable prob41
Variable prob31
Variable prob21
Variable prob11
Variable prob0
Variable prob1
Variable prob12
Variable prob13
Variable prob14
Variable prob15
Variable prob16
Variable r2on61
Variable r2off61
Variable r2on51

```

```

Variable r2off51
Variable r2on41
Variable r2off41
Variable r2on31
Variable r2off31
Variable r2on21
Variable r2off21
Variable r2on11
Variable r2off11
Variable r2on0
Variable r2off0
Variable r2on1
Variable r2off1
Variable r2on12
Variable r2off12
Variable r2on13
Variable r2off13
Variable r2on14
Variable r2off14
Variable r2on15
Variable r2off15
Variable r2on16
Variable r2off16
Variable d = 1.602e-19
If (V>=0)
    return ((prob61*(r2off61-r2on61))+(prob51 *(r2off51 -
r2on51))+(prob41*(r2off41-r2on41))+(prob31*(r2off31 -
r2on31))+(prob21*(r2off21-r2on21))+(prob11*(r2off11-
r2on11))+(prob0*(r2off0-r2on0))+(prob1*(r2off1-r2on1))+(prob12*(r2off12-
r2on12))+(prob13*(r2off13-r2on13))+(prob14*(r2off14-
r2on14))+(prob15*(r2off15-r2on15))+(prob16*(r2off16-r2on16))) * -d + c[6]*V^2
else
    return ((prob61*(r2off61-r2on61))+(prob51 *(r2off51 -
r2on51))+(prob41*(r2off41-r2on41))+(prob31*(r2off31 -
r2on31))+(prob21*(r2off21-r2on21))+(prob11*(r2off11-
r2on11))+(prob0*(r2off0-r2on0))+(prob1*(r2off1-r2on1))+(prob12*(r2off12-
r2on12))+(prob13*(r2off13-r2on13))+(prob14*(r2off14-
r2on14))+(prob15*(r2off15-r2on15))+(prob16*(r2off16-r2on16))) * -d - c[6]*V^2
endif
end

```

Finally, this function is used to calculate the steady-state current at each voltage considered. This function currently contains a simple exponential function added to the semi-classical equation for calculating current. This can be used to account for co-tunneling events. If the user does not want to consider this co-tunneling, c[6] can be

set equal to zero. Again, it is imperative that the parameters in the command line input correspond to the order of the parameters listed in the procedure file.

Once this wave is defined (the 108th wave calculated by the user) a graph can be created with the Voltage wave as the x-axis and the calculated current wave as the y-axis. Leaving this graph and a table containing the “coef” wave open, the user can watch the shape of the current vs. voltage curve change in real-time as the input parameters are varied. By creating a wave that contains experimental data (where the current was sampled at the same voltages used in the Voltage wave) and plotting it in the same window, the user can adjust the input parameters until a good fit between the two curves is reached.